UNIVERSITY OF OKLAHOMA

GRADUATE COLLEGE

CFD ANALYSIS OF POWER-LAW FLUID IN A PARTIALLY BLOCKED ECCENTRIC ANNULUS UNDER TURBULENT FLOW CONDITIONS

A THESIS

SUBMITTED TO THE GRADUATE FACULTY

in partial fulfillment of the requirements for the

Degree of

MASTER OF SCIENCE

By

RAVI ANANDALAL SINGH

Norman, Oklahoma

2019

CFD ANALYSIS OF POWER-LAW FLUID IN A PARTIALLY BLOCKED ECCENTIRC ANNULUS UNDER TURBULENT FLOW CONDITIONS

A THESIS APPROVED FOR THE

MEWBOURNE SCHOOL OF PETROLEUM AND GEOLOGICAL ENGINEERING

BY THE COMMITTEE CONSISTING OF

Ramadan Ahmed, Ph.D.
Chair

Prakash Vedula, Ph.D.

Hamidreza Karami, Ph.D.

ABSTRACT

An increase in hydrocarbon production by the application of several laterals from a single vertical wellbore is now a widespread practice. Horizontal and inclined wells are drilled at record lengths, which once seemed impossible for both onshore and offshore locations. However, well inclination causes eccentric geometry in the wellbore. The eccentric annulus results in a velocity distribution with stagnant zones that make hole cleaning inefficient which leads to the formation of stationary cutting beds and partial blockage of the annulus. These undesired bed development restrict the fluid motion by providing hydraulic resistance and thereby affecting the bottom hole pressure, which in turn influences the efficiency of the drilling operation and increases the non-productive time.

This research focuses on analyzing the fluid motion in a partially blocked eccentric wellbore using the Computational Fluid Mechanics (CFD) approach. A commercial software ANSYS Fluent is used to perform the CFD analysis. The study is conducted considering the flow of power-law fluid in eccentric annulus under turbulent flow conditions. Different flow geometries are created by varying the blockage height and diameter ratio. The pipe is considered highly eccentric (90%) for all cases. The fluid properties are varied by altering the consistency index and the fluid behavior index and analyzing their impact on the velocity profile, pressure loss, wall and bed shear stresses.

Observations are made with respect to pressure loss and shear stress. The annular pressure loss increases with cutting bed height at a given flow rate. Furthermore, at a constant flow rate, the higher the shear-thinning property of the fluid, the lower is the effect of cutting height on the annular pressure loss.

CFD simulation results are evaluated by comparing with available experimental measurements and the predictions of existing models. The pressure losses predicted using CFD are predominantly in agreement with experimental measurements. After verification and validation, CFD simulation results are utilized to develop an approximate correlation for dimensionless bed shear stress. The developed correlation exhibits a discrepancy of about ±10% against simulation results. The correlation helps optimize hole cleaning and wellbore hydraulics.

ACKNOWLEDGEMENTS

I would like to express the deepest appreciation to my committee chair, Dr. Ramadan Ahmed, for placing faith in me and selecting me as his graduate student. This thesis would not be a reality without his kind support, patience and I express a deep sense of thanks and gratitude to my mentor for his advice and assistance in the preparation of this thesis.

The author would also like to thank the advisory committee members Dr. Prakash Vedul and Dr. Hamidreza Karami, for their suggestions and advice. Also, the assistance provided by the College of Engineering for the computing software and the vital laboratory space in Rawl Engineering Practice Facility Room 220 and Carson Engineering Center Room 205 and 206 is acknowledged. Finally, I would also like to thank the Mewbourne School of Petroleum and Geological Engineering for supporting me during this investigation.

This acknowledgment would not be complete without thanking my family members Anandalal Singh and Manju Singh, who have supported me throughout my MS endeavor financially, emotionally and morally.

Table of Contents

List of Figures

Figure No. Page No.

List of Tables

Table No. Page No.

Chapter 1

Introduction

1.1 Overview

During the drilling operation, fluid from the surface flows through the drill pipe and returns back to the surface through the annular wellbore. As the fluid flows in this annulus, frictional resistant develops, leading to pressure loss. This frictional pressure loss is a critical parameter in the optimization of the drilling process. In this study, a 3-D hydrodynamic model is utilized incorporating the blockage issues experienced in the eccentric wellbore. Similar annular flows are experienced in numerous industries and can form the solution basis for industrial applications such as heat exchangers, steam generators, phase separators, inclined and horizontal wellbores, and oil risers.

In order to maximize the efficiency of a drilling process, the drilled cuttings need to be transported out of the hole quickly. At the same time, the bottom hole pressure needs to be maintained below the fracture pressure. Also, while performing a drilling operation, the bottom hole pressure needs to be kept slightly above the pore pressure. These pressure maintenance requirements make hole cleaning very challenging. Failure in ensuring a good hole cleaning condition can result in major drilling issues like a stuck pipe, fluid loss and lost circulation, or formation damage. Therefore, a wellbore hydraulic study is crucial in developing accurate hydraulic models that are required to predict annular pressure loss and subsequently bottom hole pressure to optimize hole cleaning.

Flows in eccentric annuli are found to be affected by variations including annular geometry (eccentricity, diameter ratio, and bed height), fluid circulation velocity. In addition to these variables, fluid properties such as viscosity, consistency index also affect the wellbore flow dynamics. Numerous studies (Hanks, 1979; Filip and David, 2003; Bicalho et al., 2016a; Founargiotakis et al., 2008, Ahmed et al., 2006, Ahmed and Miska 2009, Rojas et al., 2017) have been performed in the past to better understand fluid flow in wellbores and help by contributing their findings for an effective hole cleaning solution.

In the past, a number of studies (Hanks, 1979; Filip and David, 2003; Bicalho et al., 2016b; Founargiotakis et al., 2008) focused on concentric annular flows. However, with the advancement of horizontal and inclined well drilling, flow in eccentric annuli has attracted great interest. In horizontal and inclined wells, gravity causes the inner pipe to lay down on the low-side of the annulus, forming an eccentric geometry. For the schematic of an eccentric annulus presented in Figure 1.1, the following relation expresses eccentricity in dimensionless form.

$$e = \frac{d}{R_0 - R_i} \tag{1.1}$$

where,

e = Eccentricity

d = Distance of between the centers of inner and outer cylinders

R_0 = Radius of the outer cylinder

R_i = Radius of the inner cylinder

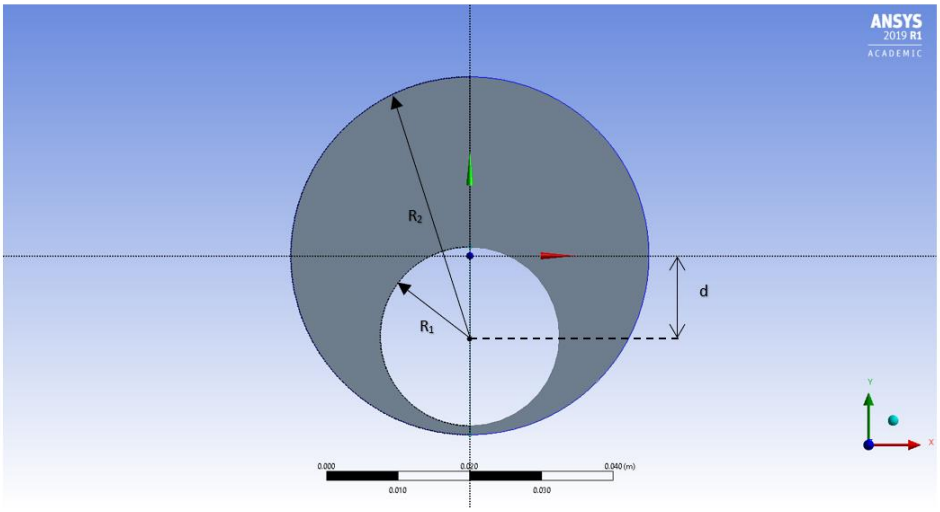

Figure 1.1. Eccentric annular geometry

1.2 Problem Description

One of the primary functions of a drilling fluid is to transport the solid cutting generated at the bottom of the wellbore to the surface. Failure in cuttings transport can cause bit damage, thereby reducing the efficiency of a drilling process. Besides this, ineffective hole cleaning can have many consequences. It can lead to the formation of cuttings beds in the wellbore causing a number of drilling problems such as stuck pipe, lost circulation, wellbore steering problems, an increase in drag and torque resulting in a significant increase in non-productive time. In order to minimize the adverse effects of bed formation and annular blockage, variables such as fluid velocity and rheology need to be controlled to achieve efficient wellbore cleanup. The shear stress acting on a cuttings bed has a direct relationship with fluid velocity. This means with an increase in fluid velocity, there is an increase in average cutting bed shear stress ($\bar{\tau}_{bed}$). However, the ill effects of a high-velocity flow are excessive Equivalent Circulating Density (ECD) and wellbore erosion. So, for drilling fluid to perform its primary function effectively and guarantee an efficient hole cleaning, hydraulic optimization and regular monitoring and control of drilling parameters

are required. Figure 1.2 shows a partially blocked eccentric annulus, with a blockage height '$H_{bed} = H/H_{max}$'. As the blockage increases, friction factor gets affected resulting in an increase in annular pressure loss. Thus, a better understanding of the effects of blockage on pressure loss and hole cleaning is essential.

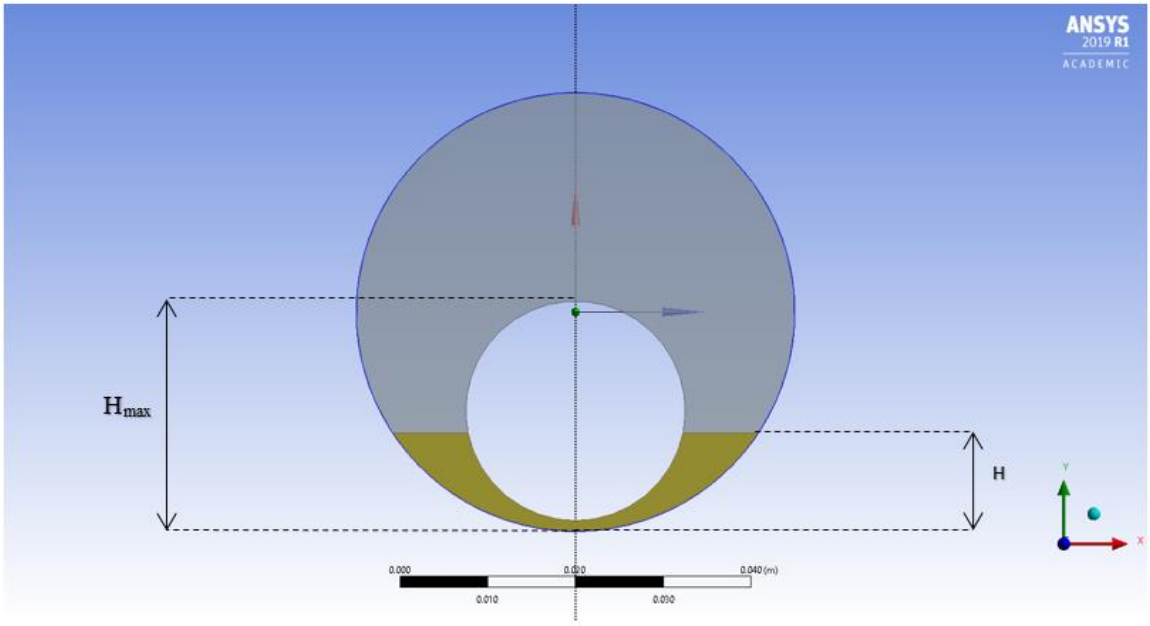

Figure 1.2. Partially blocked eccentric annulus

The presence of cutting bed complicates flow geometries; as a result, analytical results cannot be obtained. Numerical investigations are often applied in order to better understand the relationship among flow parameters such as flow rate, bed shear stress, and pressure loss relation. Previously, approximate models have been developed to predict hydraulic parameters in partially blocked annuli. In this study, CFD simulations have been performed to solve this complex flow problem by presenting accurate hydraulic models to optimize the hole cleaning process.

1.3 Objective

This study is aimed to better understand the flow non-Newtonian fluid in a partially blocked eccentric annulus under turbulent conditions, which is a common flow phenomenon observed in horizontal and inclined wells. In order to perform the flow analysis, various annular geometries are created and simulated using CFD software (ANSYS Fluent) aiming to better understand the effects of cutting bed on annular frictional pressure loss and cutting bed shear stress and formulate empirical correlations to calculate the bed shear stress.

1.4 Scope of Work and Methodology

This research involves CFD simulations in blocked eccentric annulus varying diameter ratio (κ), and cutting bed height (H_{bed}). Other than the geometric changes, flow rate, and drilling fluid rheological parameters have been varied during the simulation study. The power-law fluid parameters (consistency index (K) and power-law exponent (n)) have been varied to cover a wide range of drilling fluid properties. Validation is performed by comparing CFD simulation results with already published experimental measurements and the predictions of existing models. Furthermore, the CFD results have been analyzed and used to develop an empirical model for predicting bed shear stress and pressure loss.

1.5 Outline

This thesis comprises of six sections. Chapter 1 states the study objectives, problem statement, and the methodology used in the investigation. Chapter 2 presents past and recent studies conducted in the field of wellbore hydraulics. It provides a comprehensive review of

experimental, modeling and theoretical studies. Chapter 3 introduces the concept of turbulent flow modeling, especially in pipes and annuli. It also introduces the governing equations utilized in the CFD model. Chapter 4 introduces the techniques of CFD, which are used in simulating the steady-state flow of power-law fluid in the partially blocked annulus. The boundary conditions implemented and the grid-independent study performed. Chapter 5 presents simulated results in the form of graphs and plots and related discussions along with comparisons with published results and predictions of existing models. Finally, Chapter 6 summarizes the relevant outcomes of the study that can improve the knowledge base of the drilling technology and provides a few recommendations for future studies.

Chapter 2

Literature Review

In this chapter, a review of the existing literature is summarized. The chapter also presents an insight into various flow parameters, and how they have been incorporated in the simulation software with the advancement of computational tools. Fundamental knowledge in these concepts is essential as they form the foundation for this study and help in the 3-D analysis of the model.

Drilling engineers, on a routine basis, deal with the flow of drilling fluid in annular space formed between the drill pipe and casing or wellbore. A review of technical literature provides a comprehensive understanding of the annular flow in the wellbore. In wellbore hydraulic analysis, often the velocity profile or pressure drop is analyzed assuming the drill pipe is placed concentrically. However, in horizontal, inclined, and extended reach wells, the drill pipe is positioned in a fully eccentric configuration. As a result of eccentricity, the annular frictional loss pressures are generally lower than anticipated, resulting in a reduced ECD. Furthermore, with the introduction of new drilling technologies like underbalanced drilling and managed pressure drilling, the accurate prediction of ECD becomes crucial for the successful completion of drilling projects.

A number of rheological models have been used to model the flow behavior of non-Newtonian fluids in eccentric annuli. Two and three-parameter rheological models are often used to describe the flow behavior of drilling fluid. The three-parameter model known as the Yield power-law (YPL) model proposed by (Herschel and Bulkley, 1926; Ahmed and Miska, 2008) is widely used throughout the industry to perform accurate pressure loss predictions. Two parameter models like power-law and Bingham also provide reasonable predictions. For further refinement

and better resolution of flow behaviors, four to five parameter models have also been tested but are not widely used in practice due to the complexity in the calculation of pressure loss and other flow parameters. In this study, the power-law model is selected for the investigation.

A review of technical literature reveals that a number of studies have been conducted on the flow of non-Newtonian fluids in concentric and eccentric annuli under laminar and turbulent flow conditions. The studies are discussed in later sections to provide a brief insight into analytical, experimental and numerical modeling and hydraulic analysis of these flows.

2.1 Concentric Annuli

There are a number of studies conducted on the flow of power-law and Bingham plastic fluid in concentric annuli. To obtain a laminar flow solution, the non-linear governing equation needs to be solved analytically or numerically. There is no exact analytical solution for turbulent or laminar flow non-Newtonian fluids in concentric and eccentric annuli (Gucuyener and Mehmetoğlu, 2004). It was observed that a numerical integration is necessary to obtain an exact solution for a concentric annulus. In order to avoid the numerical procedure, the narrow slot approximation is utilized. For a diameter clearance greater than 0.3 ($\kappa > 0.3$) the narrow slot approximation (Fig. 2.1) provides a reasonably accurate solution for concentric annuli (Bourgoyne, 1991). It is not accurate for eccentric annuli. Nonetheless, it is used to estimate pressure loss in narrow eccentric annuli with low eccentricity (Iyoho and Azar, 1981).

In-depth research into concentric annular flow has led to the development of various models that are applicable to laminar and turbulent flow regimes. The comparison of numerical results with experimental data for non-Newtonian fluid in both concentric and eccentric annuli demonstrated good agreement (Escudier et al., 2000). Also, the turbulent flow of non-Newtonian

fluids in annular geometry with blockage has been extensively studied experimentally and theoretically (Nouri et al., 1993; Hussain and Sharif, 1997; Ahmed and Miska, 2009).

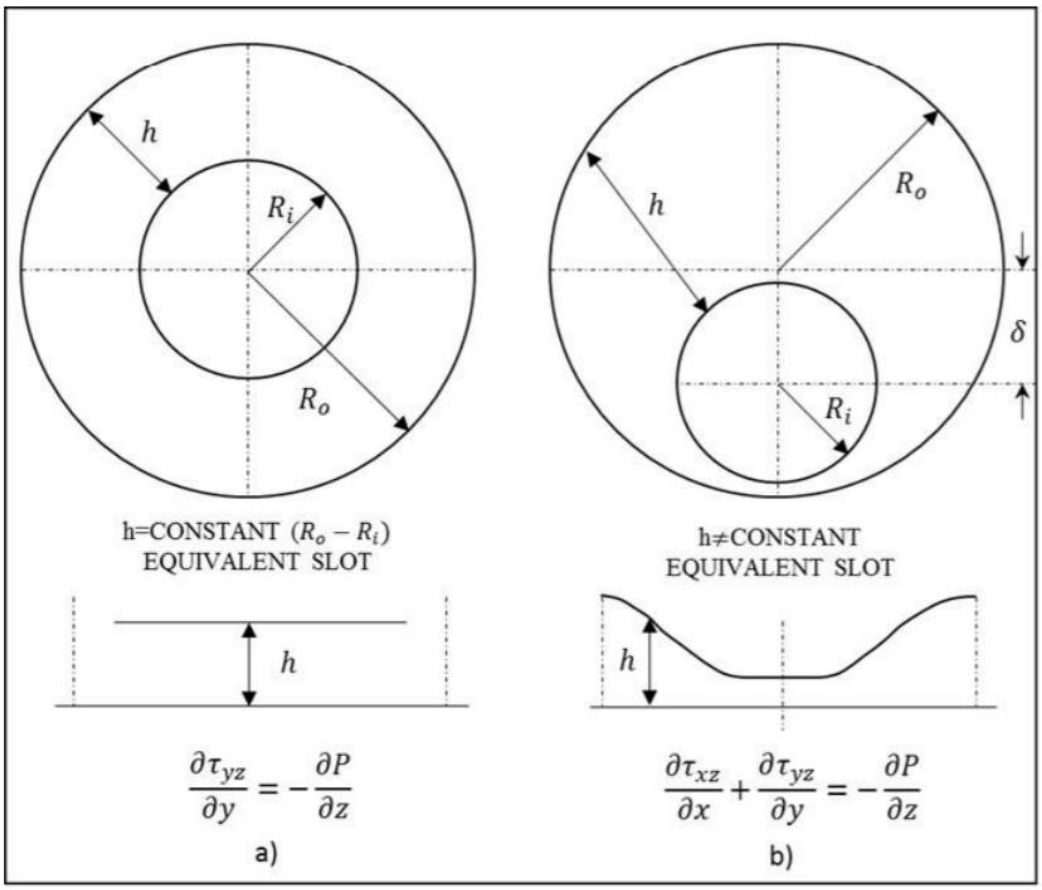

Figure 2.1. Equivalent slot for annulus (Haciislamoglu, 1989)

$$A = \pi(R_o^2 - R_i^2)$$
$$= \bar{W}h \qquad (2.1)$$

where, $\bar{W}$ is the width and h is the height of the slot

2.2 Eccentric Annulus

The flow domain in the eccentric annulus is not easy to describe mathematically, especially using the classical Cartesian coordinate system. To account for its irregular shape, a bipolar coordinate system is utilized along the cross-sectional plane of the annular pipe (Ebrahim et al., 2013; Heyda, 1959; Snyder and Goldstein, 1965). The bipolar coordinate system consists of two orthogonal systems of circles (Fig. 2.2) that provide an excellent alternative to determine velocity, pressure loss, and the flow rate in an eccentric annulus. In this coordinate system, the two circular boundaries coincide, i.e., the two cylindrical surfaces have a constant value of '$\eta_{o,i}$'. This constant is expressed in terms of dimensionless eccentricity and radius ratio. Various eccentricities shown on the y-axis are represented by different 'ξ' values, which intersect the boundaries on the annulus orthogonally. Speigel (Speigel, 1968) provided a relationship to transform cartesian coordinate to bipolar coordinate by the following relations (Ebrahim et al., 2013; Liu et al., 1999).

$$x = \frac{a_{bi} sinh\eta}{cosh\eta - cos\xi} \tag{2.2}$$

$$y = \frac{a_{bi} sin\eta}{cosh\eta - cos\xi} \tag{2.3}$$

where a_{bi} is bipolar coordinate system on the x-axis

$$a_{bi} = r_i sinh\eta_i = r_o sinh\eta_o \tag{2.4}$$

and

L_{third} is the third axis, which is perpendicular to η . Also,

$$\eta_i = \cosh^{-1}\left[\frac{(1+\kappa) - e^2(1-\kappa)}{a_{bi}e\kappa}\right] \tag{2.5}$$

$$\eta_o = \cosh^{-1}\left[\frac{(1+\kappa) - e^2(1-\kappa)}{a_{bi}e}\right] \tag{2.6}$$

The above set of relationships are necessary as they incorporate the circular pipe boundaries into the bipolar coordinate system, for the limits of $0 \leq \eta \leq 2\pi$ and $-\infty \leq L_{third} \leq \infty$

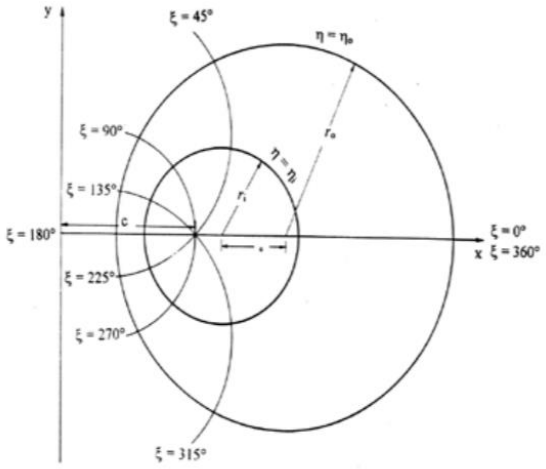

Figure 2.2. Eccentric annulus in bipolar coordinates (Haciislamoglu, 1989)

In various domains of engineering, fluid flow in eccentric annulus has caught much attention. In the past, modeling investigations of turbulent heat and mass transfer through pipes were conducted (Deissler, 1955) and model predictions are found to be in good agreement with experimental results. Later, the study was extended to the eccentric annulus (Deissler and Taylor, 1955). Jonsson and Sparrow (1965) also performed experimental work regarding turbulent flow in an eccentric annulus. They proposed a friction factor that reduces with an eccentricity (Jonsson and Sparrow, 1966).

Using bipolar coordinate transformation, modeling studies developed solutions (Eq. 2.7) for turbulent flow in an eccentric annulus. Predictions are compared with experimental measurements and found to be in good agreement (Ogino et al., 1987).

$$Q = \left[\left(\frac{dP}{dL}\right)_{c,e} \frac{r_o^{3n+1}}{K}\right]^{\frac{1}{n}} Q_{D(c,e)} \tag{2.7}$$

where

Q = Dimensionless flow rate

$Q_{D(c,e)}$ = Dimensionless flow rate for concentric or eccentric annulus

K = Fluid consistency index

$\left(\frac{dP}{dL}\right)$ = Frictional pressure loss gradient

Another recent model (Pilehvari and Serth, 2009) predicts pressure loss of non-Newtonian fluid in concentric and eccentric annuli utilizing the effective diameter concept A numerical study (Cui and Liu, 1995) solved the continuity and momentum equations and found an increase in secondary flow with eccentricity. Analysis carried out by McCann et al., (1995), which used flow loop measurements found that pressure loss of a power-law fluid decreases significantly with eccentricity. Haciislamoglu and Langlinsia (1990) also performed numerical and analytical analyses and developed widely used correlations (Eqs. 2.8 and 2.9) to relate pressure drop of a concentric annulus to that of an eccentric annulus and estimate the pressure loss of power-law fluid. These correlations are valid for a fluid behavior index of 0.4 to 1.0, eccentricity range of 0 to 0.95 and diameter ratio ranging between 0.3 to 0.9.

Laminar Flow Regime

$$\left(\frac{dP}{dL}\right)_{ecc} = \left(1 - 0.072\kappa^{0.8454}\frac{e}{n} - \frac{3}{2}e^2\sqrt{n}\kappa^{0.1852} + 0.96e^3\sqrt{n}\kappa^{0.2527}\right)\left(\frac{dP}{dL}\right)_{con} \quad (2.8)$$

Turbulent Flow Regime

$$\left(\frac{dP}{dL}\right)_{ecc} = \left(1 - 0.048\kappa^{0.8454}\frac{e}{n} - \frac{2}{3}e^2\sqrt{n}\kappa^{0.1852} + 0.285e^3\sqrt{n}\kappa^{0.2527}\right)\left(\frac{dP}{dL}\right)_{con} \quad (2.9)$$

where

$\left(\frac{dP}{dL}\right)$ = Frictional pressure loss gradient,

κ = Diameter ratio,

e = Dimensionless eccentricity

n = Fluid behavior index

Narrow slot flow models are utilized to present an approximate solution for the flow of a non-Newtonian fluid through the eccentric annulus (Iyoho and Azar, 1981; Uner et al., 1988; Tosun, 1984). A simplified model that determines the height (h) of the eccentric annulus is given by:

$$2h = \sqrt{r_o^2 - e^2 c_r^2 sin^2\theta} - r_i + e.c_r.cos\theta \quad (2.10)$$

where, c_r is the concentric radial clearance

When an annulus is very thin, its slot height can also be represented as

$$h = (r_o - r_i)(1 + e.cos\theta) \tag{2.11}$$

Iyoho and Azer (1981) along with most of their prior works in a similar domain concluded that eccentricity could dramatically reduce the annular pressure loss; thus, making its accurate estimation very critical. Piercy et al., (1993) provided an analytical solution for laminar Newtonian flow in eccentric annuli. They further went on to perform an experiential evaluation of the eccentric annular flow (Piercy et al., 1993). Also, recent studies (Rojas et al., 2017; Rojas, 2016) performed numerical simulation for the laminar flow of power-law fluid in the eccentric annulus. Other studies (Haciislamoglu and Langlinais, 1990; Haciislamoglu, 1989) performed numerical simulation in eccentric annuli by transforming the equation of motion into the bipolar coordinate system. A recent study (Fang et al., 1999) represented a set of equations by evaluating the effects of eccentricity on hydraulic parameters such as friction factor and Reynolds number. They are expressed as:

$$f = \frac{\left(\frac{dP}{dz}\right).D_h}{2\rho\bar{V}^2} \tag{2.12}$$

$$Re_{ecc} = \frac{\rho \bar{V}^{2-n} D_h^n}{K} \tag{2.13}$$

where f is fanning friction factor, Re_{ecc} is Reynolds number for eccentric annulus, $\frac{dP}{dz}$ is pressure gradient, D_h is hydraulic diameter, ρ is density, K is consistency index, $\bar{V}$ is mean fluid velocity, n is fluid behavior index.

For power-law fluid, the hydraulic parameter (fRe_{ecc}) is a function of eccentricity (e), fluid behavior index (n) and diameter ratio (κ). Numerous studies (Escudier et al., 2000; Ahmed et al., 2006) reported similar findings. Kozicki et al., (1966) proposed a generalized solution for non-circular duct flows. Dimensionless geometry parameters are utilized to determine pressure loss within ducts. The generalized Reynolds number (Re_g) is expressed as a function of the geometric parameters 'a' and 'b'. Thus:

$$Re_g = \frac{\rho \bar{V}^{2-n} D_h^n}{8^{n-1} K \left(\frac{a+bn}{n}\right)^n} \tag{2.14}$$

The values of the dimensionless geometric parameters are determined using the following equation:

$$a = \alpha_o {H_{bed}}^3 + \alpha_1 {H_{bed}}^2 + \alpha_2 H_{bed} + \alpha_3 \tag{2.15}$$

$$b = \alpha_o {H_{bed}}^3 + \alpha_1 {H_{bed}}^2 + \alpha_2 H_{bed} + \alpha_3 \tag{2.16}$$

where a_1, a_2, a_3,a_4, and α_o, α_1, α_2, α_3 are the coefficients of the correlations which are obtained (Ahmed et al., 2006) using published numerical results of Fang et al., (1999) and analytical solution presented for a Newtonian fluid. For a partially blocked eccentric annulus the expressions for the correlations are presented in Table 2.1 (Rojas et al., 2017).

Table 2.1. Geometric Parameters a and b

$a_o = -6.2328\kappa^2 + 4.1994\kappa - 0.8453$	$\alpha_o = -0.964\kappa^2 + 5.425\kappa - 1.3217$
$a_1 = 9.152\kappa^2 - 6.7796\kappa + 1.1096$	$\alpha_1 = -0.1792\kappa^2 - 8.1756\kappa + 2.0884$
$a_2 = -3.236\kappa^2 + 2.778\kappa - 0.0881$	$\alpha_2 = 0.836\kappa^2 + 3.4122\kappa - 0.9325$
$a_3 = 0.284\kappa^2 - 0.4266\kappa + 0.06684$	$\alpha_3 = 0.2456\kappa^2 - 0.2934\kappa + 0.8761$

2.3 Blocked Annulus

The fluid velocity is very low in the narrow zones of a block annulus (Nouri et al., 1993; Brighton and Jones, 1964; Jonsson and Sparrow, 1966). This reduced velocity is not enough to provide an effective hole cleaning. As a result, in horizontal or highly inclined wells, solids bed (blockages) form in the narrow zones of the annular area. Since the flow in a partially blocked annulus is complicated; there is no exact analytical solution. Thus, solutions are obtained using numerical procedures.

Several numerical studies have been performed to better understand the relationship between flow parameters such as blockage, flow rate, and pressure gradient. Numerical studies are performed by applying the finite difference method and using a curvilinear boundary fitted coordinate system (Clark and Bickham, 1994; Li et al., 2007). A review of technical papers revels

that many hydraulic models have been developed to better understand the influence of fluid flow in a blocked annulus (Sorgun, 2011; Yue et al., 2008). Other studies (Rojas, 2016; Rojas et al., 2017, Aworunse, 2012) developed a hydraulic model and performed extensive simulations to obtain a correlation between geometric parameters 'a' and 'b' in a highly eccentric (0.8 and 0.9) partially blocked annuli (Table 2.1). The correlations help predict frictional pressure loss. The geometric parameters are expressed as a function of fluid behavior index, dimensionless bed height, diameter ratio and eccentricity. Recent studies demonstrated the capability of using CFD to observe and understand complex fluid flow in the wellbore (Sorgun, 2011; Sorgun et al., 2018). CFD solutions have shown good agreement with experimental measurements (Rojas et al., 2017; Tang et al., 2016; Azouz et al., 1993).

2.4 Computational Fluid Dynamics

CFD is generally used to study fluid motion and heat transfer by solving the governing equations using a solver. CFD software (ANSYS Fluent) provides accurate predictions of fluid interactions between both fluid-fluid and wall-fluid interfaces. It eliminates the need for prototype generation (develop large physical models) or just laboratory experiments (ANSYS, 2019). In the petroleum industry, fluid flow analysis in a wellbore is very crucial. Parameters such as pressure loss, wall shear stress and the impact of blockage and fluid velocity variation can be accurately determined with the help of CFD. In the past, studies (Escudier et al., 2000; Fang et al.,1999; Sorgun, 2011; Singh and Samuel, 2009) have been performed in concentric and eccentric annuli considering laminar and turbulent flow conditions. Experimental measurements have been compared with numerical simulation and found to be in agreement.

Chapter 3

Theory of Turbulent Flow

3.1 Turbulent Flow Modeling

The Navier-Stokes equations govern fluid motion and derive its roots from Newton's second law of motion for fluids. The equations represent the conservation of momentum, while the continuity equation describes mathematically the conservation of mass. These equations (Eqs. 3.1 to 3.4) form the heart of fluid flow modeling for simple and complex geometries. Solving these equations for particular boundary conditions (like the inlet, the outlets, and the walls) helps in predicting the velocity profile and understand pressure distribution in a given flow geometry. The flow of blood in arteries, airflow over an automobile, and fluid flow in rivers are all governed by these equations. The Navier-Stokes equation in the cartesian coordinate system can be expressed as:

Continuity Equation

$$\frac{\partial \rho}{\partial t} + \nabla.\left(\rho\, \vec{V}\right) = 0 \qquad (3.1)$$

where ρ = Fluid density, t = Time, $\vec{V}$ = Flow velocity vector field, $\nabla.\left(\rho u\vec{V}\right), \nabla.\left(\rho v\vec{V}\right),$ $\nabla.\left(\rho w\vec{V}\right)$ = Momentum convection.

Momentum Equation

Component in X-direction

$$\rho\left(\frac{\partial(u)}{\partial t}+u\frac{\partial(u)}{\partial x}+v\frac{\partial(u)}{\partial y}+w\frac{\partial(u)}{\partial z}\right)=-\frac{\partial p}{\partial x}+\frac{\partial \tau_{xx}}{\partial x}+\frac{\partial \tau_{yx}}{\partial y}+\frac{\partial \tau_{zx}}{\partial z}+\rho f_x \tag{3.2}$$

Component in Y-direction

$$\rho\left(\frac{\partial(v)}{\partial t}+u\frac{\partial(v)}{\partial x}+v\frac{\partial(v)}{\partial y}+w\frac{\partial(v)}{\partial z}\right)=-\frac{\partial p}{\partial y}+\frac{\partial \tau_{xy}}{\partial x}+\frac{\partial \tau_{yy}}{\partial y}+\frac{\partial \tau_{zy}}{\partial z}+\rho f_y \tag{3.3}$$

Component in Z-direction

$$\rho\left(\frac{\partial(w)}{\partial t}+u\frac{\partial(w)}{\partial x}+v\frac{\partial(w)}{\partial y}+w\frac{\partial(w)}{\partial z}\right)=-\frac{\partial p}{\partial z}+\frac{\partial \tau_{xz}}{\partial x}+\frac{\partial \tau_{yz}}{\partial y}+\frac{\partial \tau_{zz}}{\partial z}+\rho f_z \tag{3.4}$$

where u, v, w are local fluid velocity in x, y, and z-axis, ρ is fluid density, $\frac{\partial p}{\partial x}, \frac{\partial p}{\partial y}, \frac{\partial p}{\partial z}$ are pressure gradient, $\frac{\partial \tau_{ij}}{\partial x}, \frac{\partial \tau_{ij}}{\partial y}, \frac{\partial \tau_{ij}}{\partial z}$ are viscosity-dependent momentum exchange terms, and ρf_i is body force (gravity in x, y, and z-direction).

Direct numerical simulation of turbulent flow using the Navier-Stokes equations is computational challenging. As a result, approximate models are used for practical applications. In the development of approximate models for the Navier-Stokes equation, a variety of modeling approaches have been established. One of the approaches used the Reynolds-averaged Navier–Stokes equations (RANS) that help model turbulent flows in ducts and open channels. The mathematical technique behind solving this time-averaged RANS equation is the Reynolds decomposition. The technique is developed to separate the steady component of the equation from the fluctuating ones. The steady component can be a time-averaged component (steady with time).

The RANS equation is primarily used to describe turbulent flow in uniform ducts. It is widely used in industrial flow applications.

Component in X-direction

$$\frac{\partial(\rho UU)}{\partial x}+\frac{\partial(\rho VU)}{\partial y}+\frac{\partial(\rho WU)}{\partial z} = -\frac{\partial \bar{p}}{\partial x}+\frac{\partial}{\partial x}\left[\mu_{eff}\frac{dU}{dx}\right]+\frac{\partial}{\partial y}\left[\mu_{eff}\frac{dU}{dy}\right]+\frac{\partial}{\partial z}\left[\mu_{eff}\frac{dU}{dz}\right]+S_U \quad (3.5)$$

Component in Y-direction

$$\frac{\partial(\rho UV)}{\partial x}+\frac{\partial(\rho VV)}{\partial y}+\frac{\partial(\rho WV)}{\partial z} = -\frac{\partial \bar{p}}{\partial y}+\frac{\partial}{\partial x}\left[\mu_{eff}\frac{dV}{dx}\right]+\frac{\partial}{\partial y}\left[\mu_{eff}\frac{dV}{dy}\right]+\frac{\partial}{\partial z}\left[\mu_{eff}\frac{dV}{dz}\right]+S_V \quad (3.6)$$

Component in Z-direction

$$\frac{\partial(\rho UW)}{\partial x}+\frac{\partial(\rho VW)}{\partial y}+\frac{\partial(\rho WW)}{\partial z} = -\frac{\partial \bar{p}}{\partial z}+\frac{\partial}{\partial x}\left[\mu_{eff}\frac{dW}{dx}\right]+\frac{\partial}{\partial y}\left[\mu_{eff}\frac{dW}{dy}\right]+\frac{\partial}{\partial z}\left[\mu_{eff}\frac{dW}{dz}\right]+S_Z \quad (3.7)$$

where $\mu_{eff} = \mu + \mu_t$, where U, V, W are time-averaged local fluid velocity. $\bar{p}$ is time-averaged pressure. S_U, S_V, and S_W are additional source terms due to the non-uniform viscosity.

3.1.1 Two Equation: k-ε Model

The k-ε model is the most widely used model in simulating mean flow characteristics for turbulent duct flows. The model comprises two differential equations to describe turbulence. The original motivation of this model was to enhance the Prandtl mixing-length approach. The k-ε model has been successfully used in simulating turbulent flow in uniform ducts. According to this model, the differential equation that describes the distribution of turbulent kinetic energy is expressed as:

$$\frac{\partial(\rho k)}{\partial t} + \frac{\partial(\rho k u_i)}{\partial x_i} = \frac{\partial}{\partial x_j}\left[\left(\mu + \frac{\mu_t}{\sigma_k}\right)\frac{\partial k}{\partial x_j}\right] + G_k + G_b - \rho\varepsilon - Y_M + S_k \tag{3.8}$$

Similarly, the equation used to describe the distribution of the rate of turbulent energy dissipation (ε) is given as:

$$\frac{\partial(\rho \varepsilon)}{\partial t} + \frac{\partial(\rho \varepsilon u_i)}{\partial x_i} = \frac{\partial}{\partial x_j}\left[\left(\mu + \frac{\mu_t}{\sigma_\varepsilon}\right)\frac{\partial \varepsilon}{\partial x_j}\right] + C_{1\varepsilon}\frac{\varepsilon}{k}(G_k + C_{3\varepsilon}G_b) - C_{2\varepsilon}\rho\frac{\varepsilon^2}{k} + S_\varepsilon \tag{3.9}$$

The Reynolds stresses within the fluid are obtained by performing the averaging operation. The averaging is performed over the Navier–Stokes equations and accounts for turbulent changes (fluctuations) in a fluid motion. These non-linear stress terms are responsible for the creation and growth of the turbulence in turbulent flows. In the k-ε model, the Reynolds stress is determined using an eddy viscosity (μ_t) model, which is expressed as:

$$\mu_t = \rho C_\mu \frac{k^2}{\varepsilon} \tag{3.10}$$

where k is turbulent kinetic energy, ε is the rate of dissipation, G_k is turbulent kinetic energy due to mean velocity gradient, G_b is turbulent kinetic energy due to buoyancy, Y_M is fluctuating dilatation in incompressible turbulence to overall dissipation rate, $\sigma_k, \sigma_\varepsilon$ is a turbulent Prandtl number for k and ε, $C_{1\varepsilon}$, $C_{2\varepsilon}, C_{3\varepsilon}, C_\mu$ are constants. Furthermore, the turbulent Prandtl numbers and the constants have the following values:

$$C_{1\varepsilon} = 1.44, C_{2\varepsilon} = 1.92, C_\mu = 0.09, \sigma_k = 1.0, \sigma_\varepsilon = 1.3$$

3.1.2 Model Assumptions

In order to perform the necessary CFD simulation for wellbore flow analysis, the required assumptions need to be made to simplify the Navier-Stokes equations. The following list of assumptions are made in performing the wellbore flow dynamic analysis:

- Fully developed turbulent flow of power-law fluid
- Steady-state and isothermal flow condition (time-independent)
- Incompressible fluid
- Non-rotating inner cylinder/pipe
- Flow-rate condition at the inlet is constant (uniform flow distribution)
- No-slip boundary condition at bed interface
- The bed is uniform and stable
- Negligible effect of solids on flow dynamics
- Smooth pipe wall

3.1.3 Power-law Fluid

The power-law model that relates shear stress and shear rate is given in Eq. (3.11). It is the most widely used empirical relationship in drilling engineering applications.

$$\tau = K\dot{\gamma}^n \tag{3.11}$$

where τ is shear stress, K is consistency index, n is fluid behavior index, and $\dot{\gamma}$ is the shear rate. Also, the above relationship can be rewritten in terms of apparent viscosity as follows:

$$\tau = \mu(\dot{\gamma})\dot{\gamma} \tag{3.12}$$

where $\mu(\dot{\gamma})$ is apparent viscosity, which is a function of shear rate, $\dot{\gamma}$. When the fluid becomes non-Newtonian, an additional relationship between shear rate and velocity gradient is required. Hence, the apparent viscosity of non-Newtonian fluids is related to the generalized shear rate expressed as:

$$|\dot{\gamma}|^2 = 2\left[\left(\frac{\partial u}{\partial x}\right)^2 + \left(\frac{\partial v}{\partial y}\right)^2 \left(\frac{\partial w}{\partial z}\right)^2\right] + \left(\frac{\partial u}{\partial y} + \frac{\partial v}{\partial x}\right)^2 + \left(\frac{\partial v}{\partial z} + \frac{\partial w}{\partial x}\right)^2 + \left(\frac{\partial v}{\partial z} + \frac{\partial w}{\partial y}\right)^2 \tag{3.13}$$

where $\dot{\gamma}$ is shear rate, u, v, w are local fluid velocities in x, y, and z-axis. The term $\mu(\dot{\gamma})$ is defined as a ratio between shear stress and the shear rate. This relationship helps in the understanding of the flow behavior of fluids. In Eq. (3.11), one can vary the value of 'n' and observe the relationship between apparent viscosity and shear rate. If 'n' is less than one, fluid is said to have a pseudo-plastic behavior, i.e.; it exhibits shear thinning property. If 'n' is greater than one, the fluid is considered as dilatant fluid (i.e., it shows a shear thickening behavior). In the first case, the

apparent viscosity decreases with shear rate and in the latter case, it is found to increase with the shear rate. For a case of n = 1, the fluid is said to behave like a Newtonian fluid. Figure 3.2 represents the discussed behavior with respect to apparent viscosity.

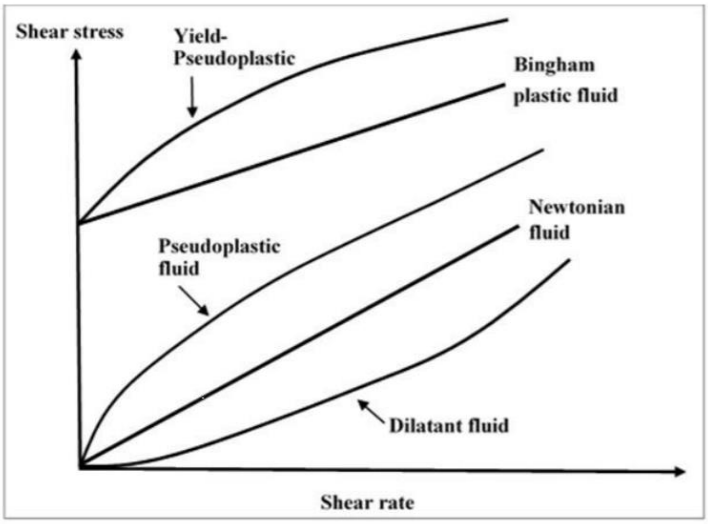

Figure 3.1. Non-Newtonian fluid types (Nguyen and Nguyen, 2012)

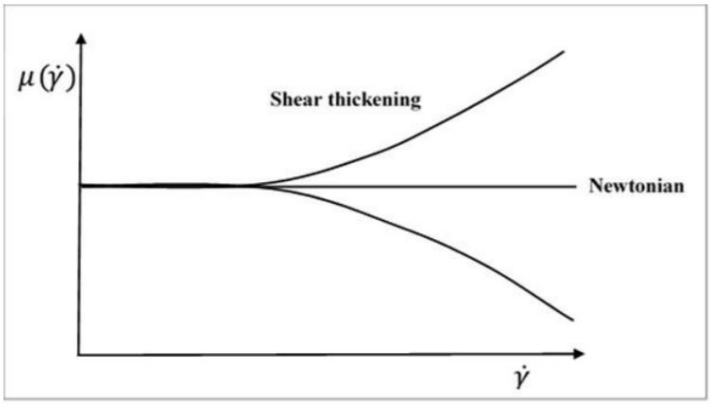

Figure 3.2. Viscosity vs shear rate (Willenbacher and Georgieva, 2013)

3.2 Relevant Flow Parameters

The Reynolds number and friction factor are very important dimensionless parameters used in the hydraulic calculation. These parameters are required to determine the average wall shear stress and pressure loss in non-circular ducts.

3.2.1 Reynolds Number

Fluid flow in a uniform duct can be in one of the three flow regimes, namely, laminar, transition and turbulent. The Reynolds number is a dimensionless number that compares the inertia force to the viscous force. It is used to determine if the flow is under laminar or turbulent condition (Holland, 1995). Thus, the Reynolds number is given as:

$$Re = \frac{Inertia\ Force}{Viscous\ Force} \tag{3.14}$$

If a fluid flow is streamlined and highly ordered (Figure 3.3), it is considered to be in laminar and in this case, the Reynolds number range between 0 and 2100. This range is applicable only for Newtonian fluid in a circular pipe. Lower ranges of Reynolds number means the viscous forces are dominant as compared to the inertia forces, which characterizes by a smooth fluid flow behavior. At higher Reynolds numbers (Re > 4000), the flow regime is said to be turbulent. In this case, the flow is mostly dominated by inertia forces and a large number of eddies are generated (Figure 3.4), resulting in velocity fluctuations and disordered fluid streamlines (motion). The regime between laminar flow and turbulent flow is called the transition flow and occurs within a Reynolds number range of 2100 to 4000. The Reynolds number in an eccentric annulus is given by Equation 2.13 (Kozicki et al., 1966). The hydraulic diameter is necessary for the determination

of the Reynolds number in an eccentric annulus. For any non-circular duct, the hydraulic diameter, $D_h = 4A/P_W$, where P_W is the wetted perimeter of the duct and A is the cross-sectional area of the duct.

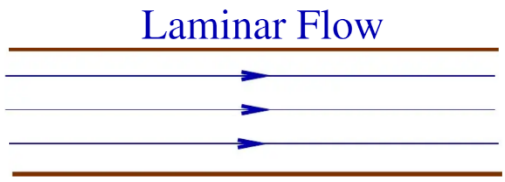

Figure 3.3. Laminar flow streamlines in a pipe (Purushothaman, 2019)

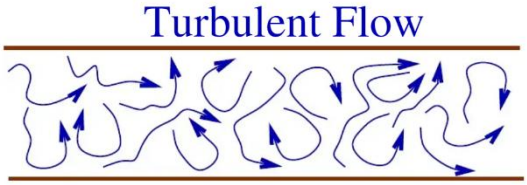

Figure 3.4. Turbulent flow streamlines in a pipe (Purushothaman, 2019)

In literature, there are published correlations that follow a power-law model. The Dodge and Metzner (Dodge and Metzner, 1959) have published turbulent flow correlations for an annular flow which have gained widespread acceptance in the petroleum industry. The correlations are limited to smooth pipes and were developed by incorporating the apparent viscosity and the effective diameter into the Reynolds number equation (Bourgoyne, 1991). The Reynolds number is given as follows.

$$Re^* = \frac{109{,}000\rho\bar{V}^{(2-n)}}{K}\left[\frac{0.0282(D_o - D_i)}{2 + 1/n}\right]^n \tag{3.15}$$

Note: In this research, the difference $(D_o - D_i)$ is replaced by the hydraulic diameter (D_h) and Re^* represents the Reynolds number for turbulent annuli flow using the power-law model.

3.2.2 Fanning Friction

Pressure losses in pipe encountered during a fluid flow occur as a result of hydraulic friction resistance. Pressure losses in a tube or annular duct are a function of the Fanning friction factor (f), which is the ratio of average wall shear stress to the kinetic energy flow density. It is expressed as:

$$f = \frac{\tau_w}{\rho \frac{\bar{V}^2}{2}} \tag{3.16}$$

where f is fanning friction factor, τ_w is wall shear stress, ρ is corresponding fluid density, $\bar{V}$ is mean fluid velocity.

Turbulent flow in tubes

During turbulent flow within a round tube, an expression for friction factor was developed by Blasius (Equation 3.17). This relation has been found to work well for hydraulically smooth pipes when the Reynolds number is between 2100 and 10^5 (Klinzing et al., 2010; Holland, 1995).

$$f = \frac{0.0791}{Re^{0.25}} \tag{3.17}$$

For high Reynolds number (i.e. greater than 10^5) turbulent flows in smooth pipes, Koo (Klinzing et al., 2010; Holland, 1995) developed another explicit formula (Equation 3.18). This formula is applicable for a Reynolds number range of $10^4 < Re < 10^7$.

$$f = 0.0014 + \frac{0.125}{Re^{0.32}} \tag{3.18}$$

Also, a widely acceptable relationship applicable to a turbulent flow regime in hydraulically smooth pipes is given by the von Karman equation (Holland, 1995).

$$\frac{1}{\sqrt{f}} = 4.0 \log\left(\frac{1}{\sqrt{f}}.Re\right) - 0.40 \tag{3.19}$$

For pipes with a certain degree of roughness or experiencing complete roughness, the Fanning friction factor is calculated, taking into account the relative roughness factor ($^{\epsilon}/_{D}$). A relationship between roughness and friction factor for high Reynolds number flows ($4 \times 10^4 < Re < 10^7$) is given by (Haaland, 1983; Holland, 1995):

$$\frac{1}{\sqrt{f}} = -3.6 log_{10}\left[\frac{6.9}{Re} + \left(\frac{^{\epsilon}/_{D}}{3.7}\right)^{^{10}/_{9}}\right] \tag{3.20}$$

Another generalized relationship between Reynolds number and Fanning friction factor, for any turbulent range, is shown as follows (Colebrook and White, 1937).

$$\frac{1}{\sqrt{f}} = -2.0 \log_{10}\left(\frac{2.51}{Re\sqrt{f}} + \left(\frac{^{\epsilon}/_{D}}{3.7}\right)\right) \tag{3.21}$$

where ϵ is roughness of the inner surface of the pipe, and D is pipe diameter.

In non-Newtonian power-law fluids, the pipe roughness has a minor effect on pressure loss and friction factor. However, the Fanning friction factor is affected by the Reynolds number (Re) and fluid behavior index (n). Kozicki et al., (1966) presented a generalized friction factor correlation for the turbulent flow of power-law fluid in non-circular ducts. Thus:

$$\frac{1}{\sqrt{f}} = \frac{4}{n^{0.75}} \log_{10}\left(Re_g . f^{\frac{2-n}{2}}\right) - \frac{0.4}{n^{1.2}} + 4n^{0.25} . \log_{10}\left[\frac{4(a+bn)}{1+3n}\right] \quad (3.22)$$

where Re_g is the generalized Reynolds number defined in Eq. (3.22), where constant "a" and "b" are geometric parameters. The information given by Kozicki et al., (1966) suggests that a and b values obtained from a laminar flow can be used to determine the friction factor in turbulent flow regime using Eq. (3.22). Thus, the geometric correlations developed by Rojas et al., (2017) are used in this study to determine the turbulent friction factor in a partially blocked eccentric annulus.

3.2.3 Wall Shear Stress

As the fluid flows in pipes, there is shear stress developed on the surfaces of the conduit. The wall shear stress developed near the boundary wall is related to the friction pressure gradient. The wall shear stress in a pipe is determined from the pressure gradient as:

$$\tau_{w,p} = \frac{\mathrm{d}P}{\mathrm{d}L} . \frac{D}{4} \quad (3.23)$$

where $\tau_{w,p}$ is wall shear stress acting on the pipe wall, $\frac{\mathrm{d}P}{\mathrm{d}L}$ is the frictional pressure loss gradient of a fully developed flow, D is the diameter of a pipe. The maximum shear stress occurs at the pipe wall. For a fully developed pipe flow, the velocity profile is shown in Figure 3.5.

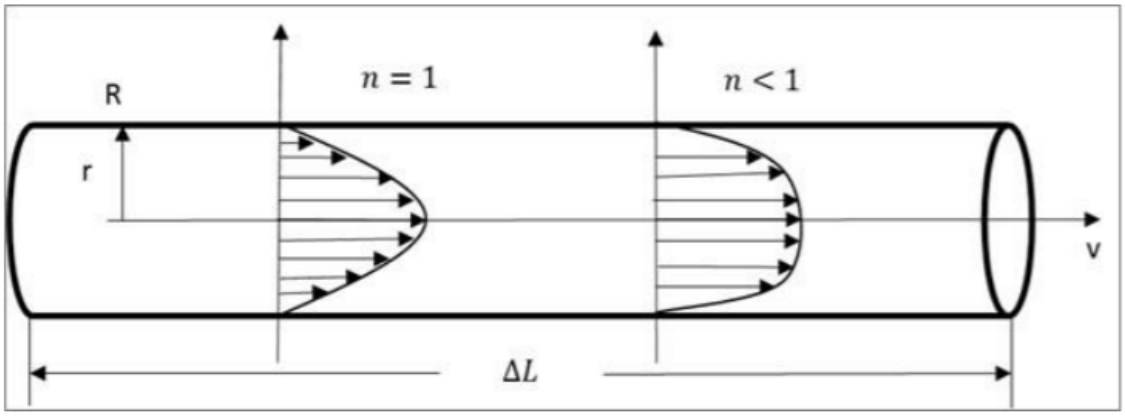

Figure 3.5. The velocity profile in a pipe (Rojas, 2016)

Theoretical analysis of a pipe flow resulted in the development of a generalized wall shear rate model, which expresses the relationship between wall shear rate and wall shear stress. Thus:

$$\dot{\gamma}_w = \left(\frac{8.\bar{V}}{D}\right).\left[\frac{3}{4} + \frac{1}{4}\frac{d\ ln\left(8.\bar{V}/_D\right)}{d\ ln\tau_w}\right] \tag{3.24}$$

where, $\dot{\gamma}_w$ is wall shear rate for generalized fluid and $\frac{8.\bar{V}}{D}$ is the nominal Newtonian shear rate. For power-law fluid, the term $\frac{d\ ln\left(8.\bar{V}/_D\right)}{d\ ln\tau_w}$ is expressed as 'n'. Thus, the wall shear stress for power-law fluid is expressed as:

$$\tau_w = \left(K\left(\frac{3n+1}{4n}\right).\frac{8\bar{V}}{D}\right)^n \tag{3.25}$$

A generalized wall shear stress model was proposed by Kozicki et al., (1966). The model is applicable for any arbitrary ducts that have a constant cross-section. In the case of power-law

fluid, the generalized wall shear stress is expressed as a function of fluid behavior index, nominal Newtonian shear rate and geometric parameters a and b. Hence:

$$\tau_w = K.\left[\frac{8.\bar{V}}{D_h}\left(b + \frac{a}{n}\right)\right]^n \tag{3.26}$$

The two geometric parameters (a and b) characterize the cross-section of the duct. In the case of fluid flow through a slot, the parameters a and b become $1/2$ and 1, respectively. For the case of pipe flow, the geometric parameters a and b are $1/4$ and $3/4$, respectively.

In the case of a concentric annulus, the wall shear stress acting on the inner and outer wall surfaces are not identical due to the difference in velocity profiles. Figure 3.6 shows the velocity profile in a concentric annulus. Figure 3.6 displays the case of a Newtonian flow; In the case of a power-law fluid, as the shear-thinning behavior of the fluid increases, the velocity profile is found to become flattered.

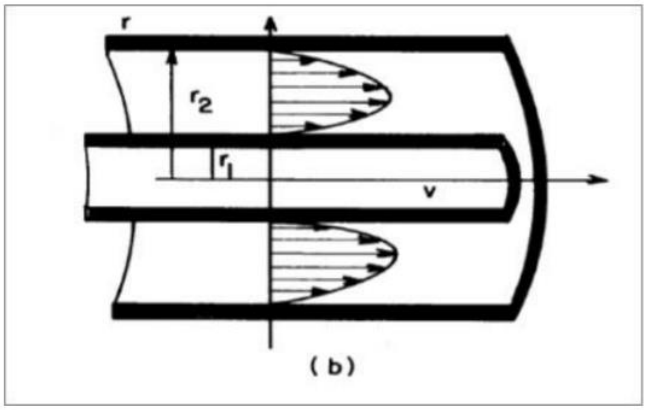

Figure 3.6. The velocity profile in a concentric annulus (Bourgoyne, 1991)

Applying the momentum balance for a slot based annular flow, the average wall shear stress is given by Equation 3.27.

$$\tau_{w,a} = \frac{\mathrm{dp}}{\mathrm{dz}} . \frac{D_h}{4} \tag{3.27}$$

where, $\tau_{w,a}$ is the wall shear stress of a concentric annular flow. The geometric constants of the concentric annulus vary with the diameter ratio (κ) and flow behavior index (n). Thus:

$$a + b = \frac{(1-\kappa)^n}{1 + \kappa^2 - \left(\frac{1-\kappa^2}{\ln\left({}^1/_\kappa\right)}\right)} \tag{3.28}$$

and,

$$a = \frac{(1-\kappa)^2}{4\left\{1 - \frac{1-\kappa^2}{2\ln\left({}^1/_\kappa\right)}\left[1 - ln\frac{1-\kappa^2}{2\ln\left({}^1/_\kappa\right)}\right]\right\}} \tag{3.29}$$

3.2.4 Hydraulic Parameter

For power fluid flowing in any uniform cross-section duct, the product of the generalized Reynolds number (Re_g) and the Fanning friction factor yields a constant 16. Thus: $f.Re_g = 16$. The friction factor is multiplied with the Reynolds number defined in Eq. (2.14), the value of the product varies with geometric constants, diameter ratio, eccentricity and fluid behavior index. Thus, for a given eccentricity and diameter ratio, the friction factor can be expressed as:

$$f = \frac{2^{3n+1}}{Re_{ecc}} . \left(\frac{a}{n} + b\right)^n \tag{3.30}$$

In the case of an eccentric annulus study, the geometric parameters are obtained by plotting the shape factor $\left(s = \left(\frac{fRe_{ecc}}{2^{3n+1}}\right)^{1/n}\right)$ as a function of 1/n for different eccentricities and diameter ratios (Fig. 3.7). As observed, the data points obtained from numerical simulation results from straight lines in s versus 1/n plot. The straight-line helps obtain the values for a and b.

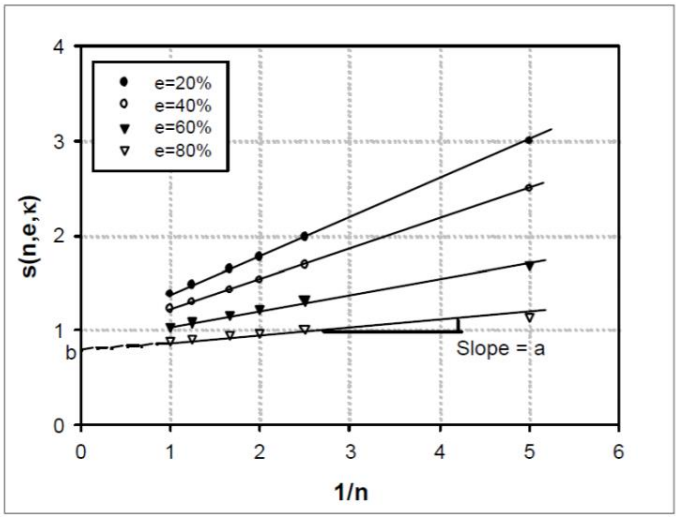

Figure 3.7. Shape factor for eccentric annular geometry (Ahmed et al., 2006)

3.2.5 Bed Shear Stress

In a partially blocked annulus, the presence of cuttings beds affects the flow pattern and the wall shear stress distribution. Thus, the shear stress acting on the beds (bed shear stress) determines the mobility of bed particles by affecting the lift and drag forces act on the bed. By determining the average bed shear stress and the pressure gradient across the annulus, one can evaluate hole cleaning performance in inclined and horizontal wells (Ahmed et al., 2003; George et al., 2014; Rojas et al., 2017). In the past, studies (Hussain and Sharif, 1997; Bicalho et al., 2016b) have conducted to better understand the effect of blockage on annular flows. Numerical

models have been developed to investigate the laminar flow in a partially blocked annulus for both Newtonian and non-Newtonian fluids. Azouz et al., (1993) analyzed the effect of blockage on annular flow and concluded that shear stress behavior is non-linear. The dimensionless bed shear stress (Rojas et al., 2017) can be another parameter that is used to better understand the fluid flow behaviors within an eccentric annulus. The dimensionless bed shear stress is defined as:

$$\pi_{bed} = \left(\frac{\bar{\tau}_{bed}}{\bar{\tau}_w}\right)^n \tag{3.31}$$

where π_{bed} is the dimensionless bed shear stress, $\bar{\tau}_w$ is the average wall shear stress, $\bar{\tau}_{bed}$ is the average bed shear stress. In this study, fluid parameters like power-law index and flow parameters such as bed height and diameter ratio are investigated and incorporated into one equation with the aim to develop a model for dimensionless bed shear stress.

The Fanning equation is the relation to calculate frictional pressure loss in pipes and annuli. All flow parameters are combined to eventually calculate the pressure gradient for the annular flow and the term pressure gradient is utilized to compare the CFD results with results obtained from existing models.

$$\frac{dP}{dL} = \frac{f\rho\bar{V}^2}{D_h} \tag{3.32}$$

3.3 Existing Models for Partially blocked eccentric annulus

The following are the two pre-existing models that are utilized in this study in order to compare the obtained CFD simulation results.

3.3.1 Hydraulic Diameter Model

The following are the steps followed in regard to the Hydraulic diameter model comparison.

- Mean flow velocity ($\bar{V}$) is an important input condition which is obtained by the ratio of flow rate (Q) with the cross-sectional area (A).
- Eq. 3.15 is used to calculate the Reynolds number to ensure flow is in turbulent regime and the Fanning friction factor (f) is calculated by using the Eq. 3.17.
- The hydraulic diameter (D_h) is calculated using the relationship $\mathrm{D}_h = 4\mathrm{A}/\mathrm{P}_W$, where P_W is the wetted perimeter and A is the cross-sectional area of the duct.
- Reynolds number (Re^*), is calculated by incorporating density (ρ), mean velocity ($\bar{V}$) and rheological parameters (n, K).
- The dimensional measurement in all cases are obtained using ANSYS software.
- Finally, the pressure gradient calculated by using Eq. 3.32. and the comparison of Hydraulic Model results with CFD results is displayed in section 5.7.

3.3.2 Kozicki's Model

The second model used to compare CFD result is the Kozicki's model (Kozicki et al., 1966).

- After the mean velocity ($\bar{V}$) is obtained from the flow rate (Q) and flow area (A).
- Geometric parameters (a and b) are obtained using correlations presented in Table 2.1. and Eq. 2.15 and 2.16 and incorporating the respective diameter ratio (κ).
- The generalized Reynolds number (Re_g) is then obtained by incorporating the above-mentioned a and b values into Eq. 2.14 along with mean velocity ($\bar{V}$), rheological parameters (n, K) and hydraulic diameter (D_h).
- This is needed to calculate the Kozicki's friction factor. The generalized Reynolds number and the geometric parameters are further incorporated into Eq. 3.22 to obtain Kozicki's friction factor value.
- Finally, the calculated mean velocity ($\bar{V}$), density (ρ), Fanning friction factor (f) and hydraulic diameter (D_h) are substituted into Eq. 3.32 to obtain the pressure gradient.
- The above-obtained pressure gradient is compared with simulation results in the form of plots and is shown in subsection 5.7.

Chapter 4

Computational Fluid Dynamics Analysis

In this chapter, a brief insight is given on the steps undertaken before beginning the simulation process and performing the post-processing operation in order to obtain reliable and meaningful results.

4.1 Geometry

An accurate description of flow geometry is a crucial step before the beginning of the CFD simulation. The flow geometries are created as 3-D models using the tool, ANSYS Design Modular, present within the workbench the commercial software. This tool is also used to incorporate various bed heights in the flow geometry, which is a crucial alteration necessary for this study to investigate the impact of blockage on pressure loss and wall shear stress. The 3-D flow geometries created during the study not only vary from one another in terms of bed height but also in diameter ratio ($\kappa = D_i/D_o$). Three different diameter ratios (0.25, 0.5 and 0.75) are considered along with various bed heights (0%, 10%, 30%, 50%, 70%, 90% and 100%). The eccentricity (e) in all the geometries remains fixed with a value of 0.9.

The bed height, length, and inlet area are accurately calculated, and the flow geometry is created accordingly. The annular area and wetted perimeter dimensions were calculated and confirmed using Chen's geometric analysis (Chen, 2005). A front view of the geometry comprising of solid blockage percentage is shown in Figure 4.1. Also, another front view of the geometry sliced by its symmetry axis for a fixed bed height of 50% with the three variations of diameter ratio is shown in Figure 4.2.

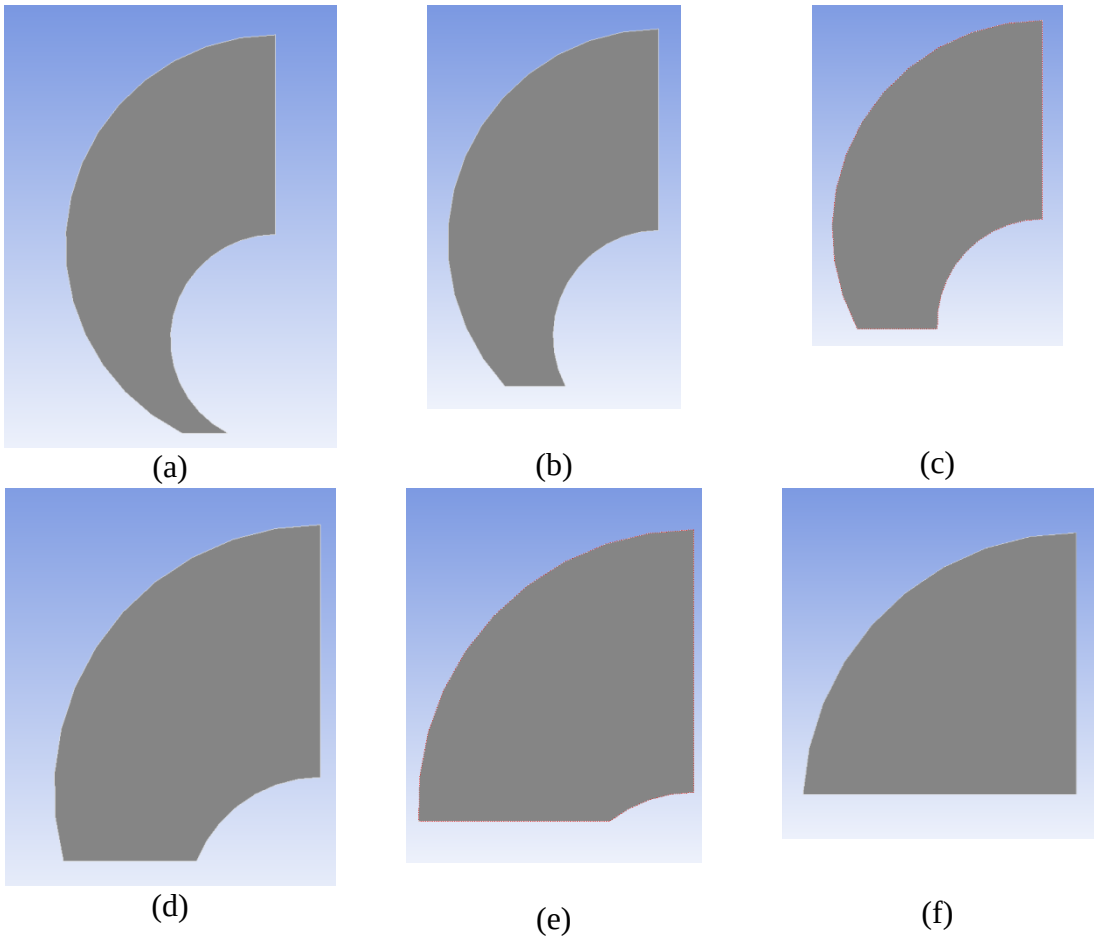

Figure 4.1. Front view of partially blocked annular geometry (κ = 0.50) (a) 10%, (b) 30%, (c) 50%, (d) 70%, (e) 90% and (f) 100%

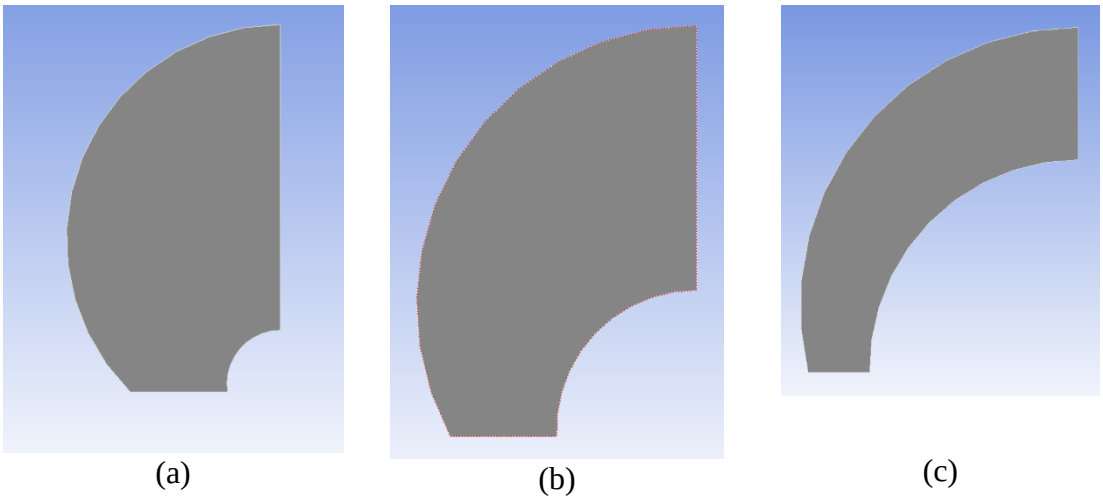

Figure 4.2. Front view of 50% blocked annular geometry with varying diameter ratio (a) κ = 0.25 (b) κ = 0.5 and (c) κ = 0.75

The flow geometry has five named faces, namely Inlet, Outlet, Outer Surface, and Inner Surface and Bed Surface, as shown in Figure 4.3. These named sections/faces along with the geometry, are imported in the mesh solver of ANSYS Workbench for mesh generation and grid refinement, an essential step for performing accurate CFD analysis.

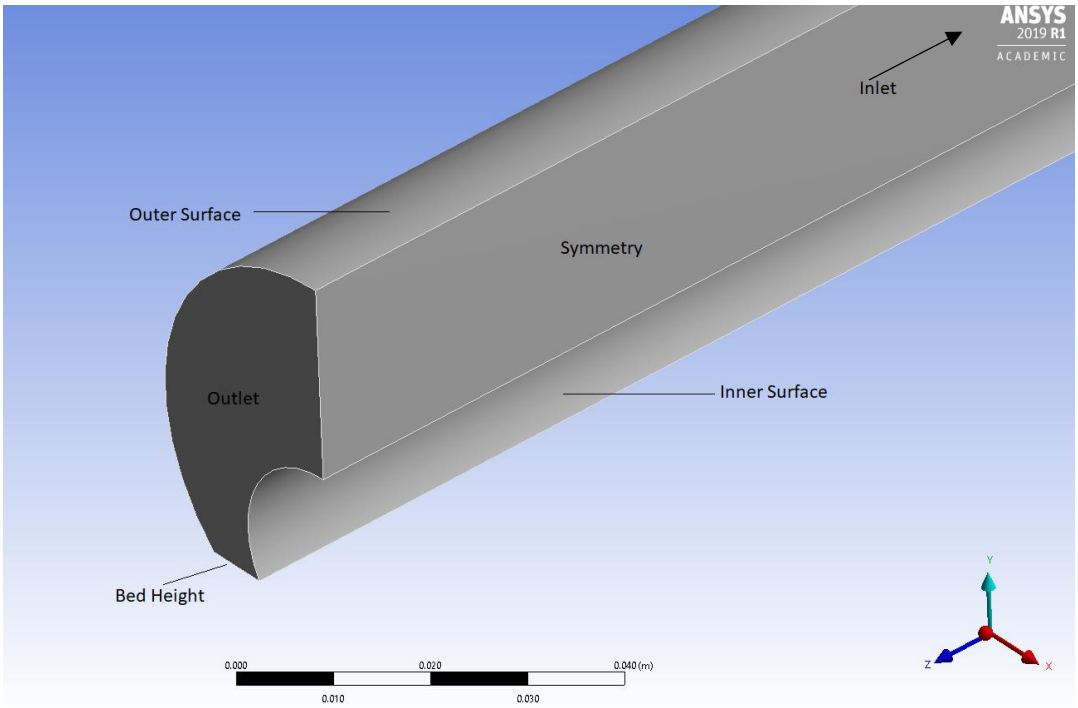

Figure 4.3. Named faces of the geometry

4.2 Mesh Generation

The second step after flow geometry creation is meshing, which is the generation of an appropriate grid (mesh) structure before performing any CFD simulation. The computational mesh is generated using the meshing tool present in ANSYS workbench. Grids are generated throughout the flow geometry and they represent the entire flow domain. There are mainly two major types of grid structures that are found in a meshing operation: structured grids and unstructured grids. The simplest type of grid is the structured grid. These kinds of grids are applicable in simple flow

geometries. In structured grids, the nodes are arranged in an orderly manner. An example of a simple structured grid is shown in Figure 4.4. On the other hand, an unstructured mesh (grid) system is used for a more complex flow geometry (flow domain). For example, in the case of a buried drill pipe, the solid bed area is critical and needs to be accurately represented. Similarly, the area close to the pipe wall is also very important due to very high-velocity gradient, so we need to have finer mesh at those interfaces. The fine grid layers created along the walls are shown with the unstructured grid (Figure 4.5).

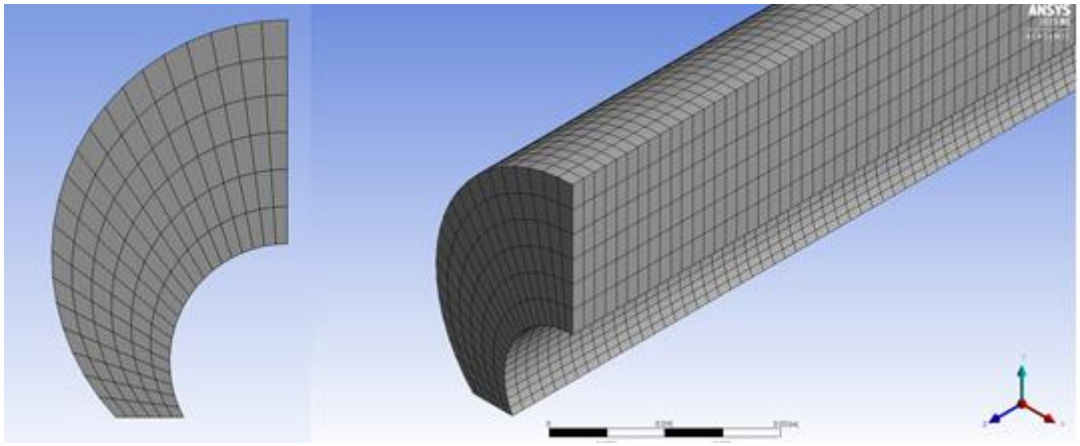

Figure 4.4. Example of structured grid

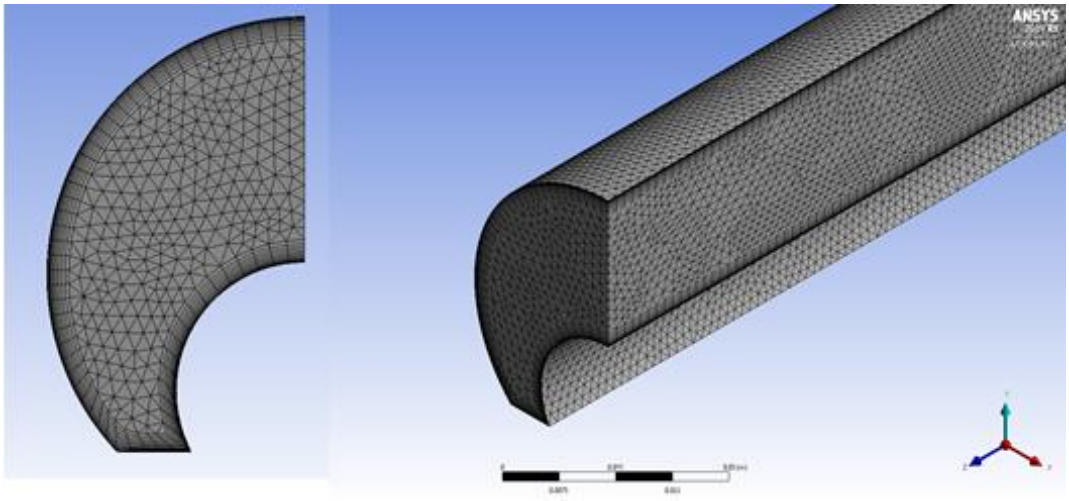

Figure 4.5. Example of unstructured grid

4.3 Boundary Conditions

Following the grid generation, it is of paramount importance to define the necessary boundary condition to represent the flow in the wellbore. As mentioned earlier, there are a total of five named surfaces, namely inlet, outlet, the outer surface, inner surface and bed surface. These surfaces are shown in Figure 4.3 and can be grouped into the following three subcategories.

Inlet (Fluid Inflow): The boundary condition at the inlet is defined as velocity inlet within ANSYS Fluent solver. The power-law fluid flows into the geometry through the inlet duct located on one end of the wellbore. The given inflow is specified at its upstream location and assumed to have a uniform flow rate of $5e^{-5}$ m^3/s.

Outlet (Fluid Outflow): The 3-D geometries outflow is directly opposite to the inlet surface (duct). It is defined as a pressure outlet boundary condition within the Fluent solver.

Wall Boundaries: The Outer Surface, Inner Surface, and Bed Surface are all defined as wall surfaces in ANSYS Fluent. These three surfaces use a no-slip wall condition and the volume enclosed by the three boundaries is considered as the flow domain.

The fluid flows into the flow domain through the inlet and leaves through the outlet. The bed height and bed shear stress are obtained by post-processing the numerical simulation results within ANSYS Workbench.

4.4 Grid Sensitivity Analysis

To perform any reliable CFD based numerical simulation comprising of 3-D geometry, just like a partially blocked annulus, adequately refined computational grid (mesh) generation is essential to ensure the solution accuracy. Numerical modeling of an eccentric annulus comprising

of blockages is generally complex. In such a domain, the horizontal length scale is larger than the vertical length scale. In order to avoid any numerical instability within the simulation process, a large number of grid points (mesh elements) are required to decrease the maximum aspect ratio of the grids, thereby (minimizing inaccuracy), ensuring the solution accuracy.

In this study, the unstructured grid system is selected for meshing the flow cross-sectional area. The mesh system comprises of tetrahedral, prism-like structures generated all along with the flow domain. In the axial direction, the annulus has been meshed with uniform grids containing tetrahedral elements and inflation lines have been used in the grid generator all along the solid bed and wall regions to better represent the wall effects. The total number of grid elements generated in the 3-D model is narrowed down using the grid refinement approach.

To perform a grid-independent study, a partially blocked annulus with a 30% bed height is considered. Mesh systems comprising of grid points (elements number) of 0.5M, 1.25M, 2.5M, and 5M are created. The final grid system is selected by analyzing and observing the pressure drop variation with the number of grids used in the simulation. The input variables, geometry dimensions and simulation conditions used for this analysis are shown in Table 4.1. Note that all simulations are performed under turbulent conditions (i.e., Reynolds number (Re^*) greater than 14000).

Table 4.1. Inputs for numerical simulation

Parameters	**Value**
Drill Pipe Diameter, D_i (m)	0.025
Casing Diameter, D_o (m)	0.05
Diameter Ratio, κ	0.5
Relative Eccentricity, e	0.9

Solid Bed Height, H_{bed} (%)	30
Fluid Flow Rate, Q (m^3/s)	$5x10^{-5}$
Fluid Density, ρ (kg/m^3)	1000
Consistency Index, K ($Pa.s^n$)	$5x10^{-5}$
Fluid Behavior Index, n	1

Simulation results (Figure 4.6.) demonstrated that with increasing the number of grids, the pressure gradient tends to stabilize after reaching a mesh size of 2.2M elements. Increasing the number of mesh elements helps provide better resolution and accuracy. This sensitivity study shows the number of grids required for reliable and accurate CFD simulation of the annular geometry in consideration.

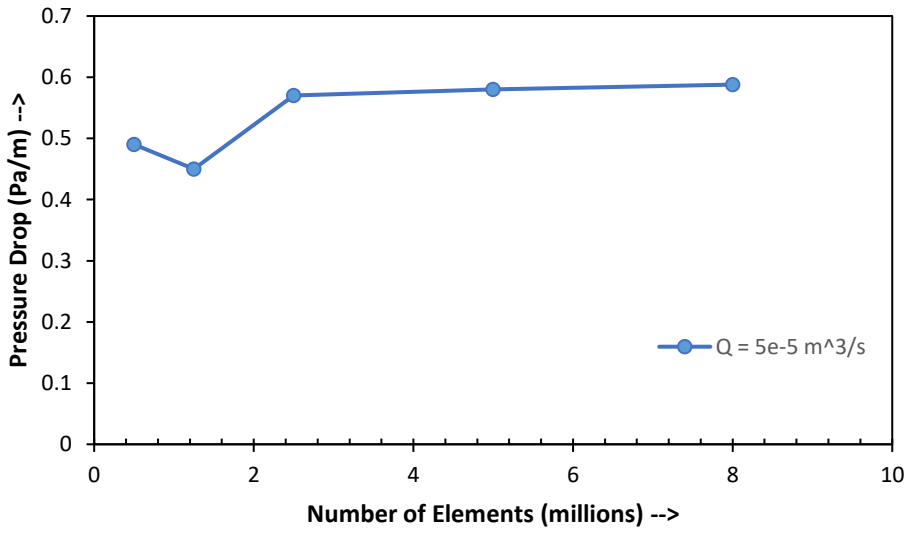

Figure 4.6. Grid independent study for various number of grids

4.5 Numerical Setup in Fluent Solver

Once the 3-D model is developed and the grid refinement is performed, the next step is to implement the necessary boundary conditions in the CFD model. This research aims to build a 3-D model taking into account the effect of cutting bed height. In order to study these effects, several numerical simulations need to be performed varying the cutting bed thickness and annular diameter ratio. Hence, one of the first things before performing CFD fluid flow simulation is to select the appropriate solver type. In this research, a steady-state pressure-based solver is selected as the fluid is incompressible in nature. Also, the final results obtained through simulation need to be independent of all initial conditions; thus, the simulation needs to be performed for steady-state conditions.

There is no detailed step by step procedure to select the appropriate turbulent flow model used to simulate flow in a partially blocked annulus. As a result, the standard k-ε model is utilized. Due to the requirement of relatively reduced computational resources, the k-ε model is one of the most commonly used models to perform the numerical simulations of turbulent flows. Adding to it, the Enhanced Wall Treatment and Pressure Gradient Effect options are selected to provide a more refined result at wall boundaries.

Appropriate boundary conditions along with material properties and operating conditions are implemented in the solver. The ANSYS Fluent solver uses the time-based iterations to perform simulation for the defined flow condition. The numerical simulations are performed for turbulent flow conditions using the Semi-Implicit Pressure Linked Equation (SIMPLE) pressure velocity scheme. The SIMPLE scheme (algorithm) is a preferred method in providing solutions for incompressible flow problems. Also, second-order discretization is selected for Pressure,

Momentum, Turbulent Kinetic Energy and Turbulent Dissipation Rate to obtain an accurate and consistent solution.

The convergence assessment parameter for the continuity equation is kept at $1x10^{-4}$ and the convergence criteria for momentum, k and epsilon equations are set at $1x10^{-7}$. After the convergence criteria are meet the simulations are concluded and results are post-processed within the Fluent solver. Visual examination of the contour diagrams and the various plots help identify numerical instability issues and a better understanding of the flow dynamics.

4.6 Post-Processing

After the numerical simulations are carried out and desired results are obtained, it is important to display results in a meaningful manner to provide reasonable explanations and interpretations for various observations. Contour diagrams are easier to extract from the solver using the post-processing tool. But plots like the velocity profile and shear stress distribution require a dimensionless coordinate system (Fig. 4.7) to display and interpret their results. The dimensionless parameters (X_L and Y_V) used to define eccentric annulus geometry. The dimensionless lateral distance is expressed as:

$$X_L = \frac{X - W_i}{W_{bed}} \tag{4.1}$$

And, dimensionless vertical distance defined as:

$$Y_V = \frac{Y}{R_o} \tag{4.2}$$

where W_i is inner pipe width, W_{bed} is the bed width, $X_L = 0$ means the inner pipe wall boundary, and $X_L = 1$ means the outer wall boundary.

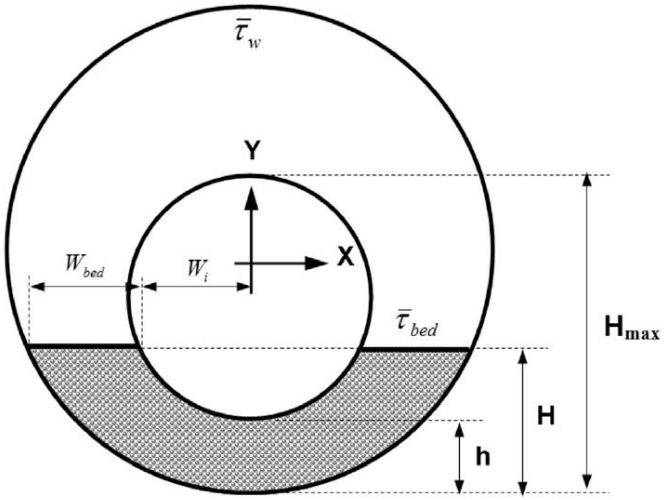

Figure 4.7. Eccentric annulus with x-y coordinate system (Rojas et al., 2017)

Chapter 5

Results and Discussion

In this chapter, the effects of diameter ratio, fluid properties and blockage height on pressure loss and wall stress are observed over the generated 3-D model. Results are obtained through post-processing of data, which include the velocity contours, velocity profiles, and shear stress distributions varying the cutting blockage height, fluid properties, and diameter ratio, thereby demonstrating their effects on pressure loss. The results are compared with predictions of existing models. Also, CFD simulations are compared with existing experimental measurements.

5.1 Verification of Simulation Results

A comparison is performed between CFD simulation results and experimental data. The experimentally measured pressure losses were obtained from the literature (Adari, 1999) for different bed heights, fluid properties and flow rates in an eccentric annulus. The CFD simulations were performed to reproduce measured pressure loss for the same flow geometry (bed heights, eccentricity, and diameter ratio), fluid properties (Table 5.1), and flow rate. The CFD simulation results (Figures 5.1 to 5.4) show good agreement with experimental data, with an average discrepancy of ±22%, indicating that the approach adopted within ANSYS Fluent solver to simulate the flow is acceptable (Table 5.2).

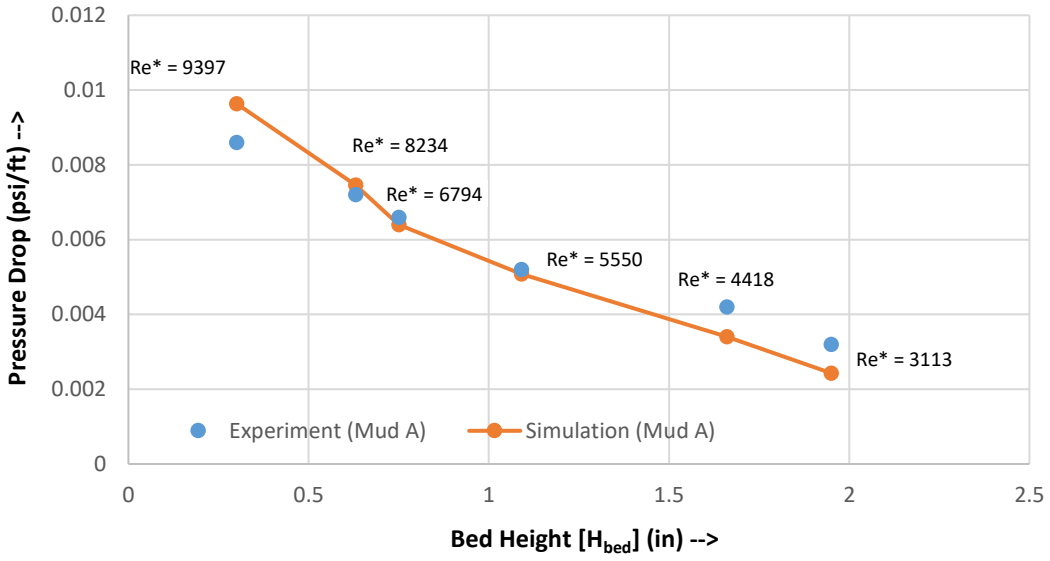

Figure 5.1. A comparison of CFD prediction with experimental measurement for Mud A

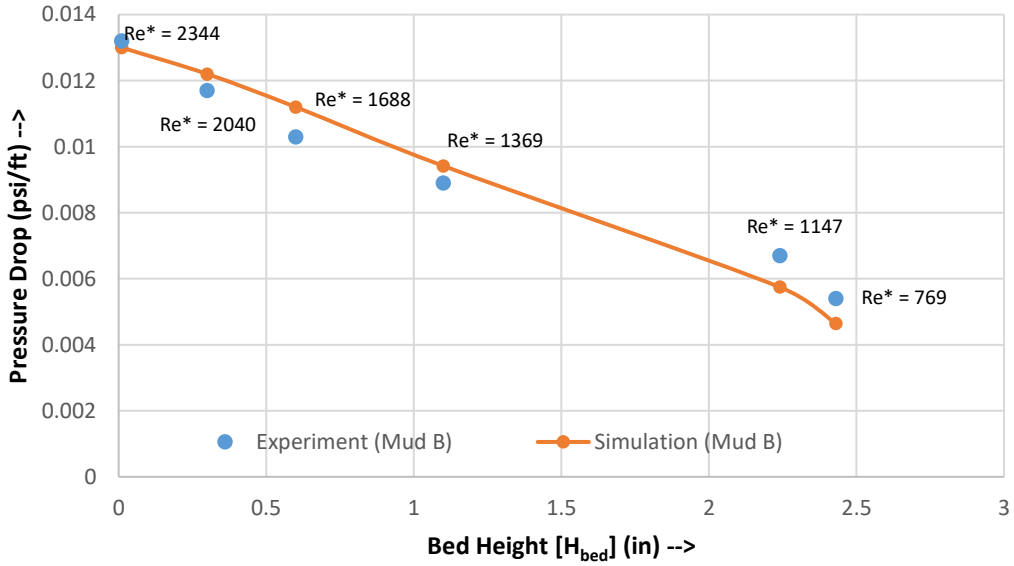

Figure 5.2. A comparison of CFD prediction with experimental measurement for Mud B

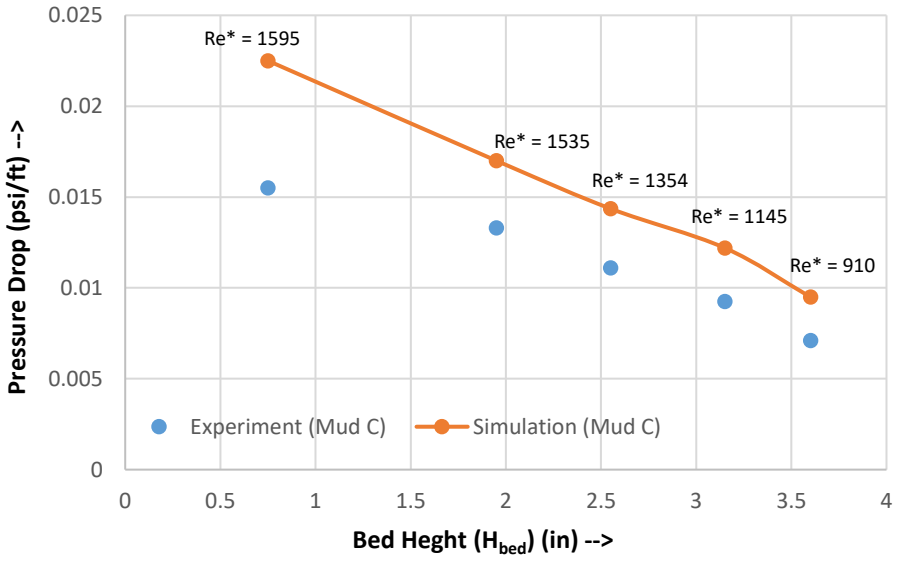

Figure 5.3. A comparison of CFD prediction with experimental measurement for Mud C

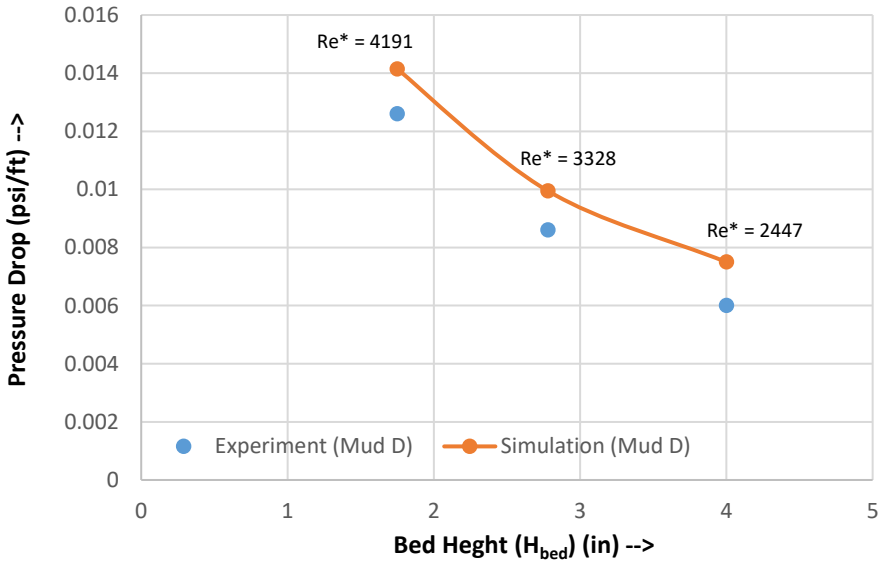

Figure 5.4. A comparison of CFD prediction with experimental measurement for Mud D

The experiment comprised of four Water Based Mud (WBM) namely Mud A, Mud B, Mud C and Mud D with their corresponding fluid properties, shown in Table 5.1. In the experiments,

the flow rates are varied from 150 to 400 gal/min for the blockage height's ranging between 0.01 to 4.00 in, i.e., from a nearly unblocked annular region to a fully buried inner pipe condition. Also, the corresponding Reynolds number is determined using Eq. (3.15), which helps distinguish the flow regime. The annular geometry was 8.0 in outer casing diameter and 4.5 in inner drill pipe diameter with an eccentricity of one.

A comparison is made between the experimental and simulation results, based on the pressure gradient for all variations, and they are listed in Table 5.2. The trends observed are displayed in the form of plots shown in Figure 5.1 to 5.4. All the results are found to be in agreement with the laminar region pressure points having a discrepancy of around 30%, while the turbulent points are fairly accurate with discrepancy of about 17%.

Table 5.1. Fluid Properties used in Experimental Analysis

Fluid Type	Fluid Behavior (n)	Consistency Index K (kg/ms)
Mud A	0.65	0.061
Mud B	0.52	0.408
Mud C	0.56	0.566
Mud D	0.69	0.140

Table 5.2. Pressure Gradient Comparison for CFD and Experimental Work

Fluid Type	Bed Height H_{bed} (in)	Volumetric Flow Rate Q (gal/min)	Reynolds Number (Re^*)	Experiment dP/dL (psi/ft)	Simulation dP/dL (psi/ft)
Mud A	1.95	150	3113	0.0032	0.00243
	1.66	200	4418	0.0042	0.0034
	1.09	250	5550	0.0052	0.00508
	0.75	300	6794	0.0066	0.0064
	0.63	350	8234	0.0072	0.00746
	0.30	400	9397	0.0086	0.0096
Mud B	0.30	350	2040	0.0117	0.0122
	0.01	400	2324	0.0132	0.013

Mud D	4.00	200	2447	0.006	0.0075
	2.78	300	3328	0.0086	0.00995
	1.75	400	4191	0.0126	0.01414

A slightly higher error is observed for a few bed heights (Figure 5.1 to 5.4). This could be due to the meshing problem. The mesh system-generated might not able to capture the velocity distribution in the stagnant zone of the annulus. As a result, the impact of cutting beds on pressure loss is not accurately reflected as a thin bed is formed in the narrow annular gap. Also, discrepancies are higher at low Reynolds numbers. This could be related to the flow regime (Figure 5.3). The Reynolds number determined from the flow parameters and fluid properties can only be considered as approximate indicative of the flow regime. Hence, some of the low Reynolds number flow measurements were possibly obtained under the laminar and/or transition flows.

5.2 Annular Pressure Loss

Numerous simulations have been carried to predict the annular pressure loss for a solid bed height ranging from 0% to 100%, which means from an unblocked annulus to a partially blocked annulus (fully buried inner pipe). For an eccentric annulus ($e = 0.9$), the effect of cutting buildup is observed. Maintaining a constant flow rate and turbulent flow condition for all the cases, observations are made in regard to the annular pressure gradient (dp/dz). Figures 5.5, 5.6 and 5.7 show graphs of annular pressure loss as a function of bed height. An exponential increase in pressure loss is observed with bed height and diameter ratio. This is mainly due to the reduction in flow area as the bed height and diameter ratio increase (Fig. 5.8). The reduction in flow area significantly increases the mean fluid velocity (Fig. 5.9) resulting in increased pressure loss.

Another important observation is that the hydraulic resistance diminishes with decreasing the value of 'n' (improving shear-thinning tendency of the fluid). From Figures 5.5 to 5.7, it can be interpreted that the annular pressure loss decreases with improving the shear-thinning behavior of the fluid. Furthermore, there is a substantial decrease in the frictional pressure loss, with a reduction in diameter ratio (from 0.75 to 0.25). The reason for this is an increase in the annular area, i.e., allowing the fluid to flow through with reduced restriction. As the flow area increases, the annular pressure loss decreases. Moreover, as the diameter ratio increases (Fig. 5.7), the pressure loss becomes more sensitive to the change in bed hight. As a result, the pressure loss increases sharply with bed height.

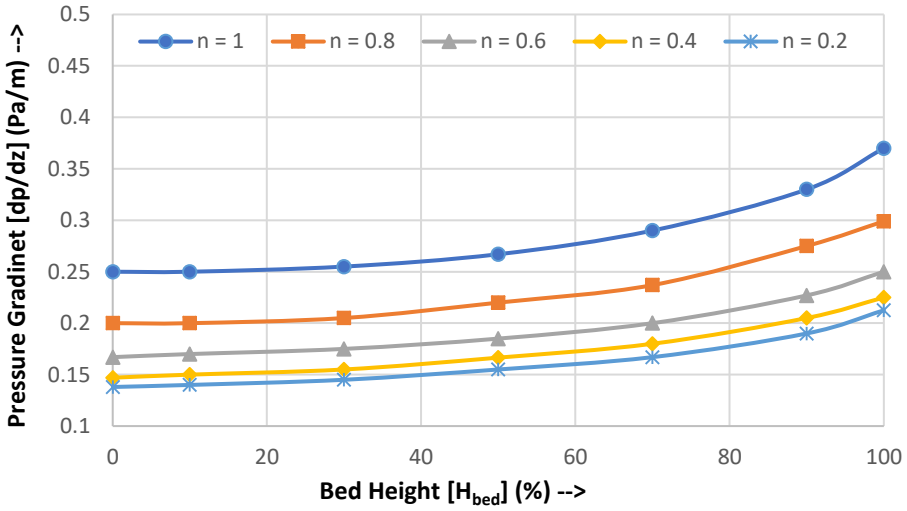

Figure 5.5. Pressure loss vs bed height for conditions [κ = 0.25, e = 0.9 and Q = 5x10^{-5} m^3/s]

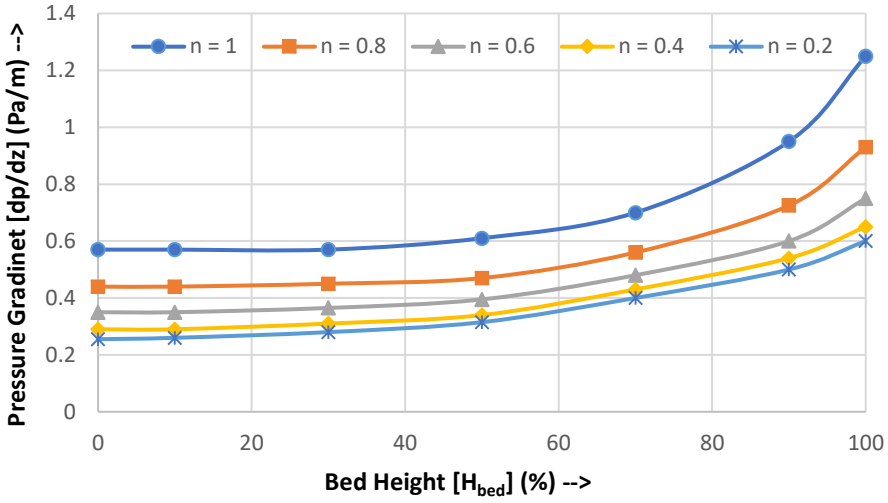

Figure 5.6. Pressure loss vs bed height for conditions [κ = 0.50, e = 0.9 and Q = 5x10^{-5} m^3/s]

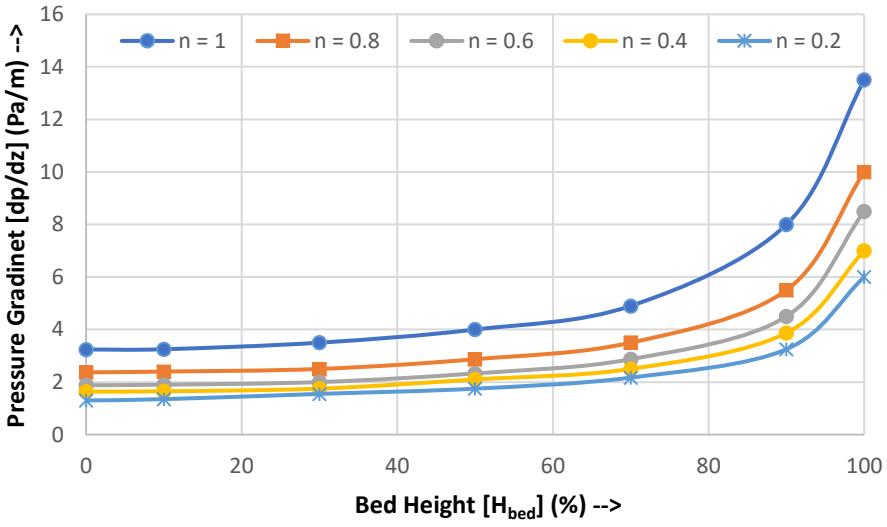

Figure 5.7. Pressure loss vs bed height for conditions [κ = 0.75, e = 0.9 and Q = 5x10^{-5} m^3/s]

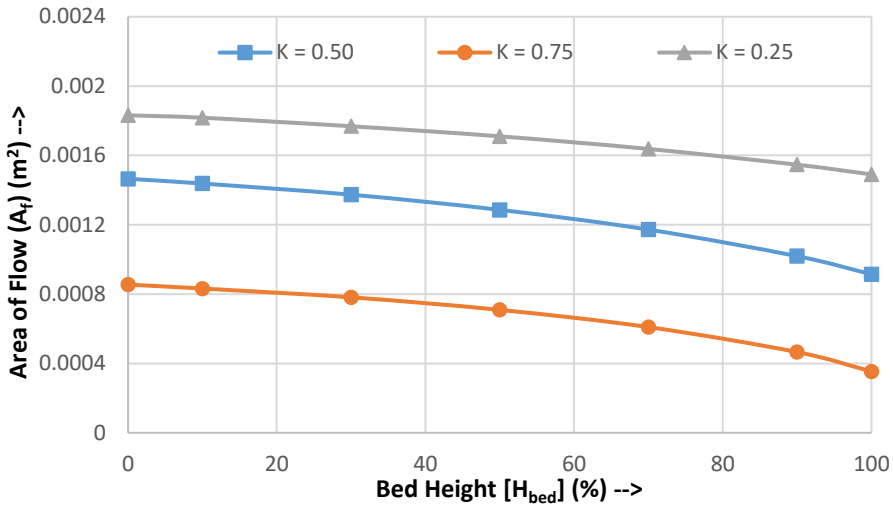

Figure 5.8. Area of flow vs bed height for conditions [e = 0.9 and Q = 5x10^{-5} m^3/s]

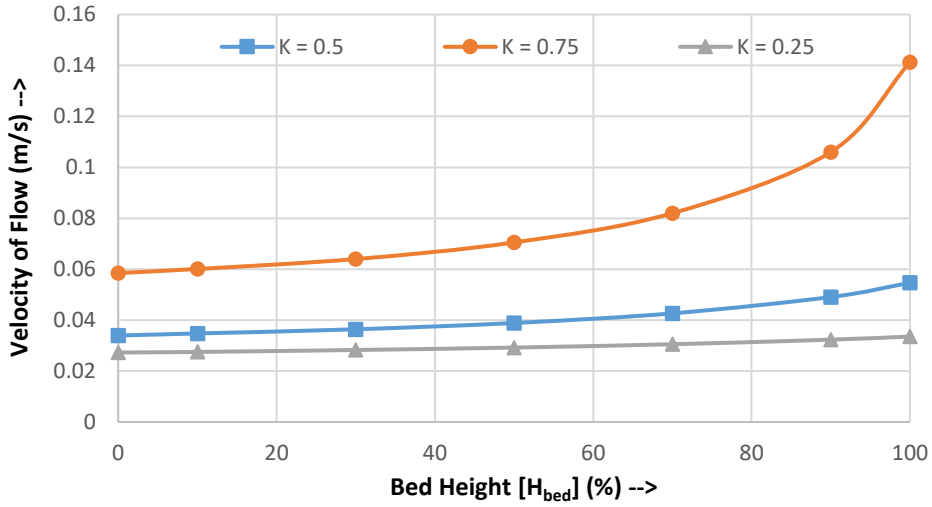

Figure 5.9. Annular flow velocity vs bed height [e = 0.9 and Q = 5x10^{-5} m^3/s]

5.3 Axial Velocity Distribution

This section gives an insight into the axial velocity distribution. Figure 5.10 shows axial fluid velocity along the central axis of the annulus. It can be deduced that with increasing the fluid

behavior index (n), the maximum fluid velocity slightly increased. With a reduction in fluid behavior index, a flatter velocity profile is observed. Overall, the impact fluid parameter 'n' on the velocity profile is minor under turbulent flow conditions. It is also noticed and is seen to affect the nature of the graph significantly.

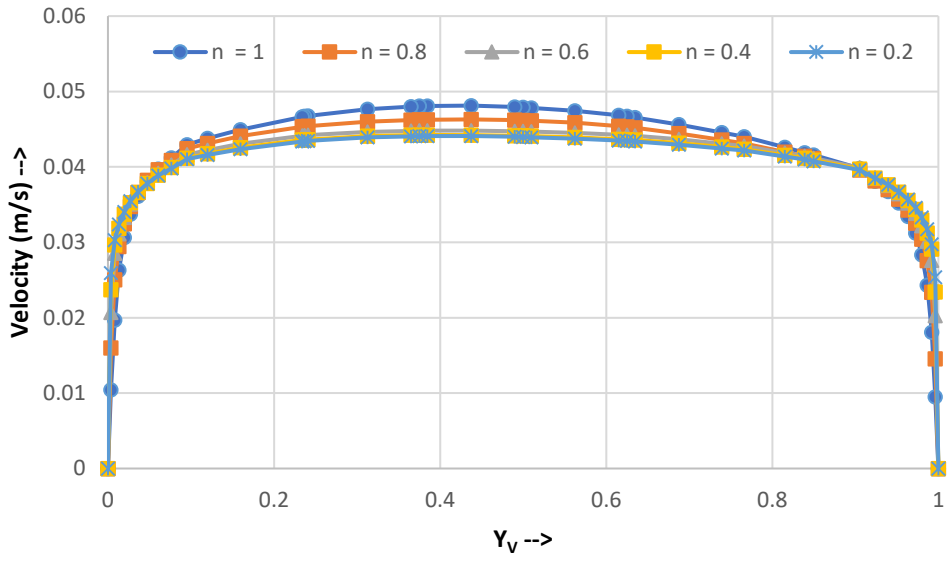

Figure 5.10. Velocity profile for conditions [H_{bed} = 50%, κ = 0.50, e = 0.9 and Q = 5x10^{-5} m^3/s]

Figures 5.11 and 5.12 display velocity contours observed at different diameter ratios and bed thicknesses. Regions with low fluid velocity (stagnant zones) are indicated by green color. These zones are found to be dominant in the lower regions of the annulus and more prominent when the bed height is low (Fig. 5.11 and 5.12). As the bed thickness increases, the stagnant zone reduces and eventually disappears when the bed height reaches the top of the inner pipe. Similar trends for both velocity plots and contour diagrams for all diameter ratios are displayed in the Appendix.

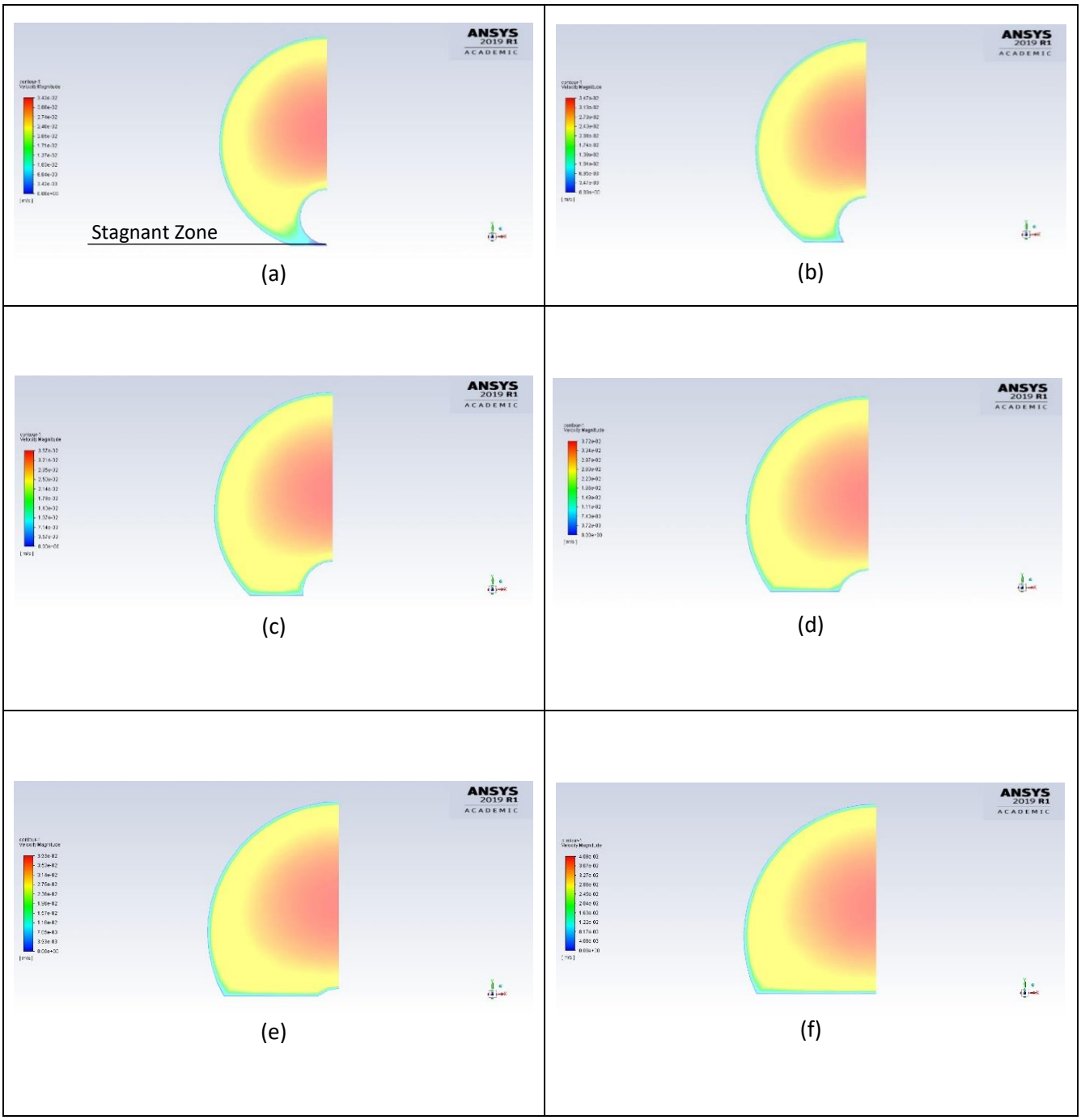

Figure 5.11. Velocity distributions in partially blocked annuli [n = 1, κ = 0.25, e = 0.9 and Q = 5x10^{-5} m^3/s]: (a) H_{bed} = 10%; (b) H_{bed} = 30%; (c) H_{bed} = 50%; (d) H_{bed} = 70%; (e) H_{bed} = 90%; and (f) H_{bed} = 100%

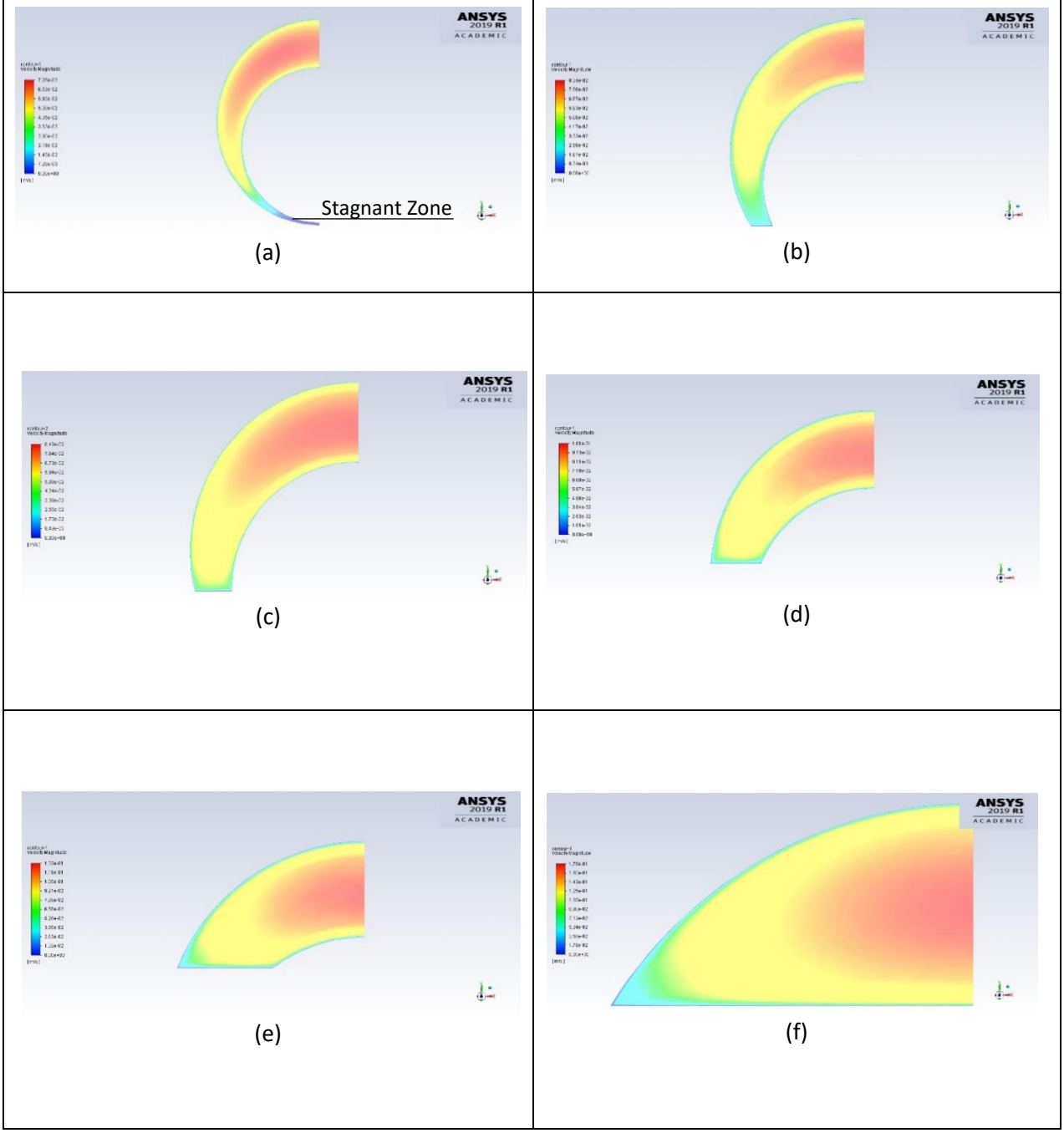

Figure 5.12. Velocity distributions in partially blocked annuli [n = 1, κ = 0.75, e = 0.9 and Q = 5x10^{-5} m^3/s]: (a) H_{bed} = 10%; (b) H_{bed} = 30%; (c) H_{bed} = 50%; (d) H_{bed} = 70%; (e) H_{bed} = 90%; and (f) H_{bed} = 100%

5.4 Shear Stress Distribution

5.4.1 Wall Shear Stress

For eccentric annulus, the wall shear stress is not uniform. The wall shear stresses vary significantly along the wetted perimeter resulting in a non-uniform distribution. Also, the presence of solids bed on the low-side of wellbore further complicates the shear stress distribution. Hence, the average wall shear stress ($\bar{\tau}_w$) is used to perform flow analysis. Figures from 5.13 to 5.15 display the average wall shear stress ($\bar{\tau}_w$) as a function of bed hieght for different values of fluid behavour index.

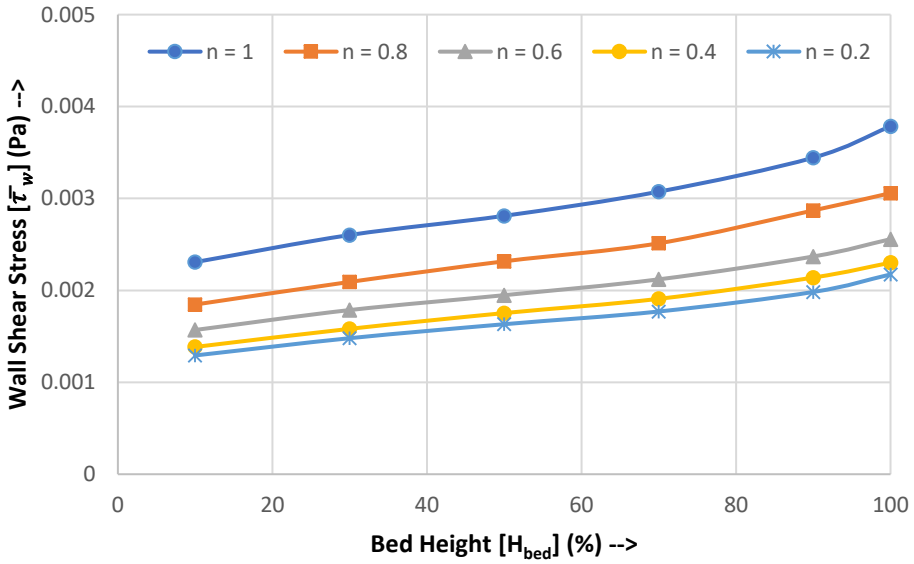

Figure 5.13. Wall shear stress vs bed height for conditions [κ = 0.25, e = 0.9 and Q = 5x10^{-5} m^3/s]

Looking at the plots, a few observations can be drawn in regard to the impact of blockage height on average wall shear stress. As the blockage height increases, the average wall shear stress in the wellbore also increases. This is expected because the flow rate is maintained constant as the blockage height increases. Consequently, the mean fluid velocity increases with blockage height

causing the wall shear stress to increase. The effect of fluid behavior index on the wall shear stress is significant. As anticipated, the wall shear stress shows a substantial reduction with the enhancement of shear-thinning characteristics of the fluid. Furthermore, the average wall shear stress follows the trend displayed by the pressure loss. It can be visually depicted that wall stress is proportional to the pressure gradient (dp/dz).

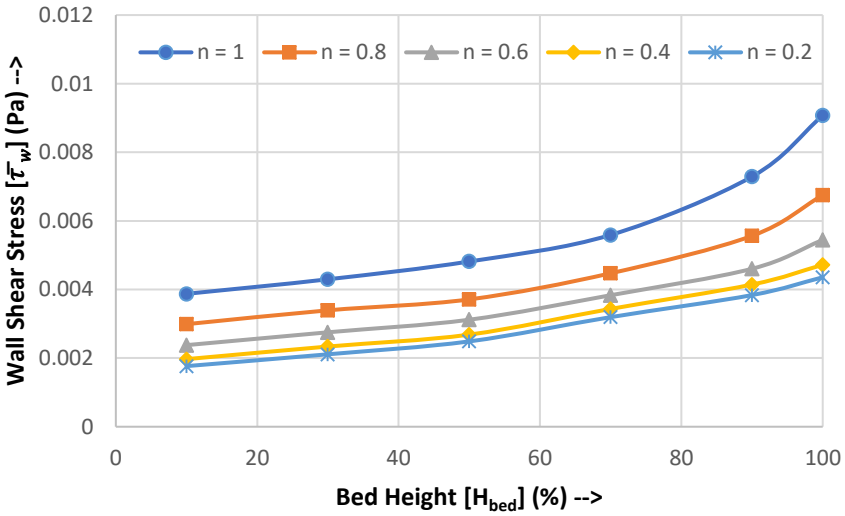

Figure 5.14. Wall shear stress vs bed height for conditions [κ = 0.50, e = 0.9 and Q = 5x10^{-5} m^3/s]

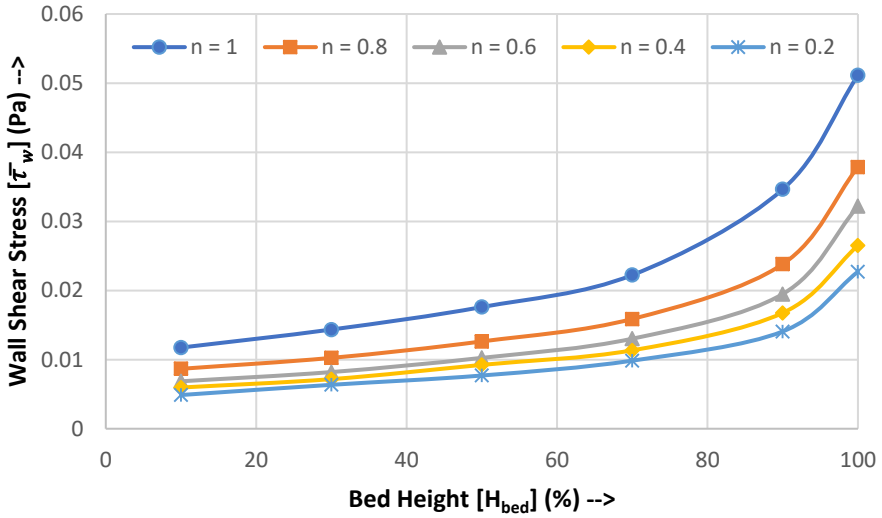

Figure 5.15. Wall shear stress vs bed height for conditions [κ = 0.75, e = 0.9 and Q = 5x10^{-5} m^3/s]

5.4.2 Bed Shear Stress

As illustrated in the previous section, the lower the fluid velocity, the lower is the bed shear stress. The same phenomenon can be observed over the area occupied by the solids cutting bed. Figures 5.16 and 5.17, show the bed shear stress distributions in a partially blocked annulus and an annulus with a fully buried inner pipe. Two distinct observations can be made. At low blockage height (Fig. 5.16), the bed shear stress generated at the outer wall boundary is considerably higher than the one created at the inner pipe boundary. And, the reverse happens for the case of high blockage height (Fig. 5.17). The bed shear stress at the inner pipe is substantially higher than the bed shear stress at the outer pipe. In the case of intermediate blockage (Fig. 5.18), the bed shear stress at the inner and outer pipe walls are comparable. The maximum bed shear stress occurs close to the middle of the bed.

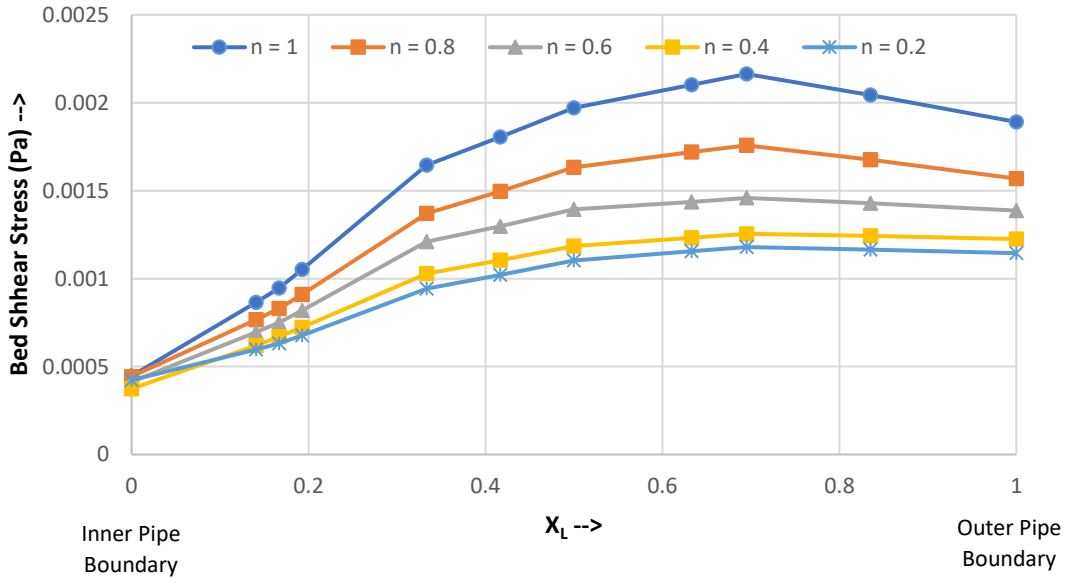

Figure 5.16. Bed shear stress vs lateral distance for H_{bed} = 30% [κ = 0.25, e = 0.9 and Q = 5x10^{-5} m^3/s]

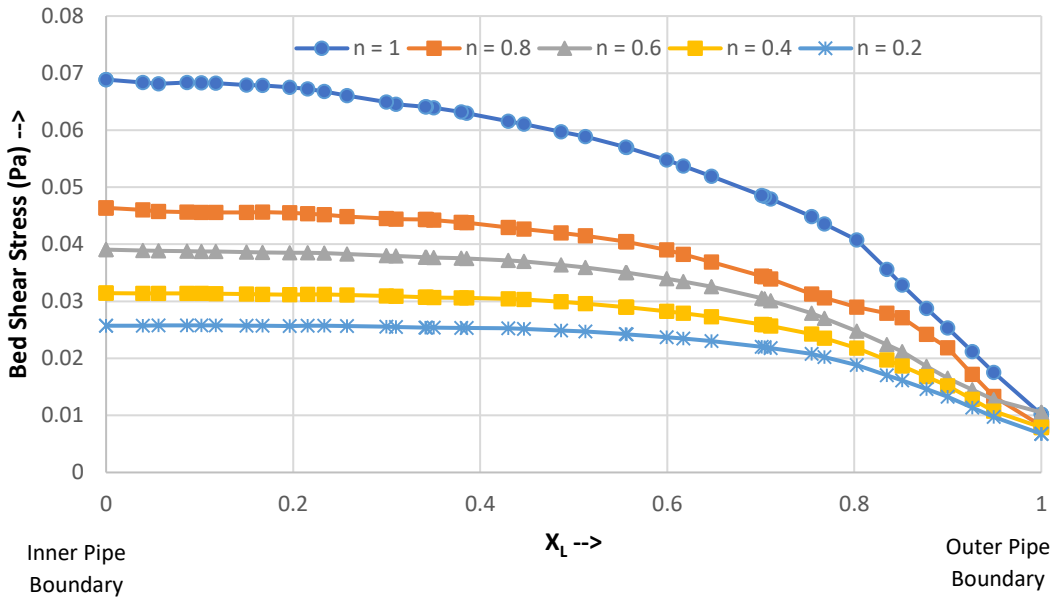

Figure 5.17. Bed shear stress vs lateral distance for H_{bed} = 100 % and for conditions [κ = 0.75, e = 0.9 and Q = 5x10^{-5} m^3/s]

Furthermore, the impact of shear-thinning behavior on bed shear stress is significant. The bed shear stress considerably varies with lateral distance when the fluid is Newtonian or weakly shear-thinning. Also, the improvement of the shear-thinning behavior, the bed shear stress diminishes. Similar observations are made for other scenarios of different diameter ratios.

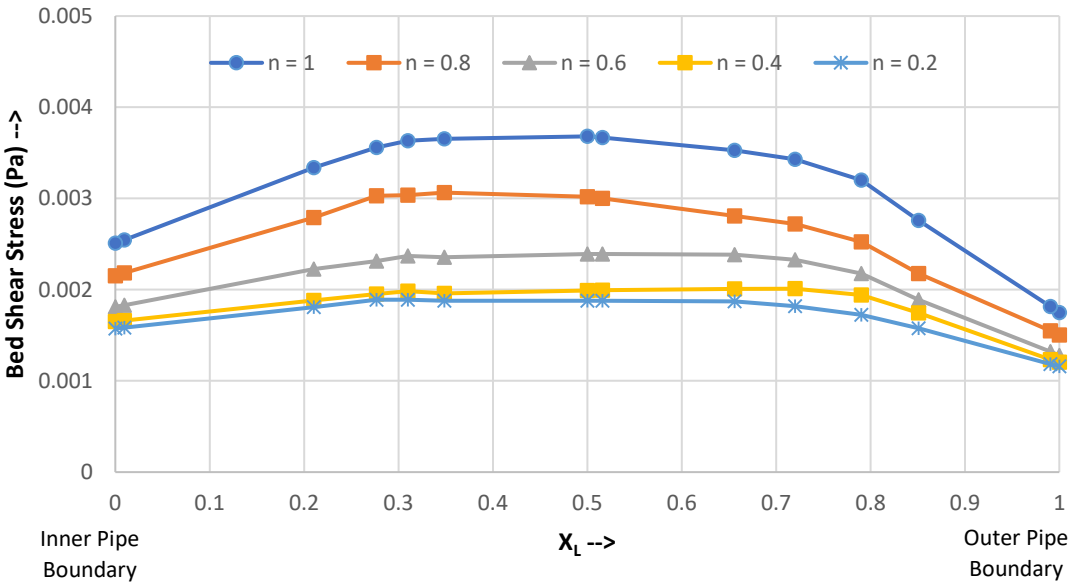

Figure 5.18. Bed shear stress vs lateral distance for H_{bed} = 50 % and for conditions [κ = 0.25, e = 0.9 and Q = 5x10^{-5} m^3/s]

Figures 5.19 to 5.21 show the average bed shear stress as a function of bed height for different diameter ratios and fluid properties (fluid behavior index). At a constant flow rate, as the diameter ratio increases, the bed shear stress is also increased. This is because of a reduction in flow area, resulting in an increase in fluid velocity. Thereby indicating an effect that as the bed height decreases, a reduction in bed shear stress is evident. The reduction in bed shear stress limits hole cleaning in horizontal and inclined wells.

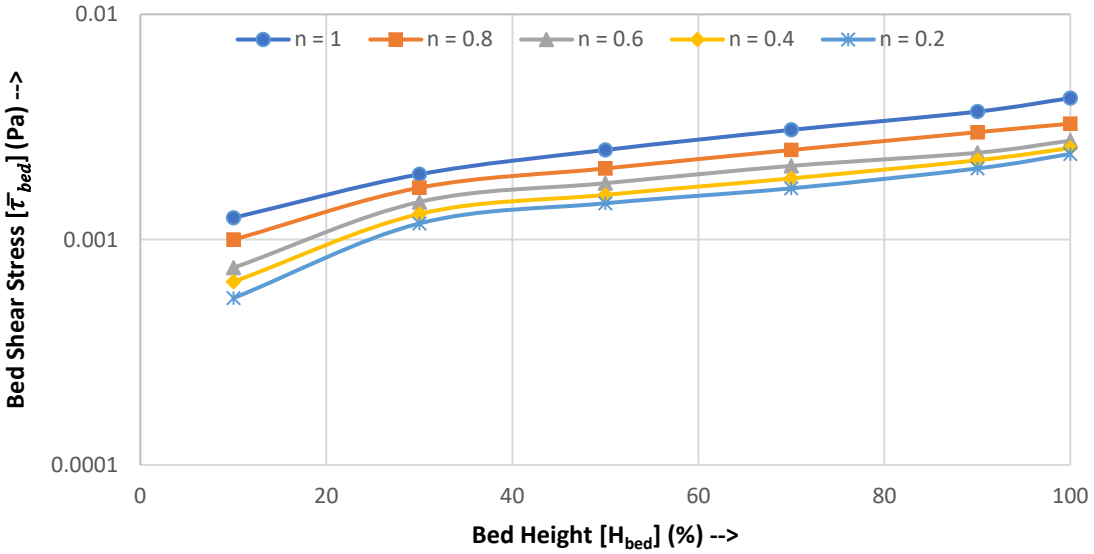

Figure 5.19. Bed shear stress vs bed height for conditions [κ = 0.25, e = 0.9 and Q = 5x10^{-5} m^3/s]

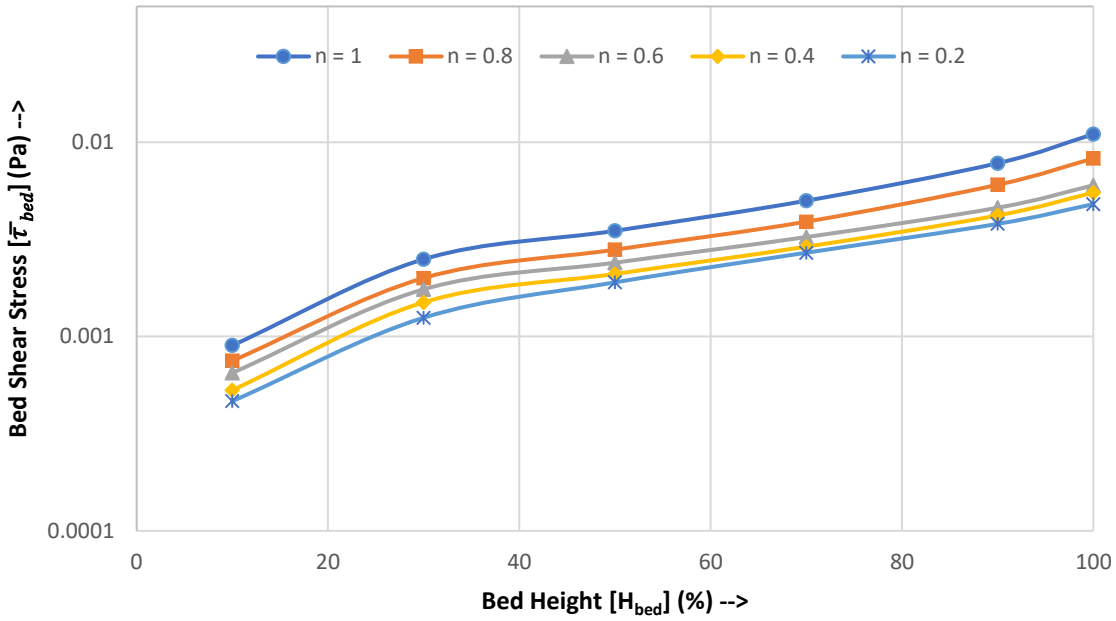

Figure 5.20. Bed shear stress vs bed height for conditions [κ = 0.50, e = 0.9 and Q = 5x10^{-5} m^3/s]

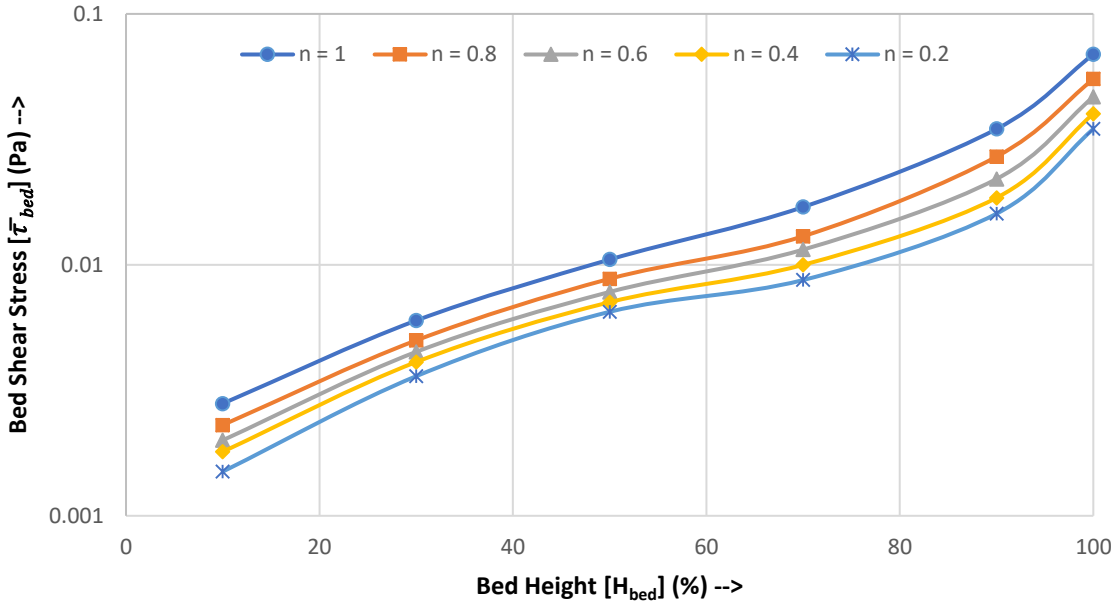

Figure 5.21. Bed shear stress vs bed height for conditions [κ = 0.75, e = 0.9 and Q = 5x10^{-5} m^3/s]

5.4.3 Dimensionless Bed Shear Stress

As defined in earlier chapters, the dimensionless bed shear stress (π_{bed}) is the ratio of bed to wall shear stress. The ratio is a dimensionless parameter that ranges between 0 to 1. Figures 5.22, to 5.24 display the relationship between diameter ratio and dimensionless bed shear stress. It is important to note the impact of fluid behavior index (n) on dimensionless bed shear stress (π_{bed}). As the index increases, the dimensionless bed shear stress increases. The effect of fluid behavior index on dimensionless bed shear stress is found to diminish at high bed thickness (close to 100% bed height). Thus, indicating that the average wall shear stress increases with blockage height and eventually aligns with the overall wall shear stress ($\bar{\tau}_w$)

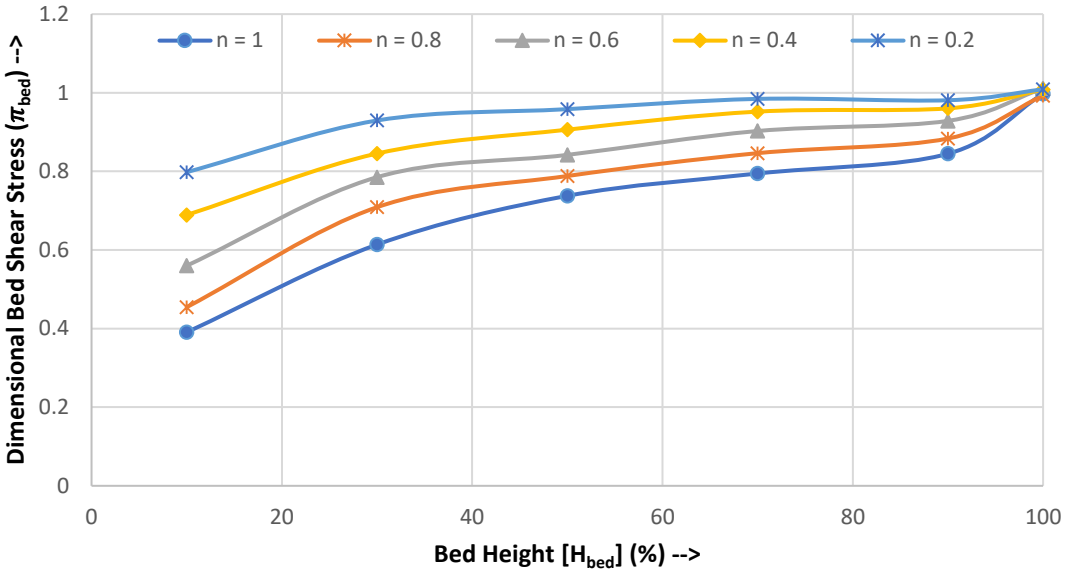

Figure 5.22. Dimensionless bed shear stress vs bed height for conditions [κ = 0.25, e = 0.9 and Q = 5x10^{-5} m^3/s]

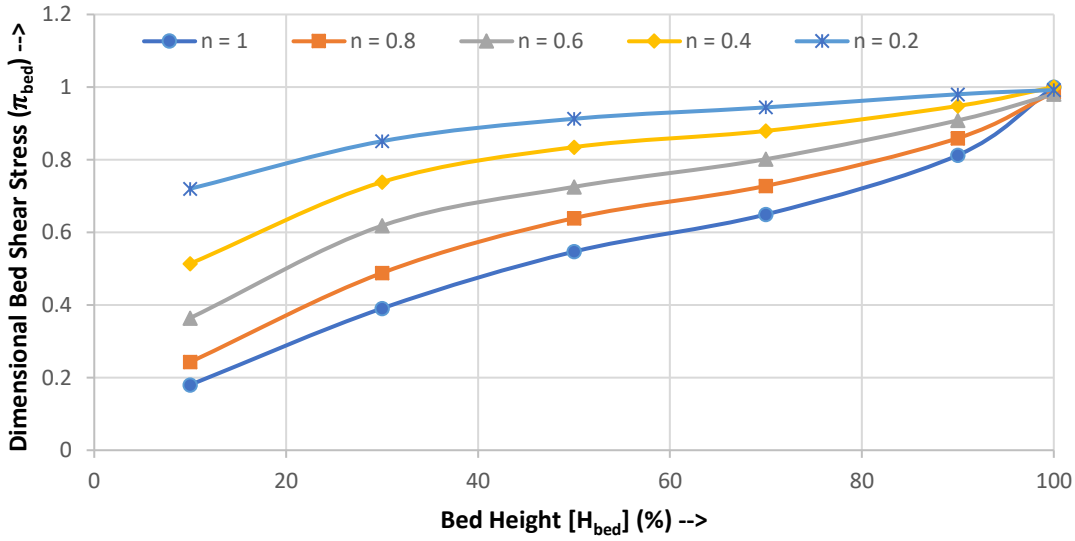

Figure 5.23. Dimensionless bed shear stress vs bed height for conditions [κ = 0.50, e = 0.9 and Q = 5x10^{-5} m^3/s]

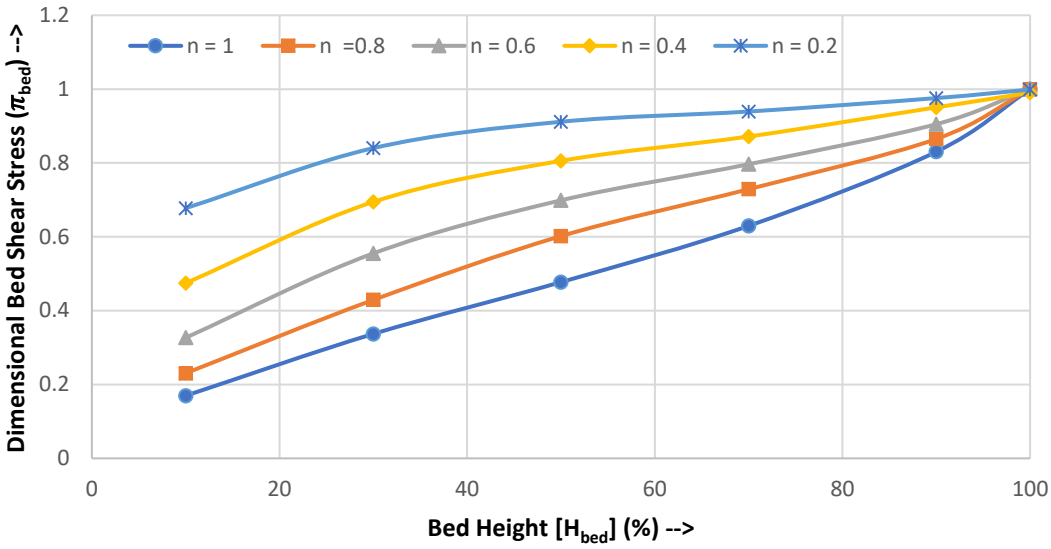

Figure 5.24. Dimensionless bed shear stress vs bed height for conditions [κ = 0.75, e = 0.9 and Q = 5x10^{-5} m^3/s]

5.5 Flow Rate Variation

The flow rate is varied to examine its impact on other flow parameters such as average wall shear stress, average bed shear stress, and dimensionless bed shear stress. Two flow rates (1x10^{-4} and 1x10^{-5} m^3/s) are considered in the analysis. The diameter ratio is maintained at 0.75.

Impact on Wall Shear Stress

As expected, the average wall shear stress increases with the flow rate (Figs. 5.25 and 5.26). Also, at a low flow rate (1x10^{-5} m^3/s), the wall shear stress shows a slight reduction with blockage for highly shear-thinning fluid. This is not observed in the case of a high flow rate (1x10^{-4} m^3/s). It is not clear if this observation is due to a numerical error or because of flow phenomena such as shear thinning and turbulence. As stated earlier, the general trend is an increase in the overall wall shear stress with cuttings accumulation (solid bed rise). The magnitude of wall shear stress is also

dependent on the mean velocity. A rise in the upper limit of pressure gradient is observed as the flow rate is increased leading to an increase in average wall shear stress ($\bar{\tau}_w$)

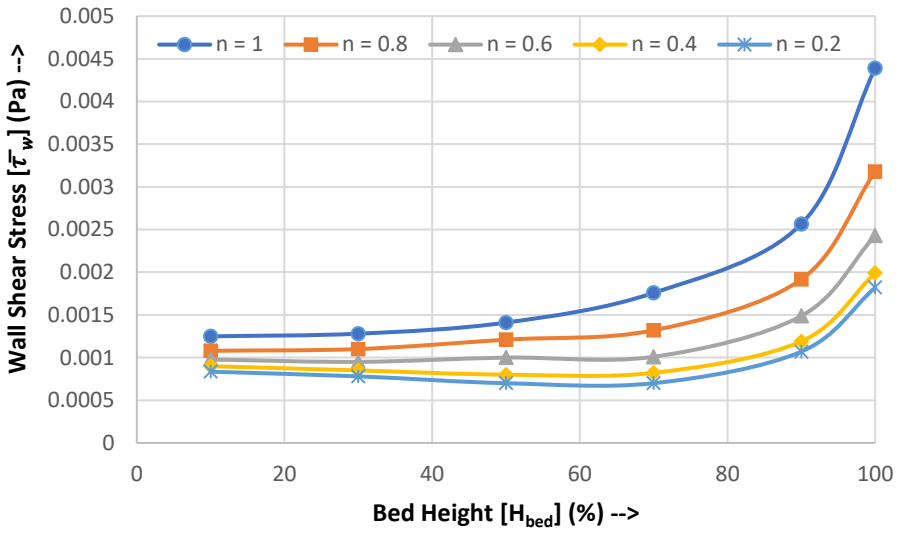

Figure 5.25. Wall shear stress vs bed height for conditions [κ = 0.75, e = 0.9 and Q = 1x10^{-5} m^3/s]

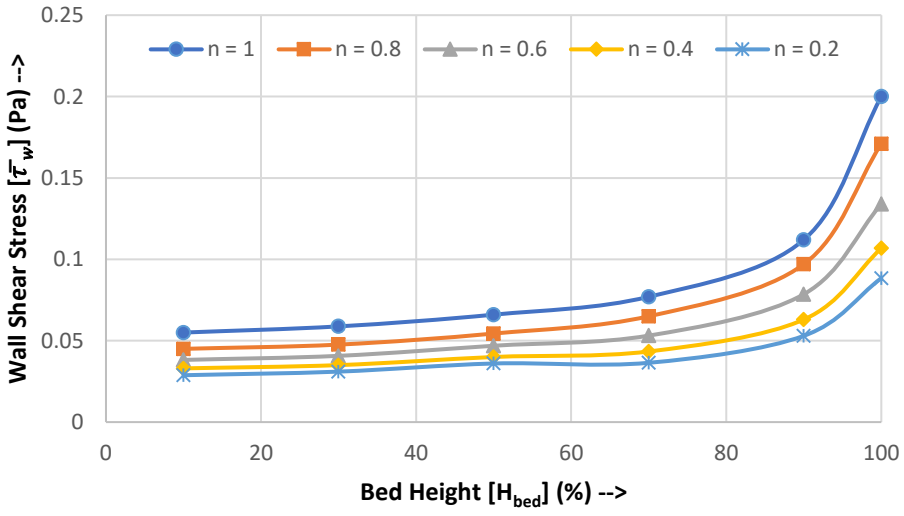

Figure 5.26. Wall shear stress vs bed height for conditions [κ = 0.75, e = 0.9 and Q = 1x10^{-4} m^3/s]

Impact on Bed Shear Stress

As mentioned in previous sections, the bed shear stress substantially increases with cutting bed height. In Figs. 5.27 and 5.28, the increase is evident as the nature of the graph has an upward trend indicating a positive effect. Likewise, as the flow velocity increases, the shear stress generated at the bed surface increases significantly. Moreover, the bed shear stress for higher flow rates has a higher upper limit; similarly, for a lower flow rate, it has a lower upper limit.

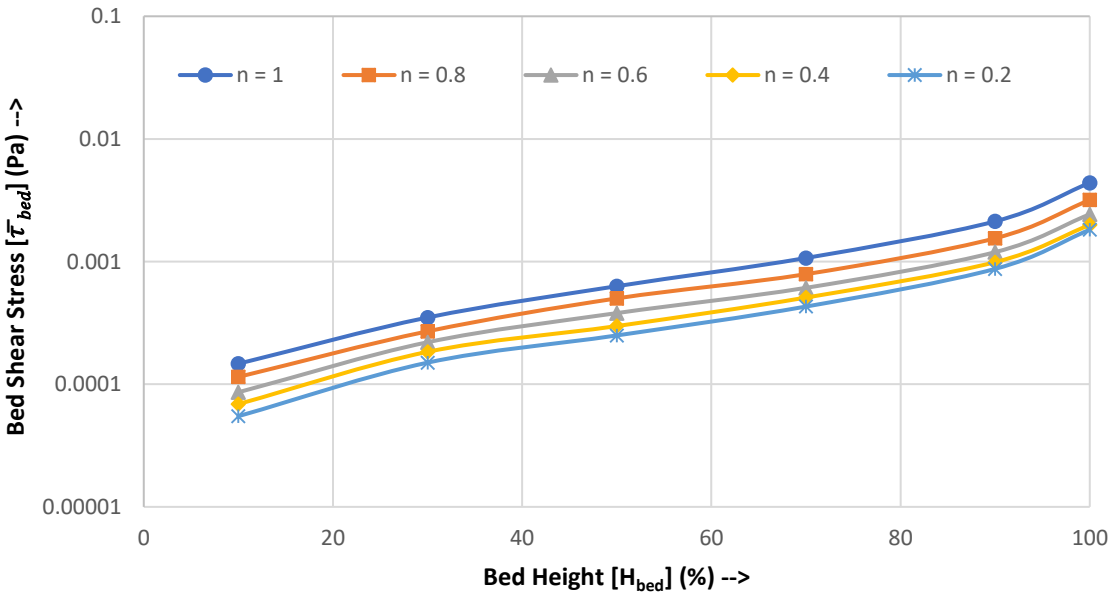

Figure 5.27. Bed shear Stress vs dimensionless bed height for conditions [κ = 0.75, e = 0.9 and Q = 1x10^{-5} m^3/s]

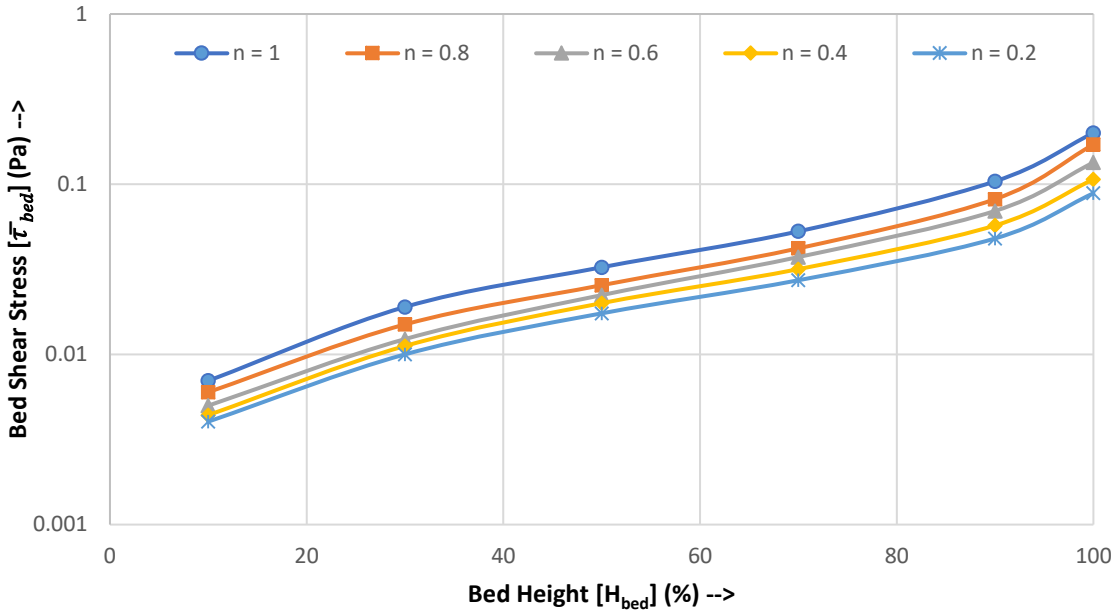

Figure 5.28. Bed shear stress vs bed height for conditions [κ = 0.75, e = 0.9 and Q = 1x10^{-4} m^3/s]

Impact on Dimensionless Bed Shear Stress

The effect of flow rate on the dimensionless bed shear stress is analyzed (Fig. 5.29) considering two flow rates (1x10^{-4} and 1x10^{-5} m^3/s). There is no noticeable change in dimensionless bed shear stress even after a ten-fold increase in flow rate, indicating that this parameter is independent of flow velocity and is only a function of geometric parameters such as diameter ratio and bed height, and fluid properties mainly the fluid behavior index. The diameter ratio considered for the analysis is 0.75. Similar results are obtained with other diameter ratios.

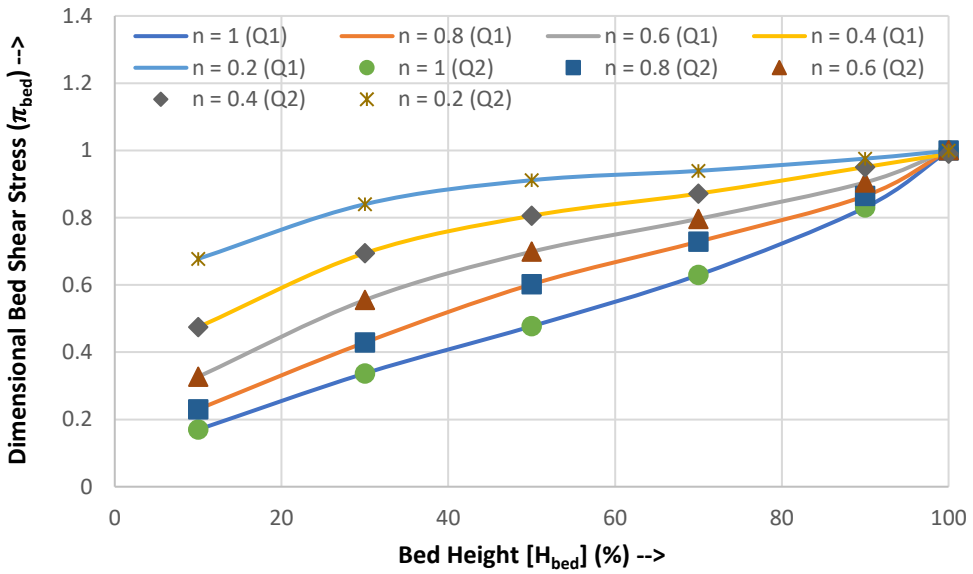

Figure 5.29. Dimensionless bed shear stress vs bed height for conditions [κ = 0.75, e = 0.9, $Q1$ = 1x10^{-5} m^3/s and $Q2$ = 1x10^{-4} m^3/s]

5.6 Consistency Index Variation

A sensitivity analysis is conducted by varying the fluid consistency index (K). The consistency index is varied while keeping the Reynolds number high to ensure the turbulent flow conditions. The behavior of the dimensionless bed shear stress is studied and thus, the nature of the graph is found to be independent of the fluid consistency index.

Furthermore, a non-linear regression method is utilized to present the dimensionless bed height as a function of flow behavior index, diameter ratio, and dimensionless bed height. The CFD simulation data obtained throughout this study is utilized in developing an empirical correlation for dimensionless bed shear stress (Π_{bed}). The correlation is expressed as:

$$\Pi_{bed} = \quad \hat{A}H_{bed}^{4.5} + \hat{B}H_{bed}^{2.5} + \hat{C}H_{bed}^{0.51} + \hat{D}n\kappa^{0.51} + \hat{E}(nH_{bed})^{1.4} + \hat{F}n + \hat{G} \qquad (5.1)$$

where $\hat{A}, \hat{B}, \hat{C}, \hat{D}, \hat{E}, \hat{F}$ and $\hat{G}$ are coefficients and have the following values: $\hat{A}$ = 0.492985, $\hat{B}$ = -0.790858, $\hat{C}$ = 0.859049, $\hat{D}$ = -0.5004261, $\hat{E}$ = 0.487752, $\hat{F}$ = - 0.285120, $\hat{G}$ = 0.555855. The correlation is valid for power-law fluid flowing through a partially blocked eccentric (90%) annulus under turbulent flow condition. The correlation is valid under the following ranges of parameters: diameter ratio ($0.25 \leq \kappa \leq 0.75$), power-law index ($0.2 \leq n \leq 1$), dimensionless bed height ($0.1 \leq H_{bed} \leq 1$), and Reynolds number ($Re^{*} > 2100$).

To validate the model, the consistency index is varied considering different power-law fluids. For all scenarios, the dimensionless bed height predicted by the regression model is in agreement with the simulation result (Fig. 5.30). A cross plot of the CFD data and model predictions are presented in Figure 5.31. The model is again found to be in agreement with CFD results showing mostly a discrepancy level of ±10%, which implies that the equation provides a reasonable prediction.

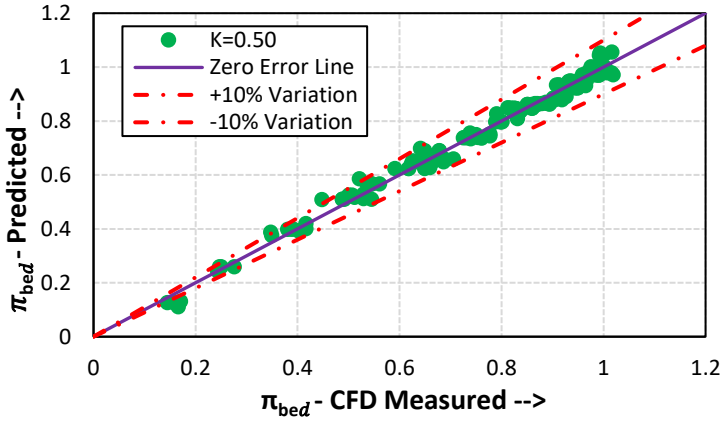

Figure 5.30. Dimensionless bed shear stress predicted vs dimensionless bed shear stress CFD for conditions [κ = 0.50, e = 0.9, K = 10^{-4} to 10^{-5} Pas^n and Q = 5x10^{-5} m^3/s]

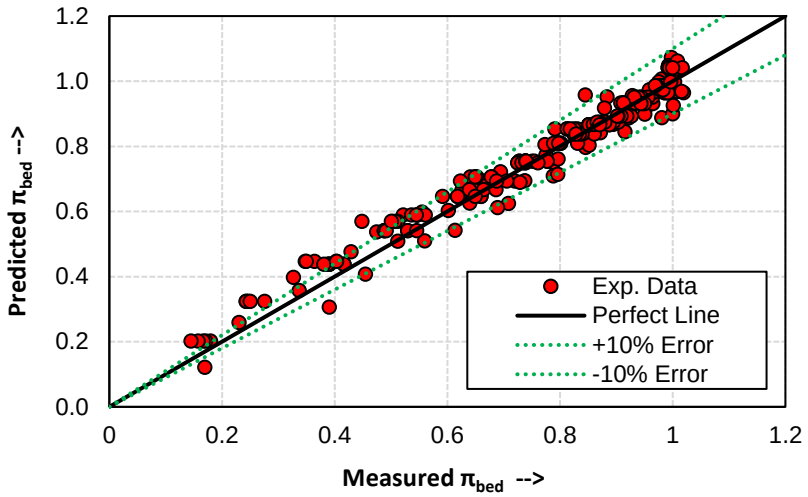

Figure 5.31. Dimensionless bed shear stress predicted vs dimensionless bed shear stress CFD for conditions [$0.25 \leq \kappa \leq 0.75$, e = 0.9 and Q = 5x10^{-5} m^3/s]

5.7 Comparison with Pre Existing Models

Pressure drop obtained from CFD simulation are compared (Fig. 5.32) with the predictions of an existing model developed by Kozicki et al., (1966). The friction factor correlation proposed by Kozicki et al., is used together with the correlations developed (Rojas et al., 2017) for the geometric parameters (a and b) and utilizing Eq. 3.22.

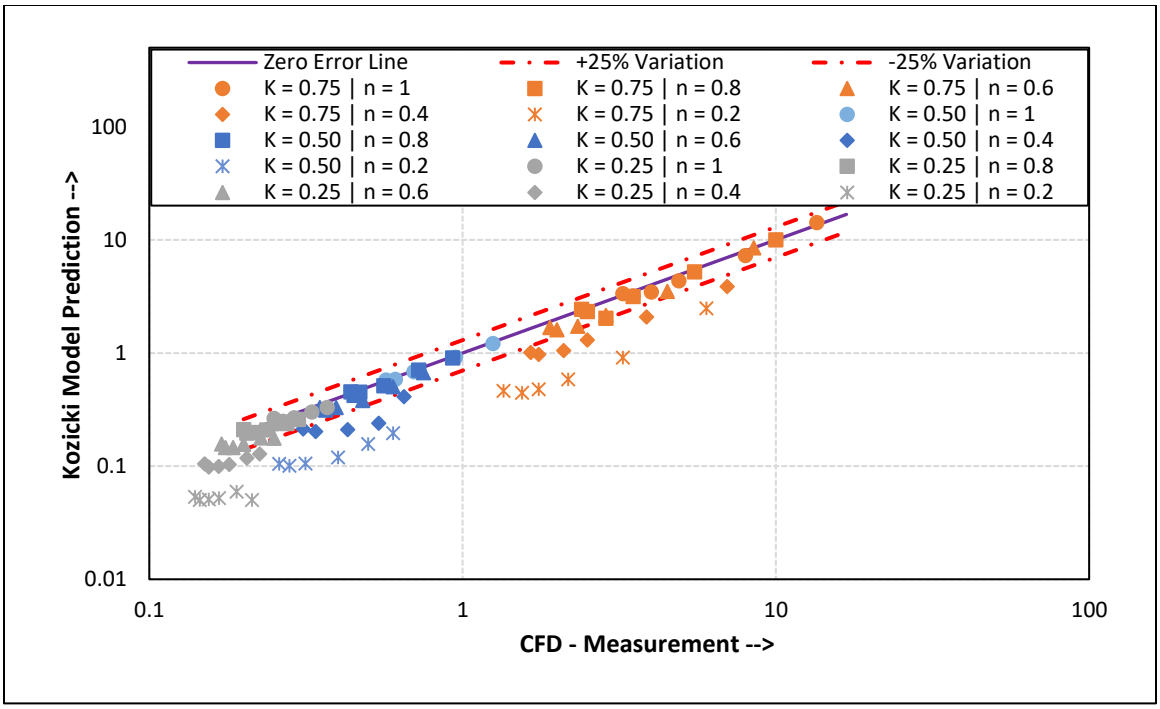

Figure 5.32. CFD measurements vs Kozicki's model predictions for conditions [$0.25 \leq \kappa \leq 0.75$, e = 0.9 and Q = 5x10^{-5} m^3/s]

From Figure 5.32 it can be interpreted that Kozicki's model works well and is in agreement with CFD results for Newtonian and shear-thinning fluids ($n > 0.4$). These results have been consistent irrespective of diameter change and have maximum discrepancies of about ±30%. However, on using the same model, for highly shear-thinning fluids ($n \leq 0.4$), the discrepancy between CFD results and Kozicki's predictions increases, implying the Kozicki's model fails for highly shear-thinning fluids ($n \leq 0.4$), i.e., it is unable to predict an accurate pressure drop for highly shear-thinning fluids.

Figure 5.33 shows that the hydraulic diameter model is able to reproduce CFD simulation results when the diameter ratio is between 0.25 and 0.75 and the fluid flow index is between 0.2

and 1.0. The CFD results are in agreement with the model with all the discrepancies laying within ±20%.

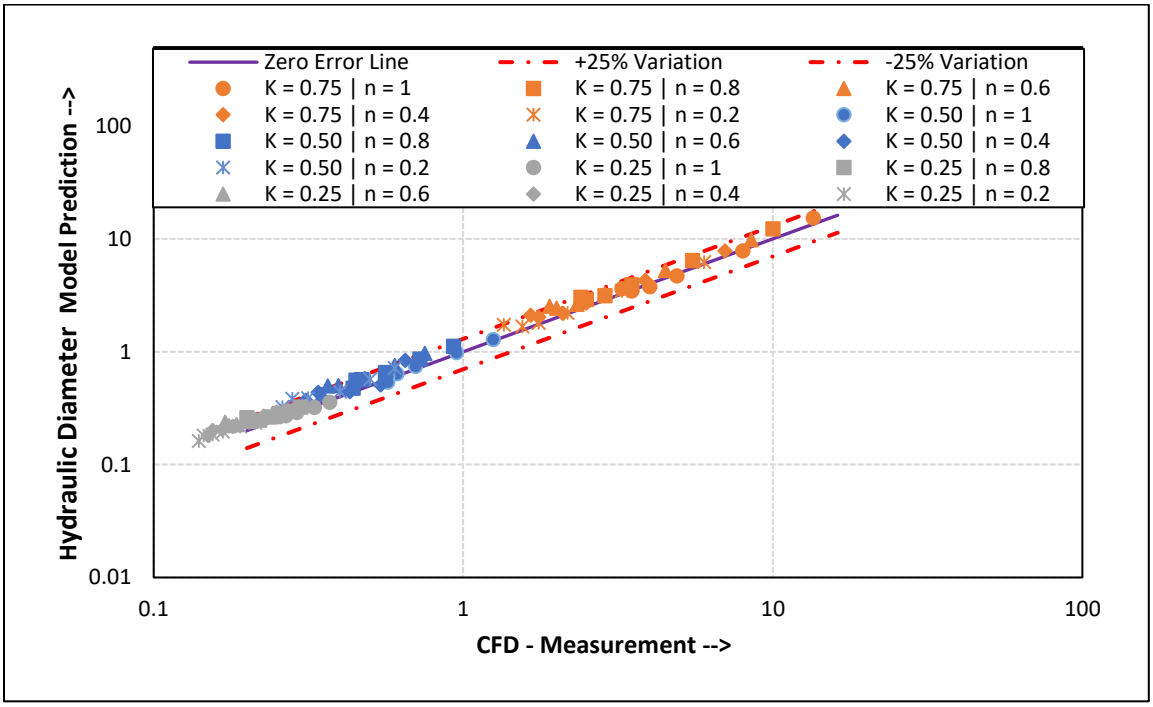

Figure 5.33. CFD measurements vs hydraulic diameter model predictions for conditions [$0.25 \leq \kappa \leq 0.75$, e = 0.9 and Q = 5x10^{-5} m^3/s]

Chapter 6

Conclusion and Future Works

6.1 Conclusions

Extensive CFD simulations have been conducted under turbulent flow conditions considering power-law fluid. The simulation study is conducted varying bed height, diameter ratio, and power-law flow behavior index. Based on the current research and investigation, the following conclusions can be drawn:

- Annular pressure loss and average bed shear stress are very important flow parameters that reduce with the shear-thinning behavior of the fluid.
- The pressure gradient is sensitive to bed height. Its effect is more prominent for a bed height (> 50%), this is mainly because of a reduction in stagnant zones.
- The dimensionless bed shear stress is independent of fluid consistency index and flow rate. It varies with diameter ratio, flow behavior index and bed thickness.
- The magnitude of bed shear stress is influenced by flow velocity, diameter ratio, bed thickness, and fluid properties.
- The CFD simulation provides a reasonable prediction of pressure loss, which is in agreement with experimental measurements.
- The CFD results and Kozicki's model predictions show good agreement when the fluid is slightly shear thinning ($0.6 \leq n \leq 1$). The model fails for highly shear-thinning fluids ($n < 0.4$).

- The CFD results and the hydraulic diameter model are in agreement as they are able to predict the pressure drop accurately for wide ranges of shear-thinning fluids (0.2 to 1.0) and diameter ratios (0.25 to 0.75).

6.2 Future Works

Using CFD, complex numerical simulations can be performed incorporating a number of flow variables to better understand flow in complex geometries such as partially blocked eccentric annulus.

The following recommendations are a few scenarios, one can consider as future works:

- Incorporating the effects of wall roughness under turbulent flow conditions in blocked eccentric annulus thereby studying its impact on frictional pressure loss.
- Examining the effect of inner pipe rotation and studying its impact on the frictional pressure gradient.
- Using other rheology models such as three-parameter models like Yield power-law fluids to investigate the flow in the eccentric annulus.
- Studying the impact of heat transfer from the formation to drilling fluid and its impact on pressure loss.
- Consider a multiphase flow pattern, along with the presence of dispersed cuttings flowing through the annular area.

Nomenclature

Symbol

A	cross-sectional area of duct, pipe and annular, m
$\hat{A}$	constant
A_f	area of flow, m^2
a	geometric parameter
a_0	constant
a_1	constant
a_2	constant
a_3	constant
a_{bi}	bipolar coordinate system
$\hat{B}$	constant
b	geometric parameter
$\hat{C}$	constant
C_1	constant
C_2	constant
C_3	constant
$C_{1\varepsilon}$	constant
$C_{2\varepsilon}$	constant
C_μ	constant
c_r	concentric radial clearance, m

D	diameter of pipe, m
$\widehat{D}$	constant
D_h	hydraulic diameter, m
D_i	inner diameter, m
D_o	outer diameter, m
d	distance of central axis of inner and outer cylinder, m
$\widehat{E}$	constant
e	relative eccentricity
$\widehat{F}$	constant
f	fanning friction factor
fRe	friction factor- Reynolds number
fRe_{ecc}	friction factor- Reynolds number for eccentric annulus
fRe_g	friction factor- Reynolds number (generalized)
f_x	gravity in the x-direction, m/s^2
f_y	gravity in the y-direction, m/s^2
f_z	gravity in the z-direction, m/s^2
$\widehat{G}$	constant
G_k	turbulent kinetic energy due to mean velocity gradient
G_b	turbulent kinetic energy due to buoyancy
H	bed height, m
H_{bed}	dimensionless bed height, (%)
H_{max}	maximum height, m

h	height, m
i	inner
$\hat{\imath}$	component in the corresponding direction
$\hat{\jmath}$	component in the corresponding direction
K	consistency index, Pa.s^n
L	length, m
L_{third}	third axis
ΔL	change in length, m
n	power-law index
o	outer
k	turbulent kinetic energy
P	pressure, Pa
P_W	wetted perimeter, m
dP/dL	frictional pressure loss gradient, Pa/m
$\bar{p}$	mean average pressure
dp/dz	pressure gradient, Pa/m
Q	flow rate, gal/min
$\bar{Q}$	dimensionless flow rate
$\bar{Q}_{D(c,e)}$	dimensionless flowrate for concentric or eccentric annulus
R	radius, m
R_i	radius of inner cylinder, m
R_o	radius of outer cylinder, m

Re	Reynolds number
Re^*	Reynolds number for annulus using power-law fluid
Re_{ecc}	Reynolds number for eccentric annulus
Re_g	generalized Reynolds number
r_i	inner radius, m
r_o	outer radius, m
S_k	user-defined source term
S_ε	user-defined source term
S_U	non-uniform viscous source term (X-component)
S_V	non-uniform viscous source term (X-component)
S_W	non-uniform viscous source term (X-component)
s	shape factor
U	non-uniform viscosity source term (X-component)
u	local axial velocity (x-axis), m/s
V	non-uniform viscosity source term (Y-component)
$\bar{V}$	mean flow velocity, m/s
v	local fluid velocity (y-axis), m/s
W	non-uniform viscosity source term (Z-component)
$\bar{W}$	width of equivalent slot
W_i	inner pipe width, m
W_{bed}	bed width, m
X	eccentric annular distance x-axis, m
X_L	dimensionless x-axis

X_M	fluctuating dilatation
x	x-axis
dx	changes with x-axis
Y	eccentric annular distance y-axis, m
Y_V	dimensionless y-axis
y	x-axis
dy	changes with x-axis
z	z-axis
dz	changes with z-axis

Greek Symbols

α	constant
α_0	constant
α_1	constant
α_2	constant
α_3	constant
δ	distance between axis of inner and outer pipe, m
ε	rate of dissipation
ξ	constant
ΔV_{vol}	volume of fluid passing through control volume, m^3
ΔP	pressure drop, Pa

Δt	variation in time, s
$\dot{\gamma}$	shear rate, 1/s
μ	viscosity of Newtonian fluid, Pa.s
μ_t	turbulent viscosity/eddy viscosity
μ_{eff}	effective viscosity
$\mu(\dot{\gamma})$	apparent viscosity, Pa.s
η	constant
θ	θ-axis
κ	diameter ratio, $\kappa = D_i/D_o = R_i/R_o$
ρ	density, kg/m^3
τ	shear stress, Pa
$\partial\tau_{\hat{\imath},\hat{\jmath}}/\partial x$	viscosity dependent momentum exchange term
$\partial\tau_{\hat{\imath},\hat{\jmath}}/\partial y$	viscosity dependent momentum exchange term
$\partial\tau_{\hat{\imath},\hat{\jmath}}/\partial z$	viscosity dependent momentum exchange term
τ_w	wall shear stress, Pa
$\tau_{w,a}$	annular wall shear stress, Pa
$\tau_{w,p}$	pipe wall shear stress, Pa
τ_{bed}	bed shear stress, Pa
$\bar{\tau}_{bed}$	average bed shear stress, Pa
$\bar{\tau}_w$	average wall shear stress, Pa
σ	turbulent Prandtl number
ϵ	roughness of pipe

π_{bed}	dimensionless bed shear stress
Π_{bed}	correlation for dimensionless bed shear stress

Acronyms

CFD	Computational Fluid Dynamics
ECD	Equivalent Circulating Density
WBM	Water Based Mud
YPL	Yield power-law

References

Adari, R.B. 1999. Development of Correlations Relating Bed Erosion to Flowing Time for Near Horizontal Wells. MS thesis, University of Tulsa, USA.

Ahmed, R., P. Skalle, and S. T. Johansen. 2003. A Mechanistic Model to Determine the Critical Flow Velocity Required to Initiate the Movement of Spherical Bed Particles in Inclined Channels. *Chemical Engineering Science* 58 (10): 2153–2163. https://doi.org/10.1016/S0009-2509(03)00061-7.

Ahmed, R., Miska, S. and Miska, W. 2006. Friction Pressure Loss Determination of Yield Power Law Fluid in Eccentric Annular Laminar Flow. Wiertnictwo, Nafta, *Gaz* R. 23/1: 47–53.

Ahmed, R, and Miska, S. 2008. Experimental Study and Modeling of Yield Power-Law Fluid Flow in Annuli with Drillpipe Rotation. SPE/IADC Drilling Conference, Proceedings 1 (January). https://doi.org/10.2118/112604-MS.

Ahmed, R.M. and Miska, S.Z. 2009. Drilling Hydraulics: Advanced Drilling and Well Technology, Edited by: Aadnoy, B.; Cooper, I.; Miska, S.; Mitchell, R.F.; Payne, M.L., Society of Petroleum Engineering, Chap 4.1, 191-220.

ANSYS®. 2019. Academic Research Mechanical, Release 18.1, Help System, Coupled Field Analysis Guide, ANSYS, Inc.

Aworunse, O.A. 2012. Modeling of Power-Law Fluid Flow in Annulus with Cutting Bed Buildup. MS Thesis, the University of Oklahoma, Norman, OK.

Azouz, Idir, Siamack A. Shirazi, Ali Pilehvari, and J. J. Azar. 1993. Numerical Simulation of Laminar Flow of Yield-Power-Law Fluids in Conduits of Arbitrary Cross-Section. *Journal of Fluids Engineering* 115 (4): 710–16. https://doi.org/10.1115/1.2910203.

Bicalho, I. C., D. B. L. dos Santos, C. H. Ataíde, and C. R. Duarte. 2016a. Fluid-Dynamic Behavior of Flow in Partially Obstructed Concentric and Eccentric Annuli with Orbital Motion. *Journal of Petroleum Science and Engineering* 137 (January): 202–13. https://doi.org/10.1016/j.petrol.2015.11.029.

Bicalho, Isabele Cristina, José Lucas Mognon, Carlos Henrique Ataíde, and Claudio Roberto Duarte. 2016b. Fluid Dynamics Study of the Flow and Pressure Drop Analysis of a Non-Newtonian Fluid through Annular Ducts with Unusual Cross-Sections. *The Canadian Journal of Chemical Engineering* 94 (2): 391–401. https://doi.org/10.1002/cjce.22401.

Bourgoyne, Adam T. 1991. Applied Drilling Engineering. Richardson, TX: Society of Petroleum Engineers.

Brighton, J. A., and J. B. Jones. 1964. Fully Developed Turbulent Flow in Annuli. *Journal of Basic Engineering* 86 (4): 835–42. https://doi.org/10.1115/1.3655966.

Chen, Z. 2005. Cuttings Transport with Foam in Horizontal Concentric Annulus under Elevated Pressure and Temperature Conditions. PhD Dissertation, The University of Tulsa, OK, 190-191.

Clark, R. K., and K. L. Bickham. 1994. A Mechanistic Model for Cuttings Transport. In . Society of Petroleum Engineers. https://doi.org/10.2118/28306-MS.

Colebrook, C. F., and C. M. White. 1937. Experiments with Fluid Friction in Roughened Pipes. *Proceedings of the Royal Society of London. Series A, Mathematical and Physical Sciences* 161 (906): 367–81.

Cui, Hai-qing, and Xi-Sheng Liu. 1995. Research on Helical Flow of Non-Newtonian Fluids in Eccentric Annuli. In . Society of Petroleum Engineers. https://doi.org/10.2118/29940-MS.

Deissler, R. G. 1955. Analysis of Turbulent Heat Transfer, Mass Transfer, and Friction in Smooth Tubes at High Prandtl and Schmidt Numbers. NACA-1210. Lewis Flight Propulsion Lab., Cleveland. https://www.osti.gov/biblio/4359415-analysis-turbulent-heat-transfer-mass-transfer-friction-smooth-tubes-high-prandtl-schmidt-numbers.

Deissler, Robert G., and Maynard F. Taylor. 1955. Analysis of Fully Developed Turbulent Heat Transfer and Flow in an Annulus With Various Eccentricities. Report. Digital Library. May 1955. https://digital.library.unt.edu/ark:/67531/metadc57459/.

Dodge, D. W., and A. B. Metzner. 1959. Turbulent flow of non-Newtonian systems. *AIChE Journal* 5 (2): 189–204. https://doi.org/10.1002/aic.690050214.

Ebrahim, Nuha Hussein, Noaman El-Khatib, and Mariyamni Awang. 2013. Numerical Solution of Power-Law Fluid Flow through Eccentric Annular Geometry. *American Journal of Numerical Analysis* 1 (1): 1–7. https://doi.org/10.12691/ajna-1-1-1.

Escudier, Marcel, I.W. Gouldson, Paulo Oliveira, and Fernando Pinho. 2000. Effects of Inner Cylinder Rotation on Laminar Flow of a Newtonian Fluid through an Eccentric Annulus. *International Journal of Heat and Fluid Flow* 21 (February): 92–103. https://doi.org/10.1016/S0142-727X(99)00059-4.

Fang, P., R. M. Manglik, and M. A. Jog. 1999. Characteristics of Laminar Viscous Shear-Thinning Fluid Flows in Eccentric Annular Channels. *Journal of Non-Newtonian Fluid Mechanics* 84 (1): 1–17. https://doi.org/10.1016/S0377-0257(98)00145-1.

Filip, Petr, and J. David. 2003. Axial Couette-Poiseuille Flow of Power-Law Viscoplastic Fluids in Concentric Annuli. *Journal of Petroleum Science and Engineering -Journal of Petroleum Science and Engineering* 40 (December): 111–19. https://doi.org/10.1016/S0920-4105(03)00107-4.

Founargiotakis, K., V. C. Kelessidis, and R. Maglione. 2008. Laminar, Transitional and Turbulent Flow of Herschel–Bulkley Fluids in Concentric Annulus. *The Canadian Journal of Chemical Engineering* 86 (4): 676–83. https://doi.org/10.1002/cjce.20074.

George, Matthew, Rida Elgaddafi, Ramadan Ahmed, and Frederick Growcock. 2014. Performance of Fiber-Containing Synthetic-Based Sweep Fluids. *Journal of Petroleum Science and Engineering* 119 (July). https://doi.org/10.1016/j.petrol.2014.05.009.

Gucuyener, Ismail Hakki, and Tanju Mehmetoğlu. 2004. Flow of Yield-pseudo-plastic Fluids through a Concentric Annulus. *AIChE Journal* 38 (June): 1139–43. https://doi.org/10.1002/aic.690380717.

Haaland, S. E. 1983. Simple and Explicit Formulas for the Friction Factor in Turbulent Pipe Flow. *Journal of Fluids Engineering* 105 (1): 89–90. https://doi.org/10.1115/1.3240948.

Haciislamoglu, M., and J. Langlinais. 1990. Non-Newtonian Flow in Eccentric Annuli. *Journal of Energy Resources Technology* 112 (3): 163–69. https://doi.org/10.1115/1.2905753.

Haciislamoglu, Mustafa. 1989. Non-Newtonian Fluid Flow in Eccentric Annuli and Its Application to Petroleum Engineering Problems. *LSU Historical Dissertations and Theses*, January. https://digitalcommons.lsu.edu/gradschool_disstheses/4848.

Hanks, Richard W. 1979. The Axial Laminar Flow of Yield-Pseudoplastic Fluids in a Concentric Annulus. *Industrial & Engineering Chemistry Process Design and Development* 18 (3): 488–93. https://doi.org/10.1021/i260071a024.

Herschel, Winslow H., and Ronald Bulkley. 1926. Konsistenzmessungen von Gummi-Benzollösungen. *Kolloid-Zeitschrift* 39 (4): 291–300. https://doi.org/10.1007/BF01432034.

Heyda, James F. 1959. A Green's Function Solution for the Case of Laminar Incompressible Flow between Non-Concentric Circular Cylinders. *Journal of the Franklin Institute* 267 (1): 25–34. https://doi.org/10.1016/0016-0032(59)90034-1.

Holland, F. A. 1995. Fluid Flow for Chemical Engineers. 2nd ed. / F.A. Holland, R. Bragg.. London: Edward Arnold. https://ezproxy.lib.ou.edu/login?url=https://app.knovel.com/hotlink/toc/id:kpFFCEE005/fluid-flow-for?kpromoter=marc.

Hussain, Quazi E., and Muhammad A. R. Sharif. 1997. Viscoplastic Fluid Flow in Irregular Eccentric Annuli Due to Axial Motion of the Inner Pipe. *The Canadian Journal of Chemical Engineering* 75 (6): 1038–45. https://doi.org/10.1002/cjce.5450750606.

Iyoho, Aniekan W., and Jamal J. Azar. 1981. An Accurate Slot-Flow Model for Non-Newtonian Fluid Flow Through Eccentric Annuli. *Society of Petroleum Engineers Journal* 21 (05): 565–72. https://doi.org/10.2118/9447-PA.

Jonsson, V. K., and E. M. Sparrow. 1965. Results of Laminar Flow Analysis and Turbulent Flow Experiments for Eccentric Annular Ducts. *AIChE Journal* 11 (6): 1143–45. https://doi.org/10.1002/aic.690110635.

Jonsson, V. K., and E. M. Sparrow. 1966. Experiments on Turbulent-Flow Phenomena in Eccentric Annular Ducts. *Journal of Fluid Mechanics* 25 (1): 65–86. https://doi.org/10.1017/S0022112066000053.

Klinzing, G. E., F. Rizk, R. Marcus, and L. S. Leung. 2010. Pneumatic Conveying of Solids: A Theoretical and Practical Approach. Vol. 8. Particle Technology Series. Dordrecht: Springer Netherlands.

Kozicki, W., C. H. Chou, and C. Tiu. 1966. Non-Newtonian Flow in Ducts of Arbitrary Cross-Sectional Shape. *Chemical Engineering Science* 21 (8): 665–79. https://doi.org/10.1016/0009-2509(66)80016-7.

Li, Y., Nancy Bjorndalen, and Ergun Kuru. 2007. Numerical Modelling of Cuttings Transport in Horizontal Wells Using Conventional Drilling Fluids. *Journal of Canadian Petroleum Technology - J CAN PETROL TECHNOL* 46 (July). https://doi.org/10.2118/07-07-TN.

Liu, John, Murray R Spiegel, and Murray R Spiegel. 1999. Mathematical Handbook of Formulas and Tables. New York: McGraw-Hill. http://search.ebscohost.com/login.aspx?direct=true&scope=site&db=nlebk&db=nlabk&AN=12910.

McCann, R. C., M. S. Quigley, Mario Zamora, and K. S. Slater. 1995. Effects of High-Speed Pipe Rotation on Pressures in Narrow Annuli. *SPE Drilling & Completion* 10 (02): 96–103. https://doi.org/10.2118/26343-PA.

Nguyen, Hung, and Diep Nguyen Ngoc. 2012. Incompressible Non-Newtonian Fluid Flows. In . https://doi.org/10.5772/26091.

Nouri, J. M., H. Umur, and J. H. Whitelaw. 1993. Flow of Newtonian and Non-Newtonian Fluids in Concentric and Eccentric Annuli. *Journal of Fluid Mechanics* 253 (August): 617–41. https://doi.org/10.1017/S0022112093001922.

Ogino, F., T. Sakano, and T. Mizushina. 1987. Momentum and Heat Transfers from Fully Developed Turbulent Flow in an Eccentric Annulus to Inner and Outer Tube Walls. *Wärme - Und Stoffübertragung* 21 (2): 87–93. https://doi.org/10.1007/BF01377564.

Piercy N.A.V, Hooper, M.S., and Winny, H.F. 1933.Viscous Flow through pipes with core. *London Edinburgh Dublin Phil. Mag. J. Sci.,* 15, 647-676

Pilehvari, Ali, and Robert Serth. 2009. Generalized Hydraulic Calculation Method for Axial Flow of Non-Newtonian Fluids in Eccentric Annuli. *SPE Drilling & Completion* 24 (04): 553–63. https://doi.org/10.2118/111514-PA.

Purushothaman, Venkitaraj Konery. n.d. Laminar and Turbulent Flows in Pipes. Accessed October 27, 2019. https://www.academia.edu/3157721/Laminar_and_Turbulent_Flows_in_Pipes.

Rojas, Silvia. 2016. Flow of Power-Law Fluid in a Partially Blocked Eccentric Annulus, December. https://shareok.org/handle/11244/47115.

Rojas, Silvia, Ramadan Ahmed, Rida Elgaddafi, and Matthew George. 2017. Flow of Power-Law Fluid in a Partially Blocked Eccentric Annulus. *Journal of Petroleum Science and Engineering* 157 (August): 617–30. https://doi.org/10.1016/j.petrol.2017.07.060.

Singh, Ajay Pratap, and Robello Samuel. 2009. Effect of Eccentricity and Rotation on Annular Frictional Pressure Losses With Standoff Devices. In . Society of Petroleum Engineers. https://doi.org/10.2118/124190-MS.

Snyder, William T., and Gerald A. Goldstein. 1965. An Analysis of Fully Developed Laminar Flow in an Eccentric Annulus. *AIChE Journal* 11 (3): 462–67. https://doi.org/10.1002/aic.690110319.

Sorgun, M. 2011. Computational Fluid Dynamics Modeling of Pipe Eccentricity Effect on Flow Characteristics of Newtonian and Non-Newtonian Fluids. *Energy Sources, Part A: Recovery, Utilization, and Environmental Effects* 33 (12): 1196–1208. https://doi.org/10.1080/15567036.2010.492381.

Sorgun, Mehmet, Erman Ulker, and Sila Korkut Uysal. 2018. A Numerical Approach for Modeling of Turbulent Newtonian Fluid Flow in Eccentric Annulus. *Teknik Dergi* 29 (July): 8497–8513. https://doi.org/10.18400/tekderg.336801.

Speigel, M. R., Mathematical Handbook of Formulas and Tables, McGraw-Hill Book Co., pp. 125-128, 1968.

Tang, Ming, Ramadan Ahmed, and Shiming He. 2016. Modeling of Yield-Power-Law Fluid Flow in a Partially Blocked Concentric Annulus. *Journal of Natural Gas Science and Engineering* 35 (September): 555–66. https://doi.org/10.1016/j.jngse.2016.09.001.

Tosun, Ismail. 1984. Axial Laminar Flow in an Eccentric Annulus: An Approximate Solution. *AIChE Journal* 30 (5): 877–78. https://doi.org/10.1002/aic.690300540.

Uner, Deniz, Canan Ozgen, and Ismail Tosun. 1988. An Approximate Solution for Non-Newtonian Flow in Eccentric Annuli. *Industrial & Engineering Chemistry Research* 27 (4): 698–701. https://doi.org/10.1021/ie00076a028.

Willenbacher, Norbert, and Kristina Georgieva. 2013. Rheology of Disperse Systems. In *Product Design and Engineering*, 7–49. John Wiley & Sons, Ltd. https://doi.org/10.1002/9783527654741.ch1.

Yue, Pengtao, Joseph Dooley, and James J. Feng. 2008. A General Criterion for Viscoelastic Secondary Flow in Pipes of Noncircular Cross Section. *Journal of Rheology* 52 (1): 315–32. https://doi.org/10.1122/1.2817674.

Appendix

Velocity Distributions for Diameter Ratio 0.25 (n = 1)

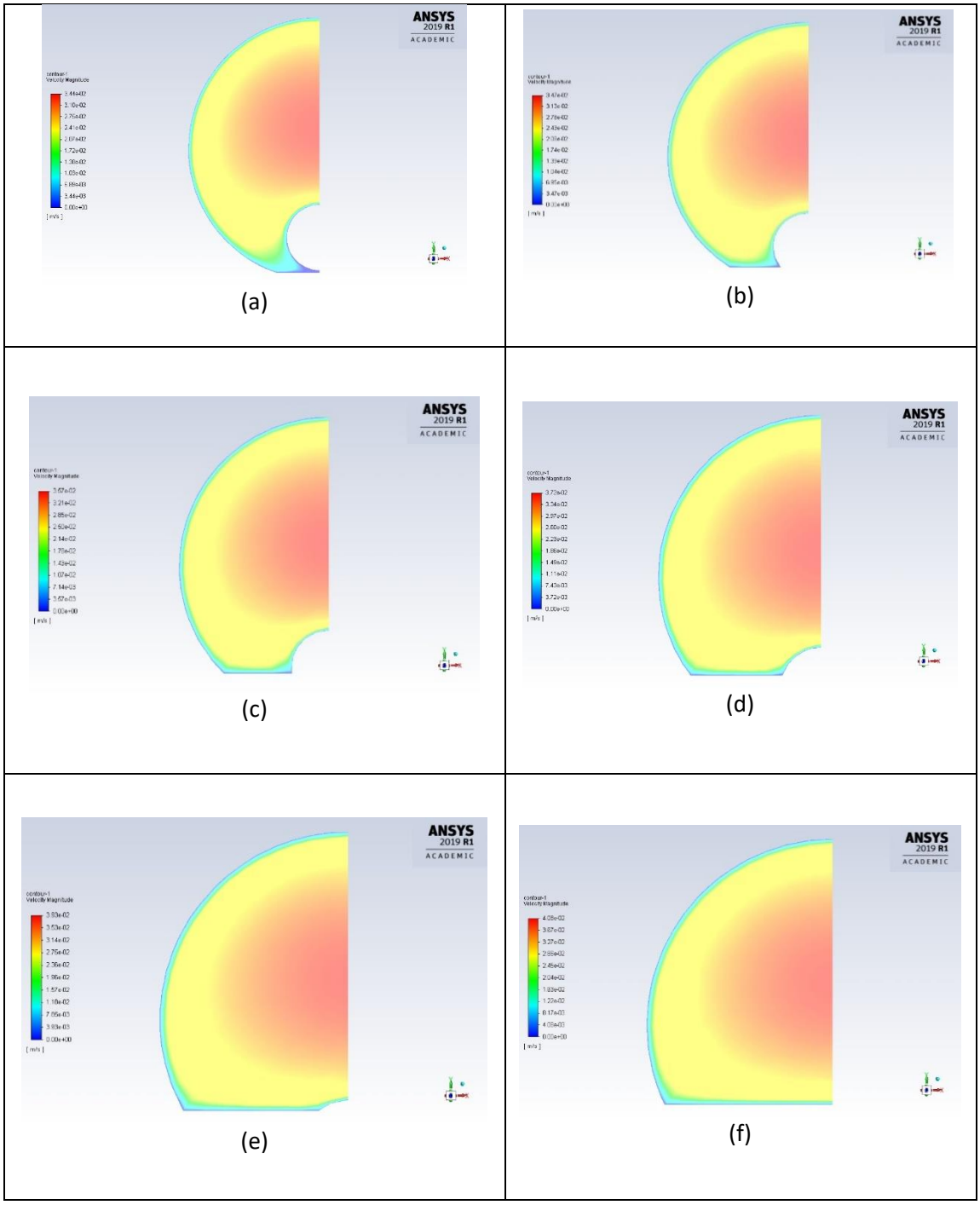

Figure A.1. Velocity distributions in partially blocked annuli [n = 1, κ = 0.25, e = 0.9 and Q = 5x10^{-5} m^3/s]: (a) H_{bed} = 10%; (b) H_{bed} = 30%; (c) H_{bed} = 50%; (d) H_{bed} = 70%; (e) H_{bed} = 90%; and (f) H_{bed} = 100%

Velocity Distributions for Diameter Ratio 0.25 (n = 0.8)

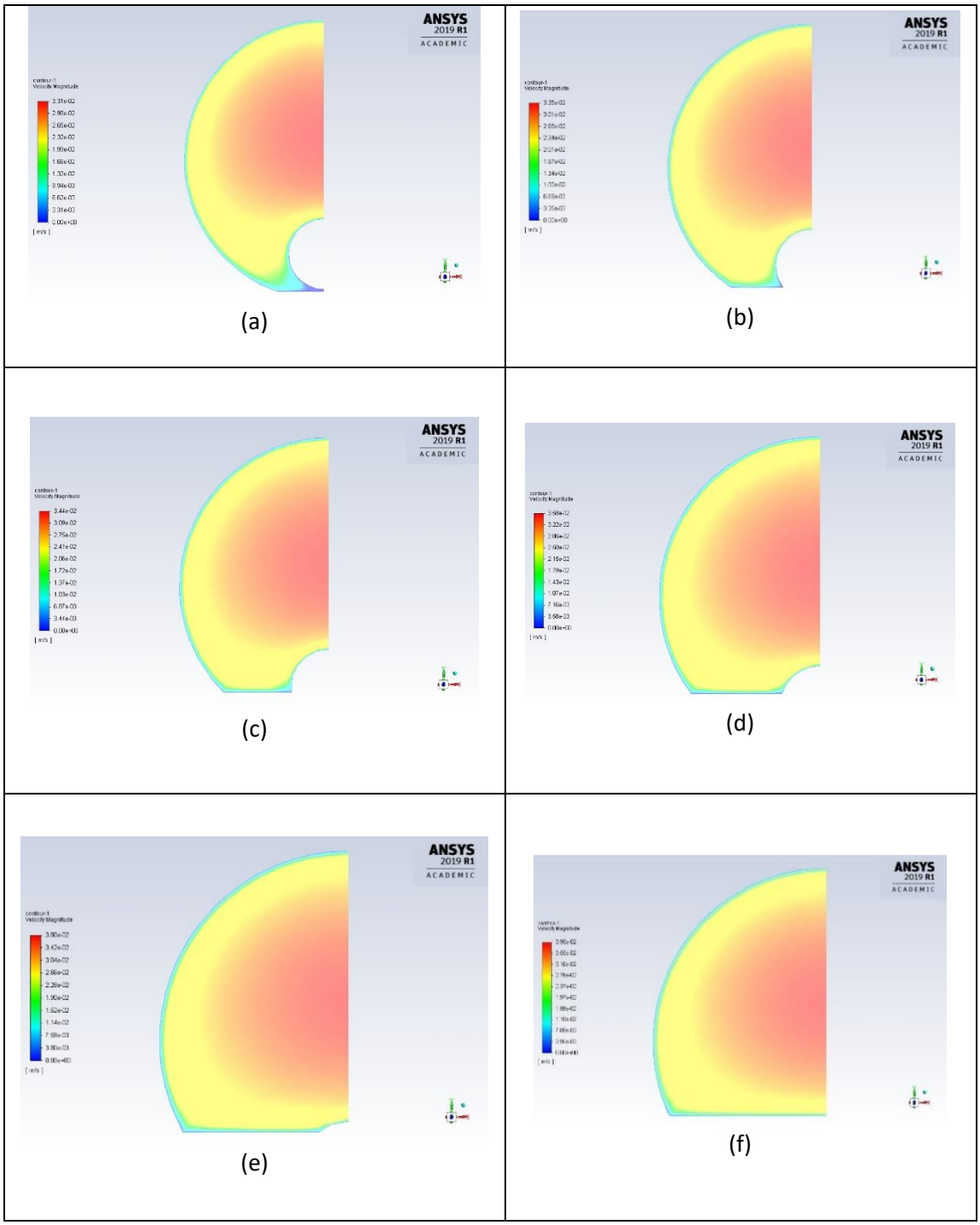

Figure A.2. Velocity distributions in partially blocked annuli [n = 0.8, κ = 0.25, e = 0.9 and Q = 5x10^{-5} m^3/s]: (a) H_{bed} = 10%; (b) H_{bed} = 30%; (c) H_{bed} = 50%; (d) H_{bed} = 70%; (e) H_{bed} = 90%; and (f) H_{bed} = 100%

Velocity Distributions for Diameter Ratio 0.25 (n = 0.6)

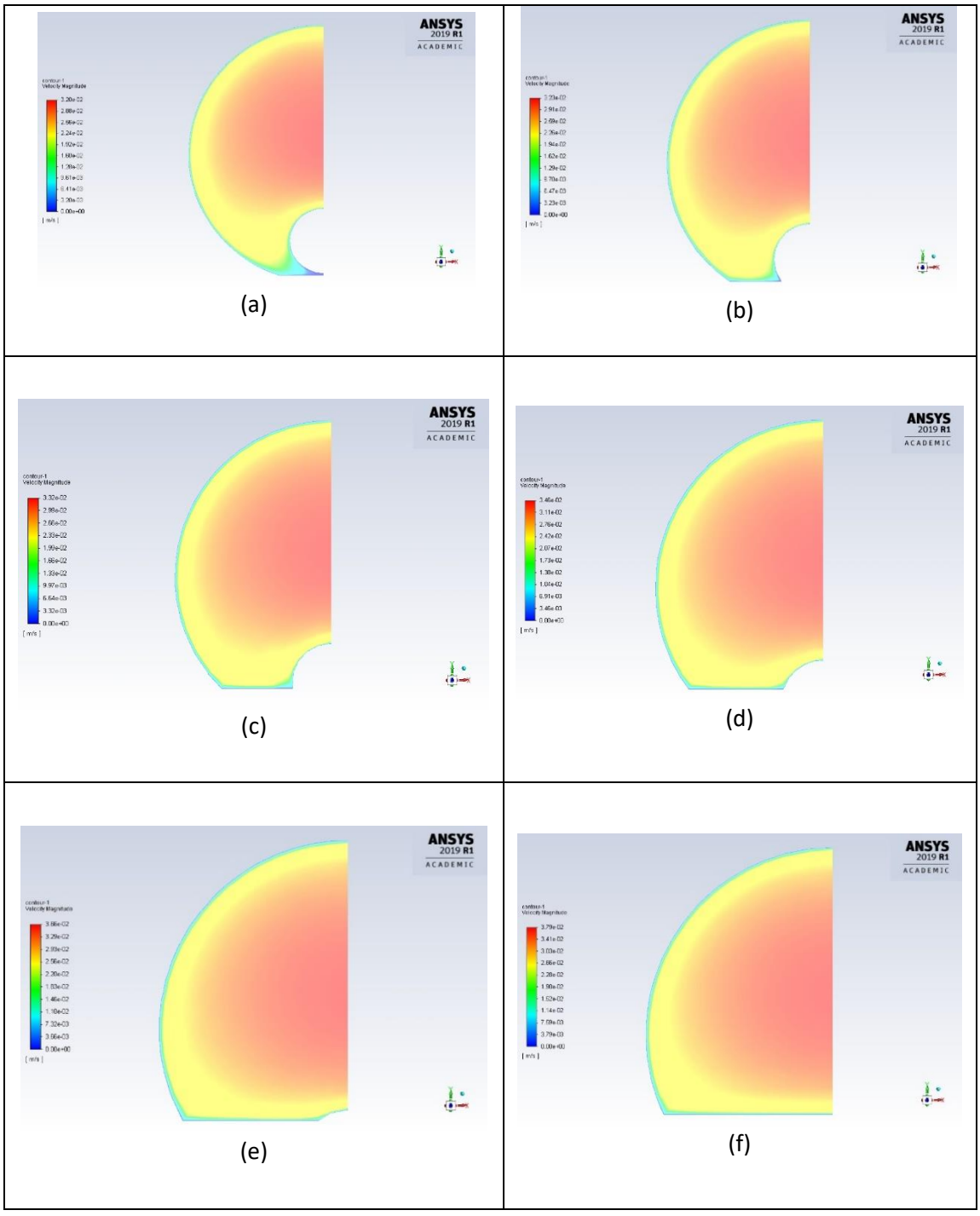

Figure A.3. Velocity distributions in partially blocked annuli [n = 0.6, κ = 0.25, e = 0.9 and Q = 5x10^{-5} m^3/s]: (a) H_{bed} = 10%; (b) H_{bed} = 30%; (c) H_{bed} = 50%; (d) H_{bed} = 70%; (e) H_{bed} = 90%; and (f) H_{bed} = 100%

Velocity Distributions for Diameter Ratio 0.25 (n = 0.4)

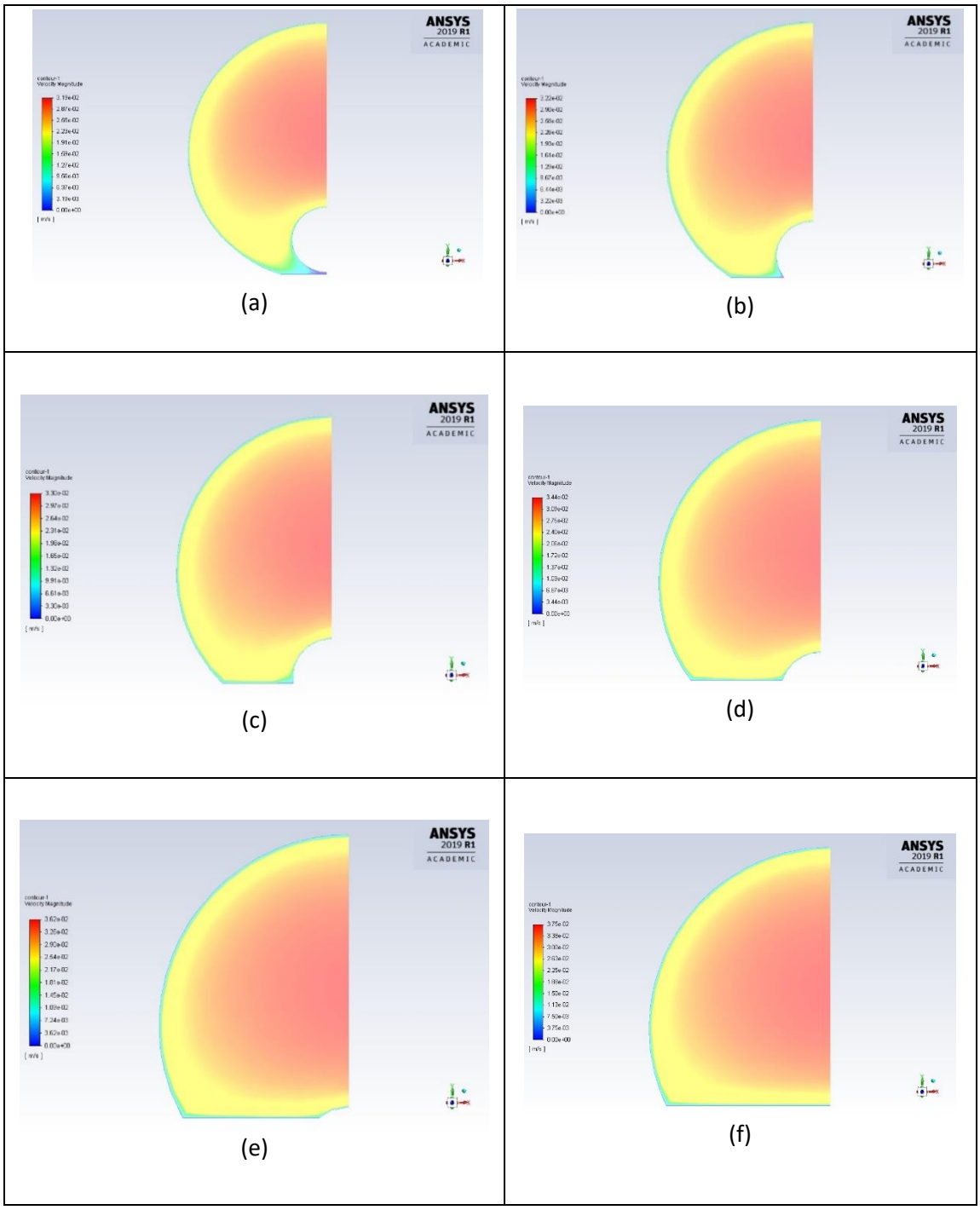

Figure A.4. Velocity distributions in partially blocked annuli [n = 0.4, κ = 0.25, e = 0.9 and Q = 5x10^{-5} m^3/s]: (a) H_{bed} = 10%; (b) H_{bed} = 30%; (c) H_{bed} = 50%; (d) H_{bed} = 70%; (e) H_{bed} = 90%; and (f) H_{bed} = 100%

Velocity Distributions for Diameter Ratio 0.25 (n = 0.2)

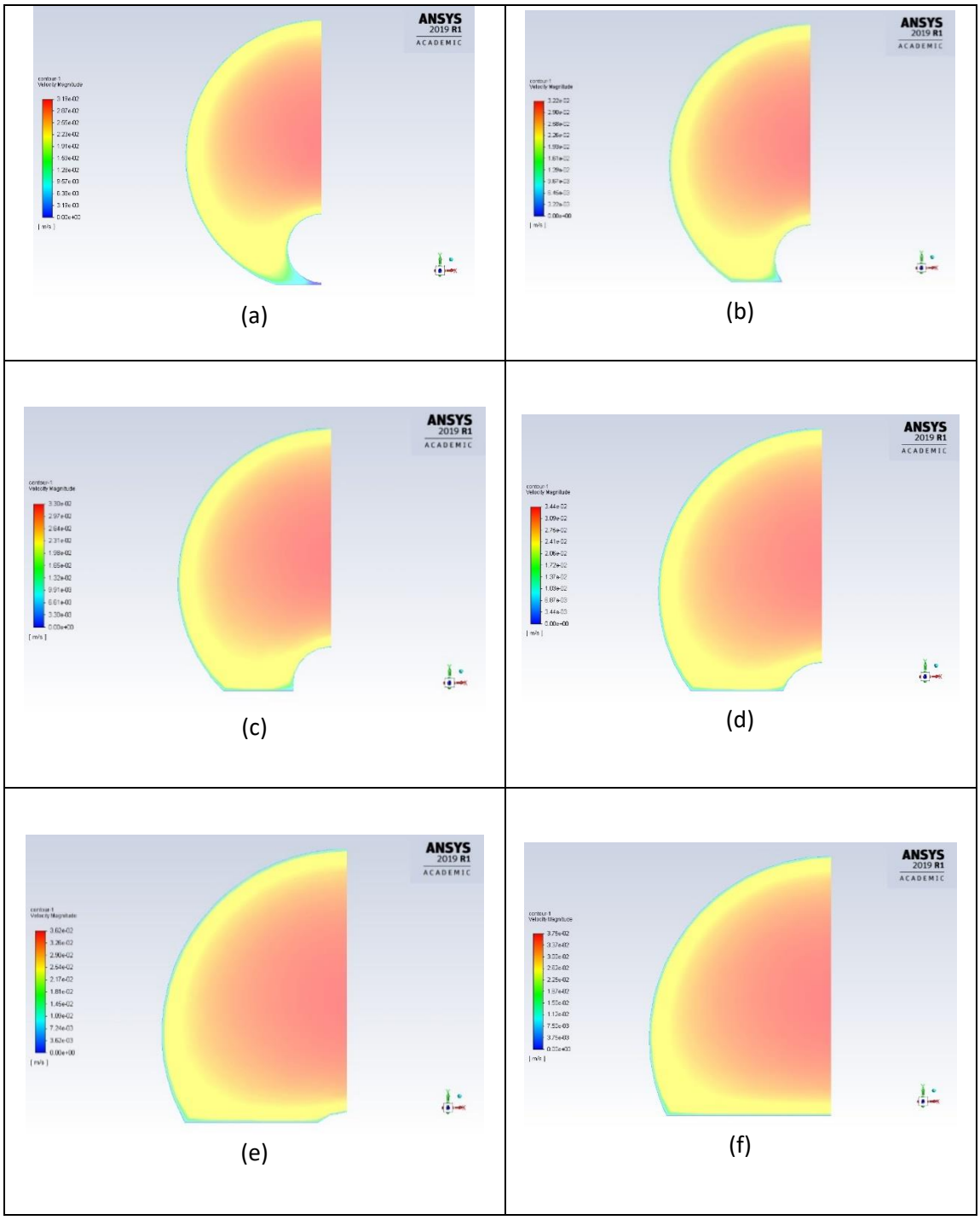

Figure A.5. Velocity distributions in partially blocked annuli [n = 0.2, κ = 0.25, e = 0.9 and Q = 5x10^{-5} m^3/s]: (a) H_{bed} = 10%; (b) H_{bed} = 30%; (c) H_{bed} = 50%; (d) H_{bed} = 70%; (e) H_{bed} = 90%; and (f) H_{bed} = 100%

Velocity Distributions for Diameter Ratio 0.25 and H_{bed} = 0%

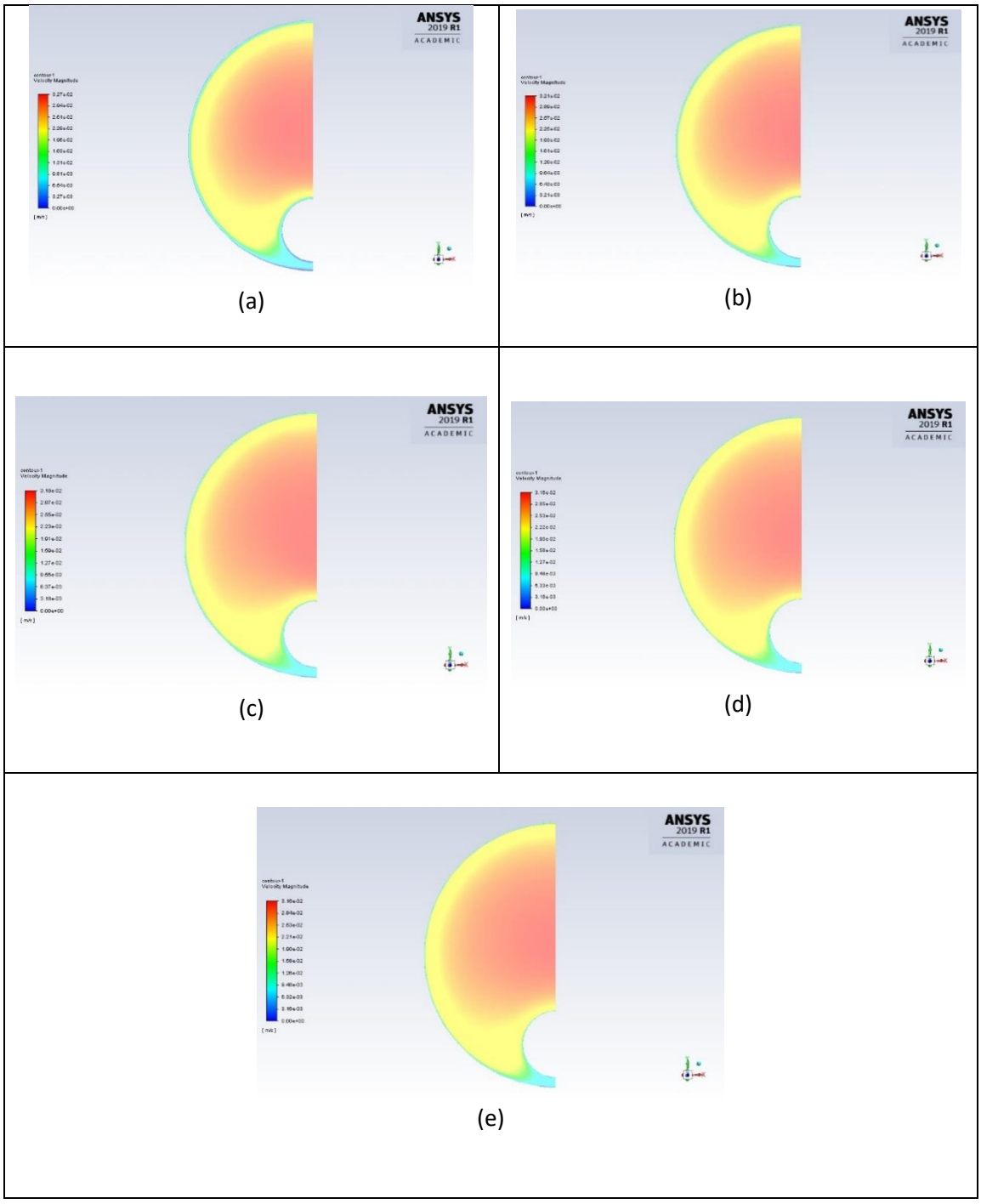

Figure A.6. Velocity distributions in unblocked annuli [κ = 0.25, e = 0.9 and Q = 5x10^{-5} m^3/s]: (a) n = 1; (b) n = 0.8; (c) n = 0.6; (d) n = 0.4; and (e) n = 0.2

Velocity Distributions for Diameter Ratio 0.50 (n = 1)

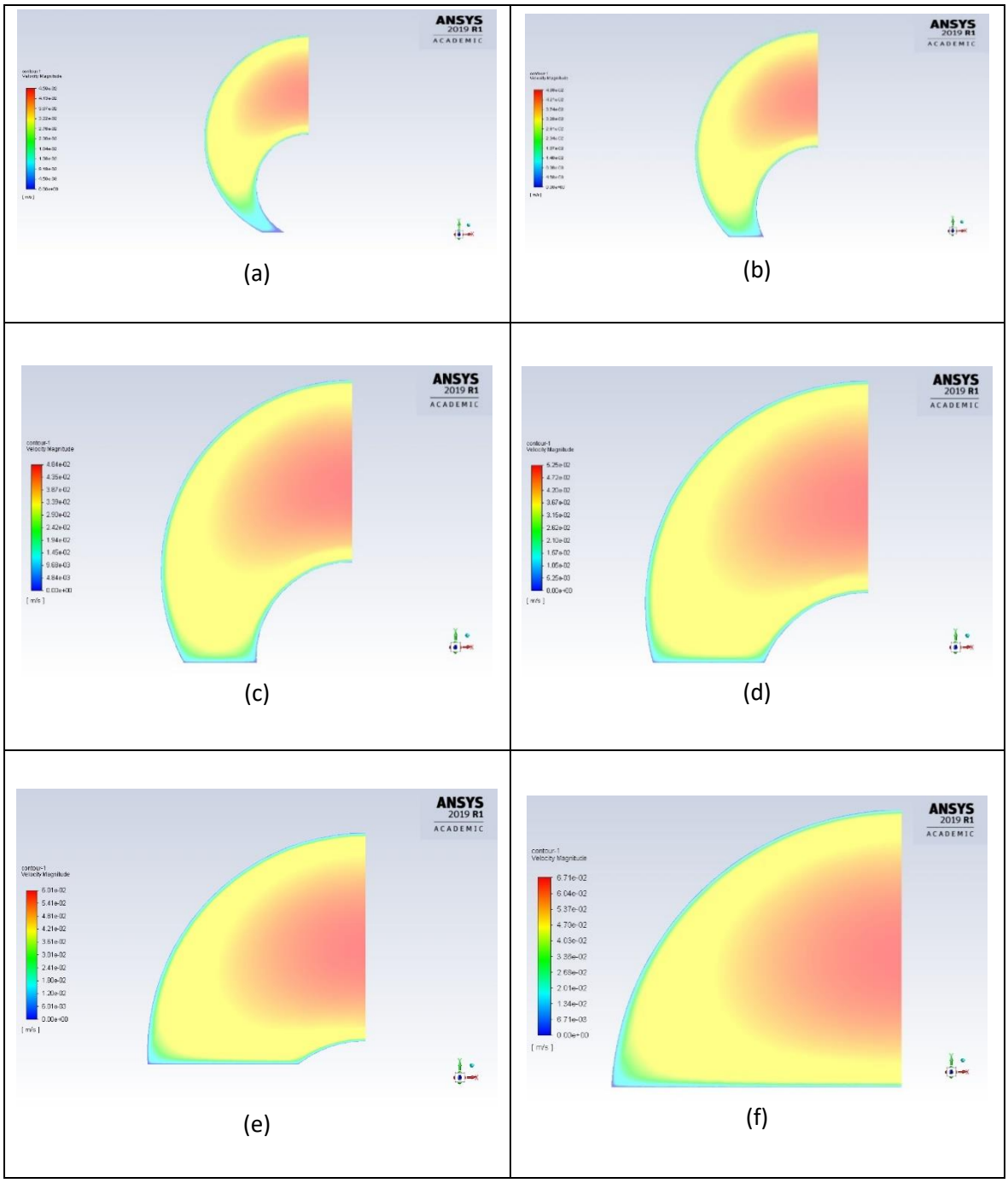

Figure A.7. Velocity distributions in partially blocked annuli [n = 1, κ = 0.50, e = 0.9 and Q = 5x10^{-5} m^3/s]: (a) H_{bed} = 10%; (b) H_{bed} = 30%; (c) H_{bed} = 50%; (d) H_{bed} = 70%; (e) H_{bed} = 90%; and (f) H_{bed} = 100%

Velocity Distributions for Diameter Ratio 0.50 (n = 0.8)

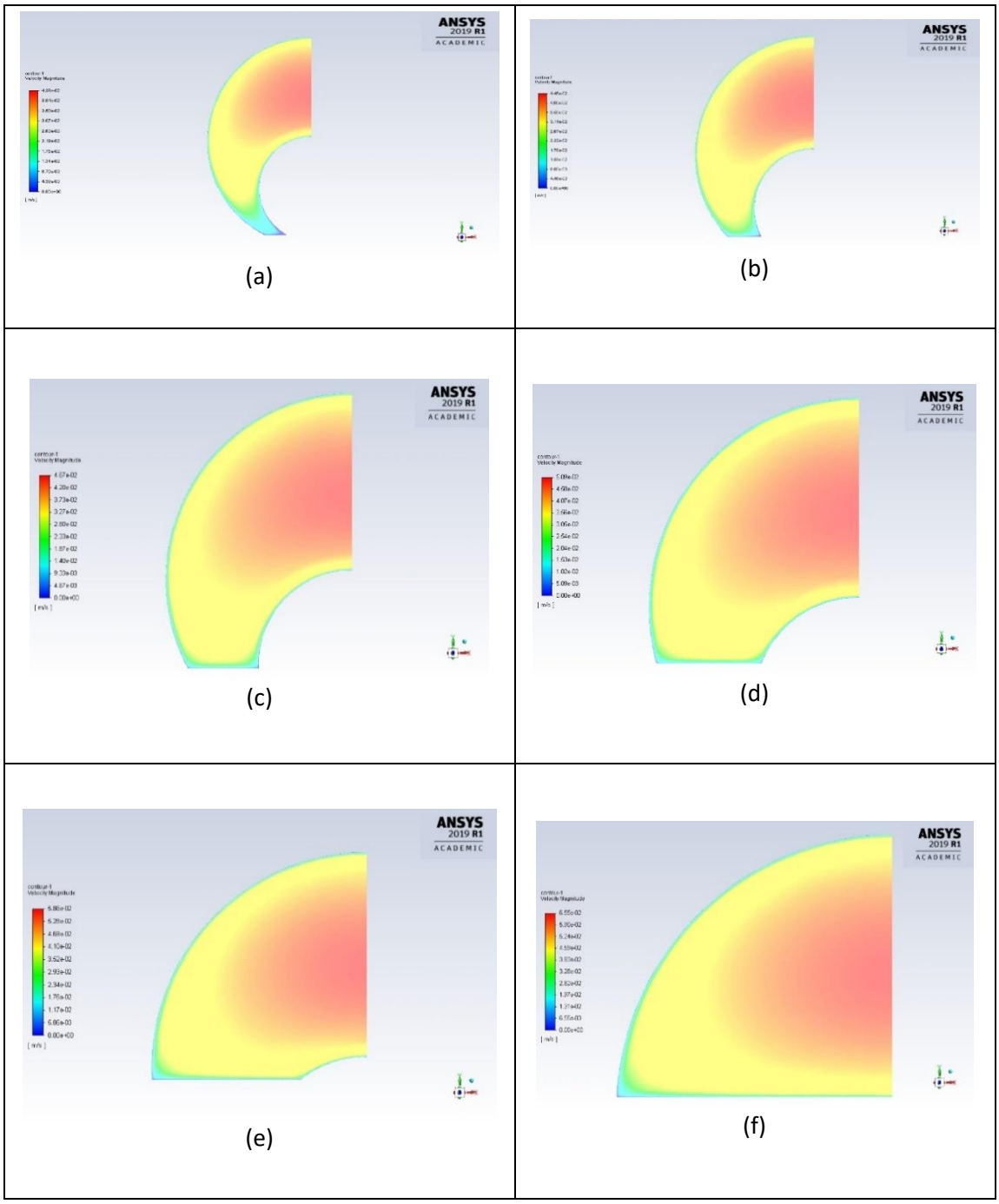

Figure A.8. Velocity distributions in partially blocked annuli [n = 0.8, κ = 0.50, e = 0.9 and Q = 5x10^{-5} m^3/s]: (a) H_{bed} = 10%; (b) H_{bed} = 30%; (c) H_{bed} = 50%; (d) H_{bed} = 70%; (e) H_{bed} = 90%; and (f) H_{bed} = 100%

Velocity Distributions for Diameter Ratio 0.50 (n = 0.6)

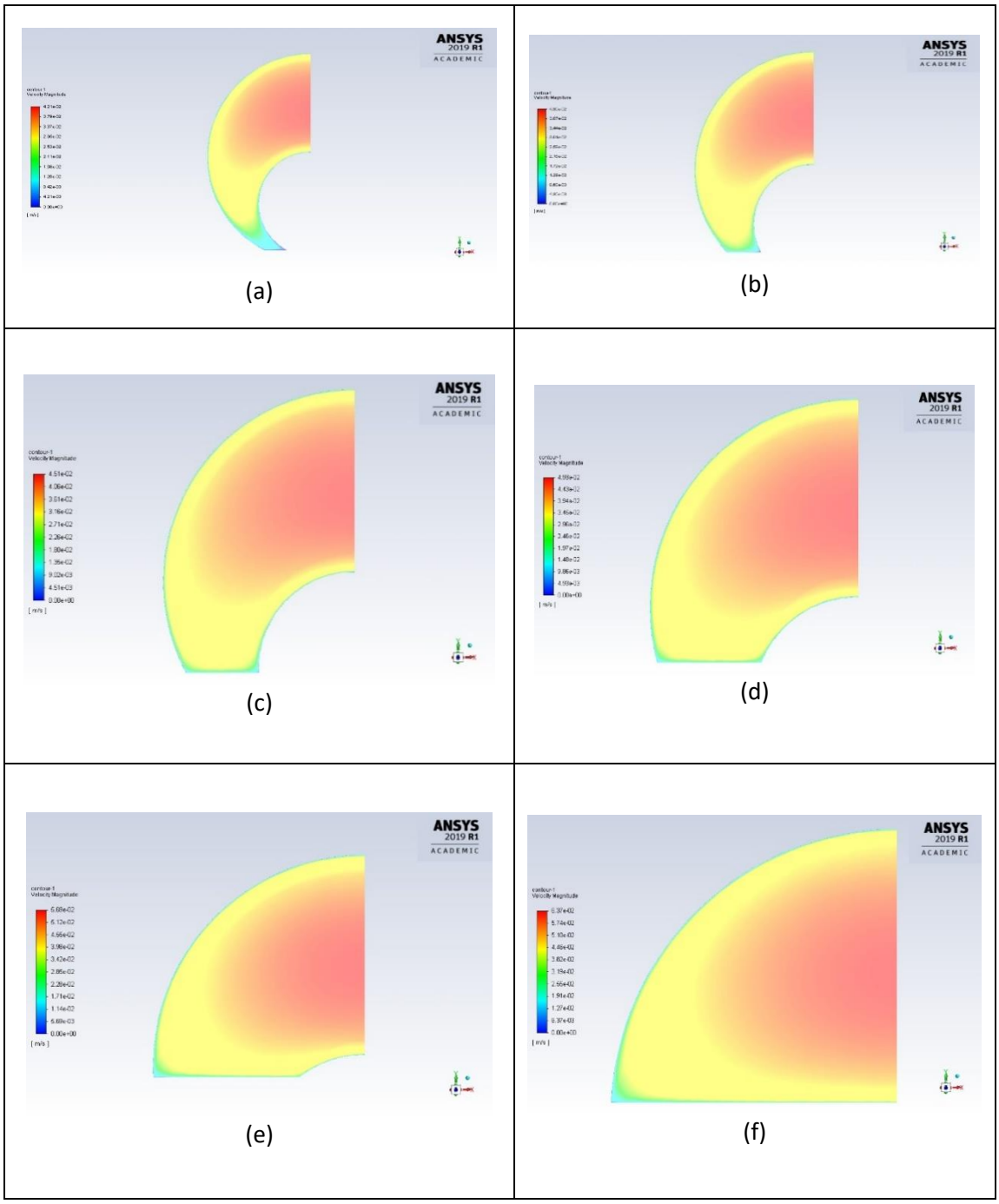

Figure A.9. Velocity distributions in partially blocked annuli [n = 0.6, κ = 0.50, e = 0.9 and Q = 5x10^{-5} m^3/s]: (a) H_{bed} = 10%; (b) H_{bed} = 30%; (c) H_{bed} = 50%; (d) H_{bed} = 70%; (e) H_{bed} = 90%; and (f) H_{bed} = 100%

Velocity Distributions for Diameter Ratio 0.50 (n = 0.4)

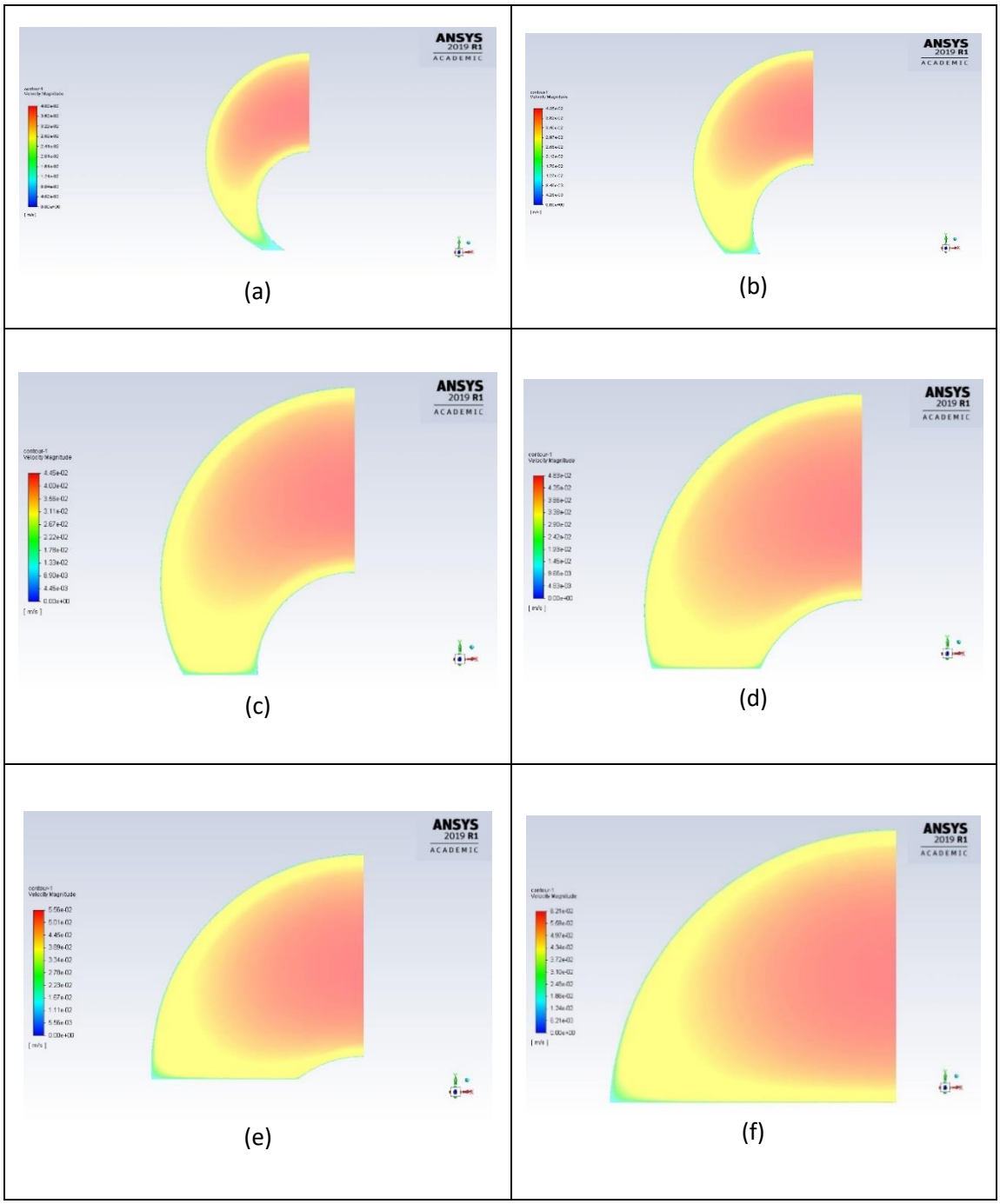

Figure A.10. Velocity distributions in partially blocked annuli [n = 0.4, κ = 0.50, e = 0.9 and Q = 5x10^{-5} m^3/s]: (a) H_{bed} = 10%; (b) H_{bed} = 30%; (c) H_{bed} = 50%; (d) H_{bed} = 70%; (e) H_{bed} = 90%; and (f) H_{bed} = 100%

Velocity Distributions for Diameter Ratio 0.50 (n = 0.2)

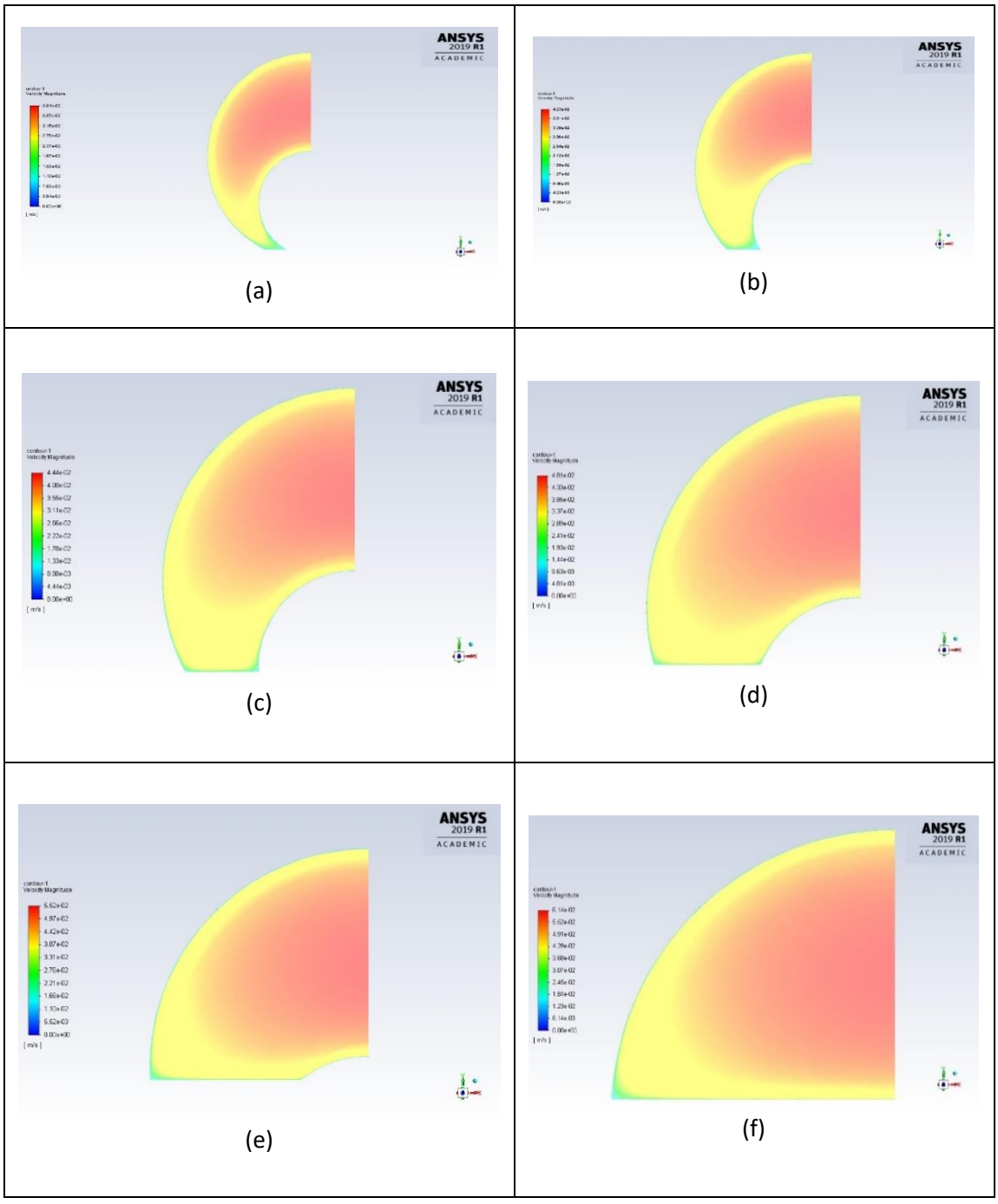

Figure A.11. Velocity distributions in partially blocked annuli [n = 0.2, κ = 0.50, e = 0.9 and Q = 5x10^{-5} m^3/s]: (a) H_{bed} = 10%; (b) H_{bed} = 30%; (c) H_{bed} = 50%; (d) H_{bed} = 70%; (e) H_{bed} = 90%; and (f) H_{bed} = 100%

Velocity Distributions for Diameter Ratio 0.50 and H_{bed} = 0%

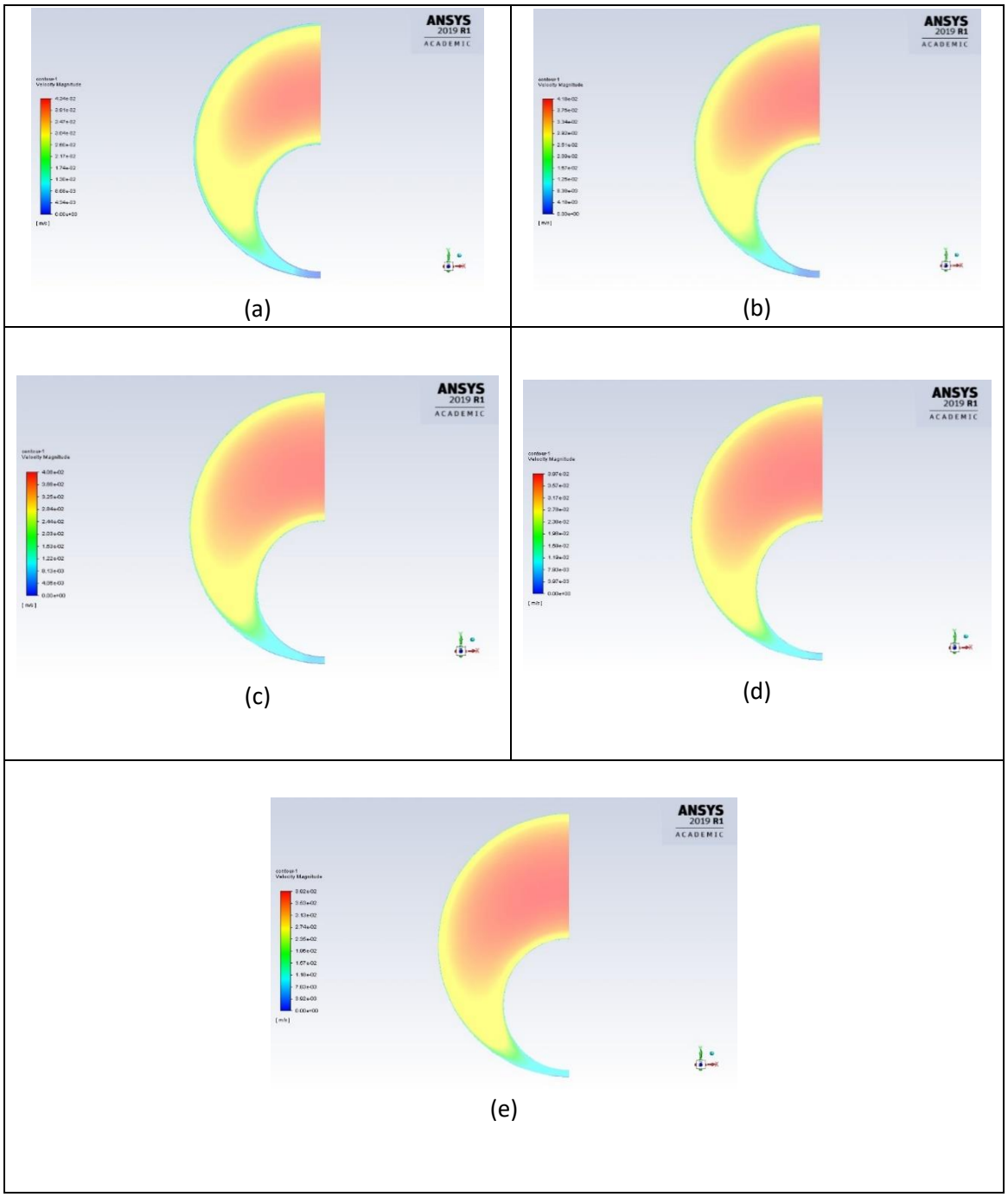

Figure A.12. Velocity distributions in unblocked annuli [κ = 0.50, e = 0.9 and Q = 5x10^{-5} m^3/s]: (a) n = 1; (b) n = 0.8; (c) n = 0.6; (d) n = 0.4; and (e) n = 0.2

Velocity Distributions for Diameter Ratio 0.75 (n = 1)

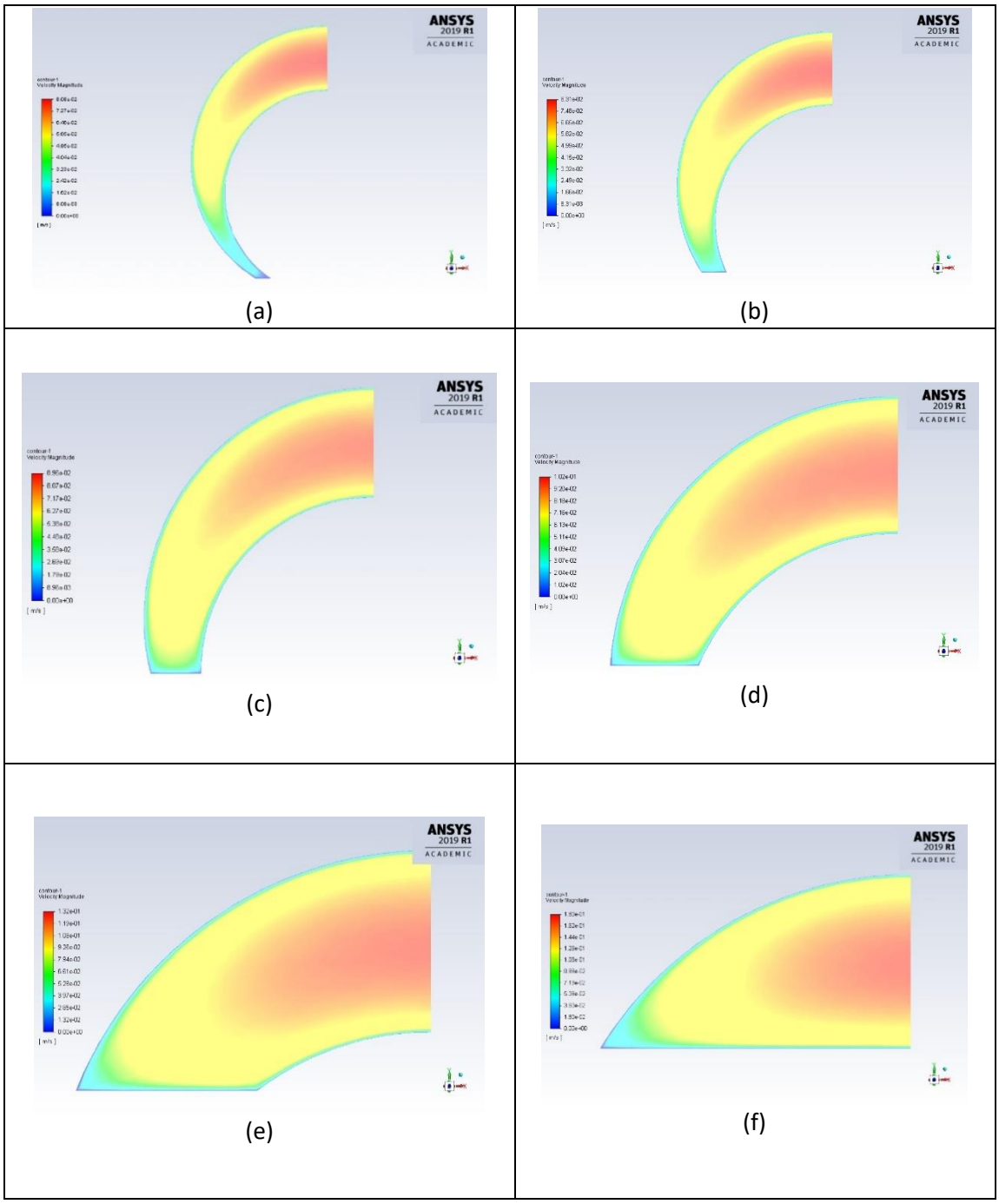

Figure A.13. Velocity distributions in partially blocked annuli [n = 1, κ = 0.75, e = 0.9 and Q = 5x10^{-5} m^3/s]: (a) H_{bed} = 10%; (b) H_{bed} = 30%; (c) H_{bed} = 50%; (d) H_{bed} = 70%; (e) H_{bed} = 90%; and (f) H_{bed} = 100%

Velocity Distributions for Diameter Ratio 0.75 (n = 0.8)

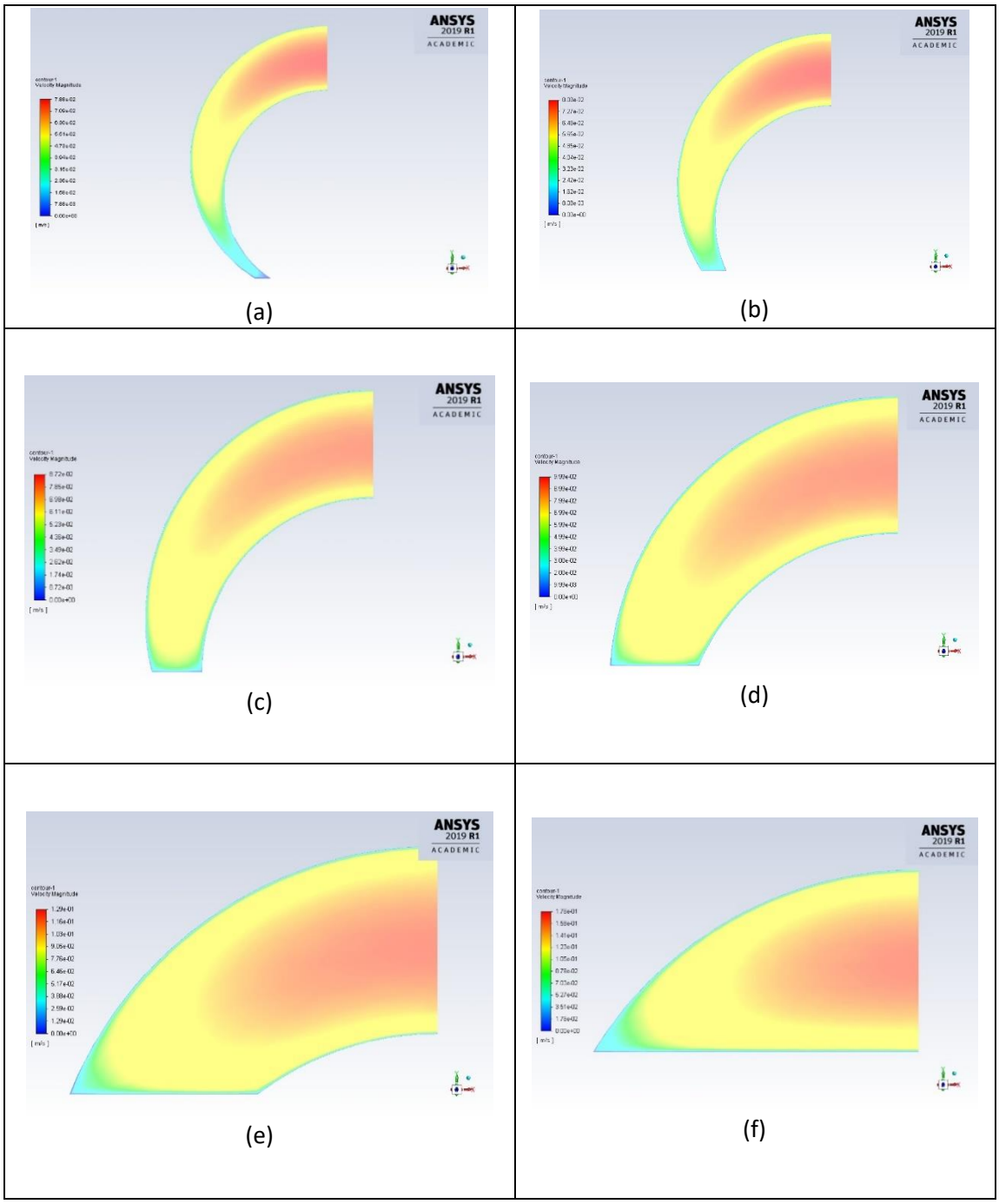

Figure A.14. Velocity distributions in partially blocked annuli [n = 0.8, κ = 0.75, e = 0.9 and Q = 5x10^{-5} m^3/s]: (a) H_{bed} = 10%; (b) H_{bed} = 30%; (c) H_{bed} = 50%; (d) H_{bed} = 70%; (e) H_{bed} = 90%; and (f) H_{bed} = 100%

Velocity Distributions for Diameter Ratio 0.75 (n = 0.6)

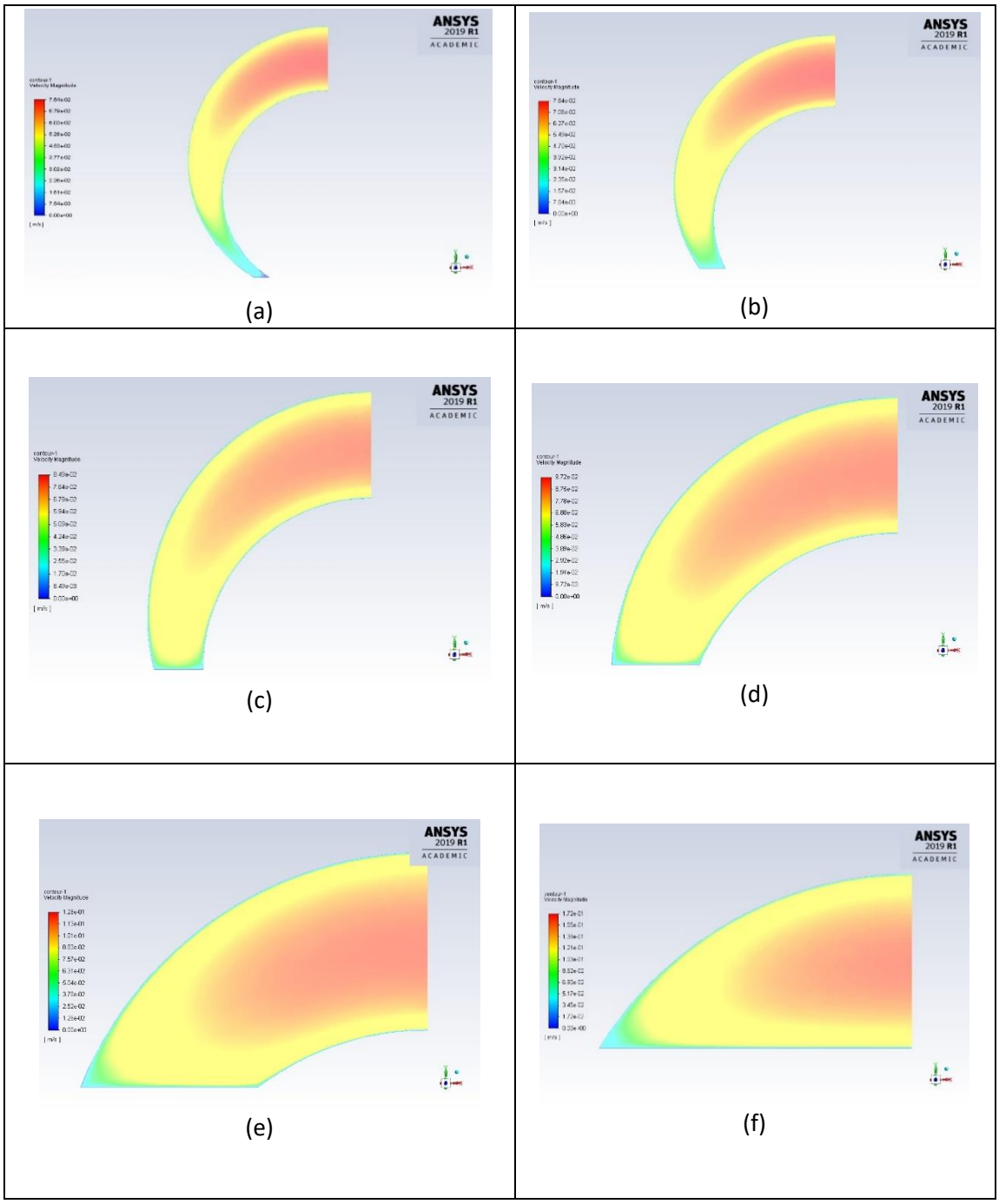

Figure A.15. Velocity distributions in partially blocked annuli [n = 0.6, κ = 0.75, e = 0.9 and Q = 5x10^{-5} m^3/s]: (a) H_{bed} = 10%; (b) H_{bed} = 30%; (c) H_{bed} = 50%; (d) H_{bed} = 70%; (e) H_{bed} = 90%; and (f) H_{bed} = 100%

Velocity Distributions for Diameter Ratio 0.75 (n = 0.4)

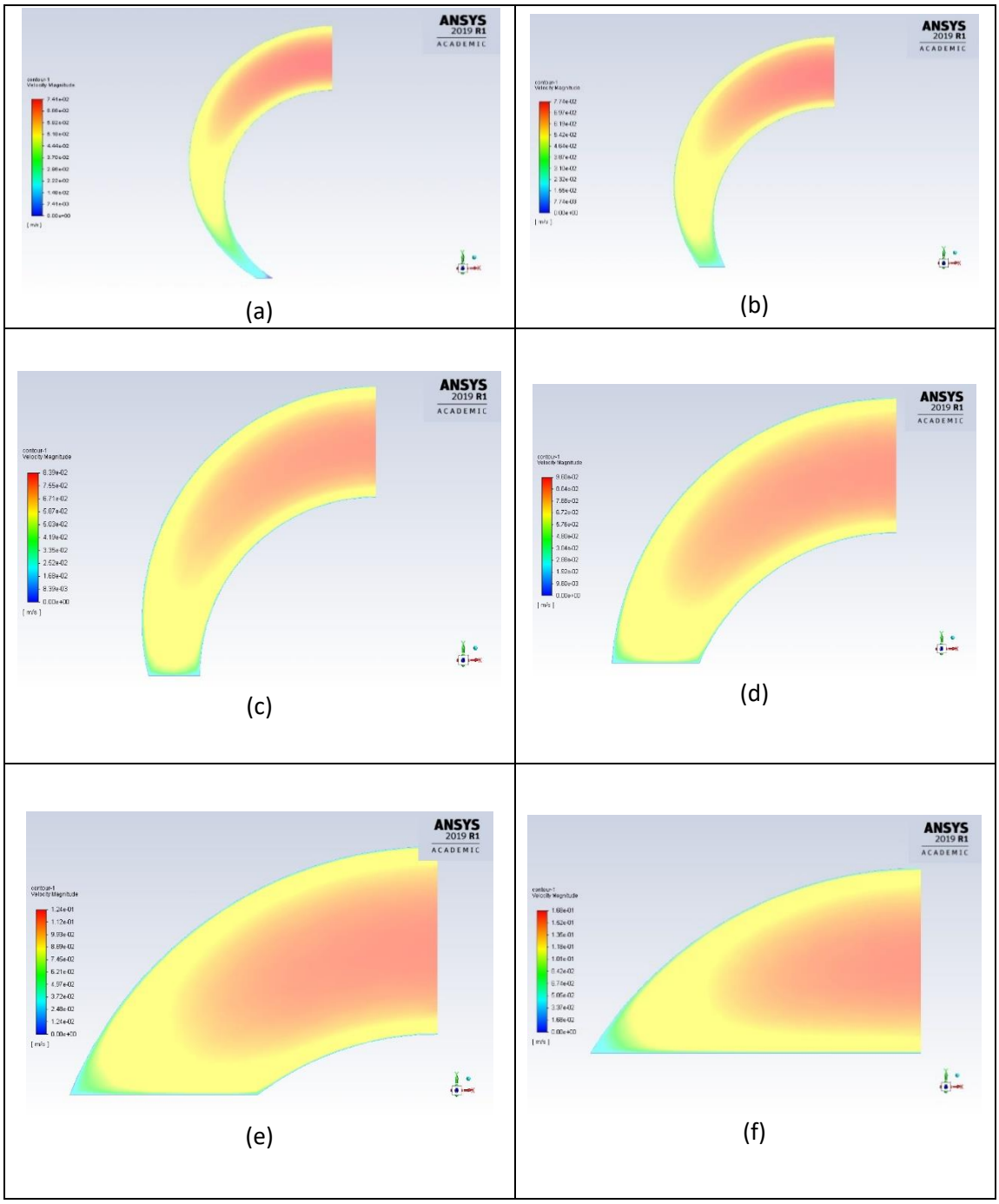

Figure A.16. Velocity distributions in partially blocked annuli [n = 0.4, κ = 0.75, e = 0.9 and Q = 5x10^{-5} m^3/s]: (a) H_{bed} = 10%; (b) H_{bed} = 30%; (c) H_{bed} = 50%; (d) H_{bed} = 70%; (e) H_{bed} = 90%; and (f) H_{bed} = 100%

Velocity Distributions for Diameter Ratio 0.75 (n = 0.2)

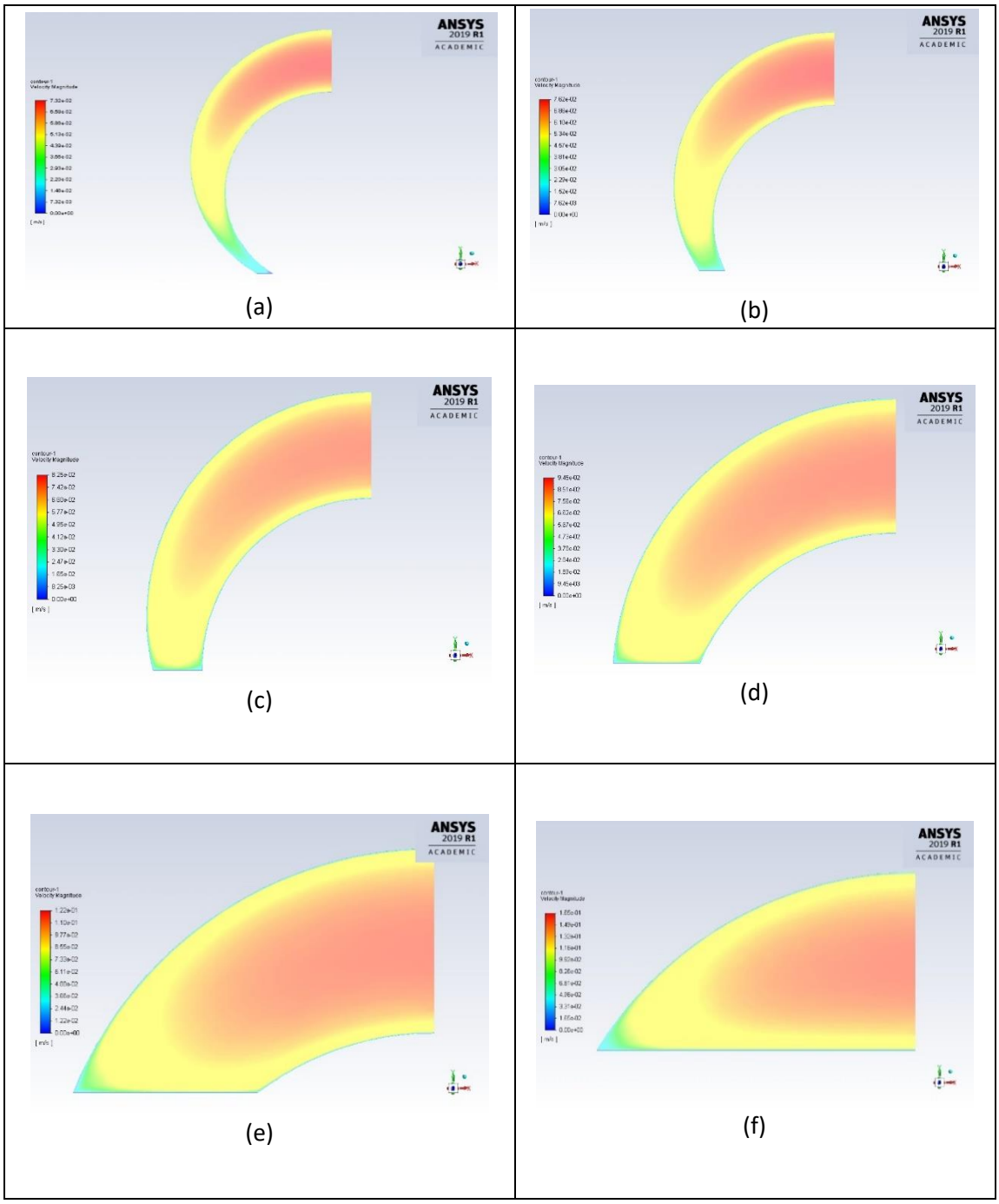

Figure A.17. Velocity distributions in partially blocked annuli [n = 0.2, κ = 0.75, e = 0.9 and Q = 5x10^{-5} m^3/s]: (a) H_{bed} = 10%; (b) H_{bed} = 30%; (c) H_{bed} = 50%; (d) H_{bed} = 70%; (e) H_{bed} = 90%; and (f) H_{bed} = 100%

Velocity Distributions for Diameter Ratio 0.75 and H_{bed} = 0%

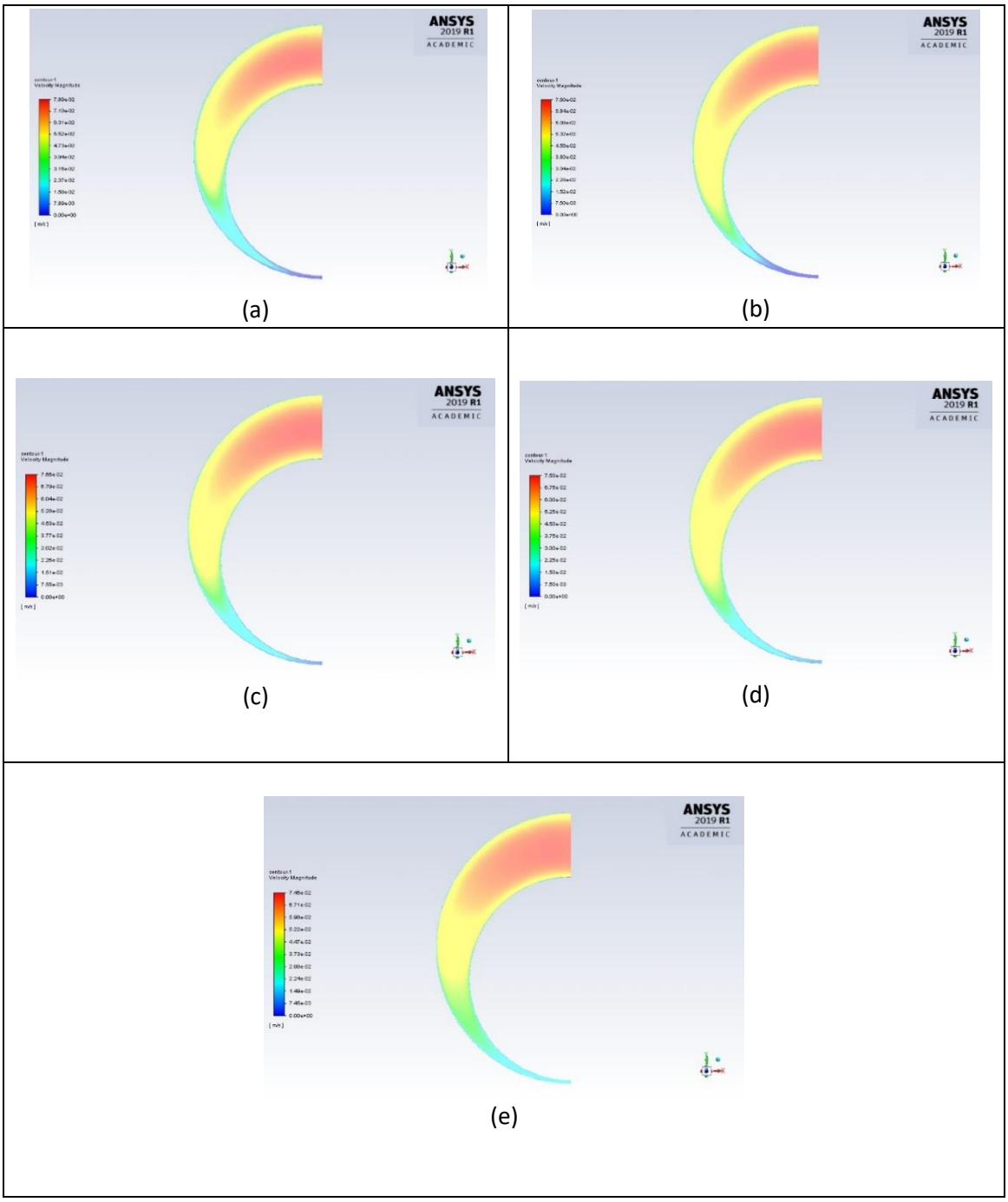

Figure A.18. Velocity distributions in unblocked annuli [κ = 0.75, e = 0.9 and Q = 5x10^{-5} m^3/s]: (a) n = 1; (b) n = 0.8; (c) n = 0.6; (d) n = 0.4; and (e) n = 0.2

Bed Shear Stress Distributions for Diameter Ratio 0.25

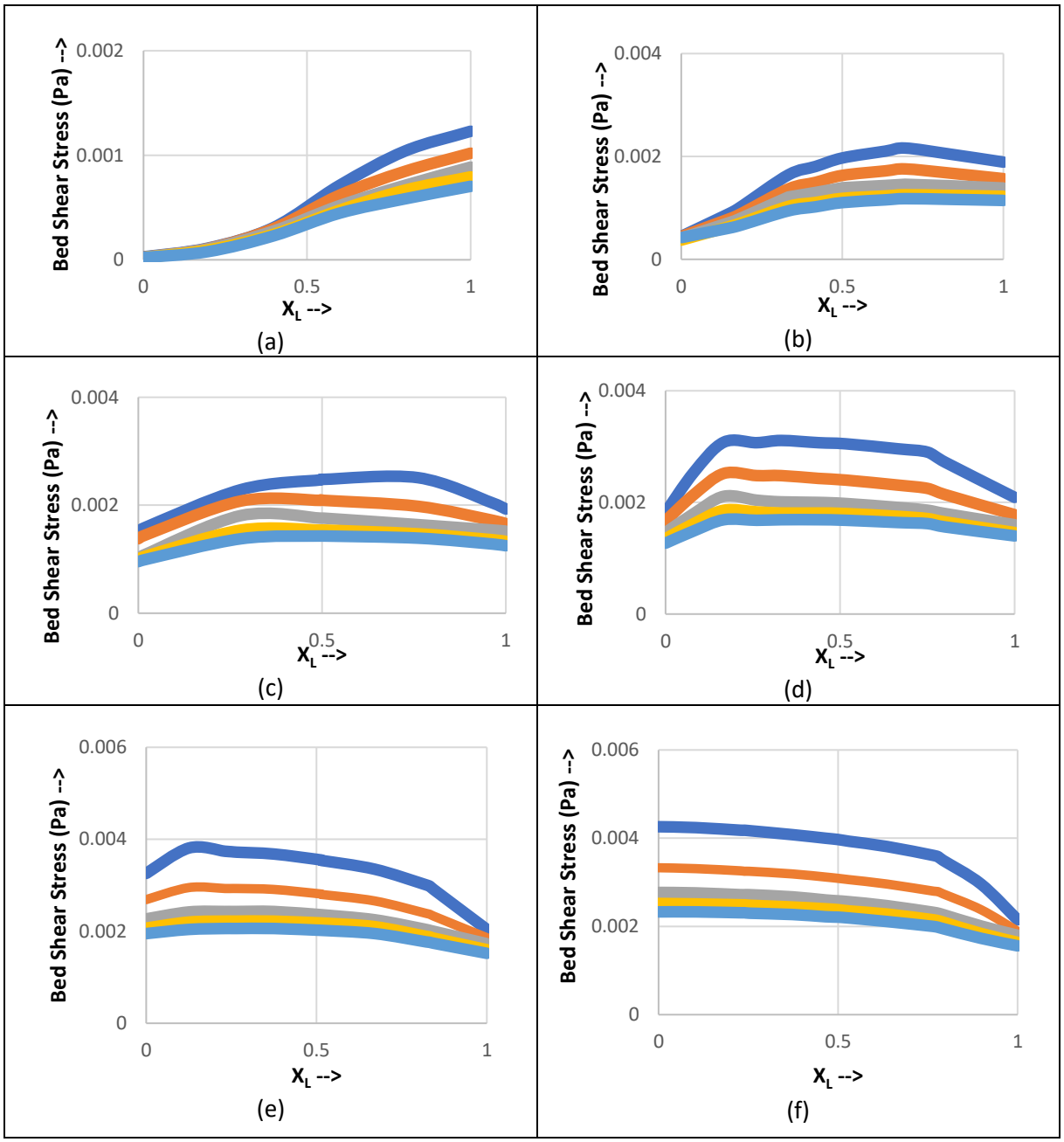

Figure A.19. Bed shear stress distributions for diameter ratio [κ = 0.25] (a) H_{bed} = 10%; (b) H_{bed} = 30%; (c) H_{bed} = 50%; (d) H_{bed} = 70%; (e) H_{bed} = 90%; and (f) H_{bed} = 100%

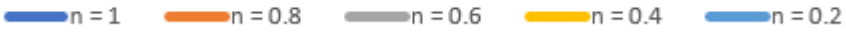

Bed Shear Stress Distributions for Diameter Ratio 0.50

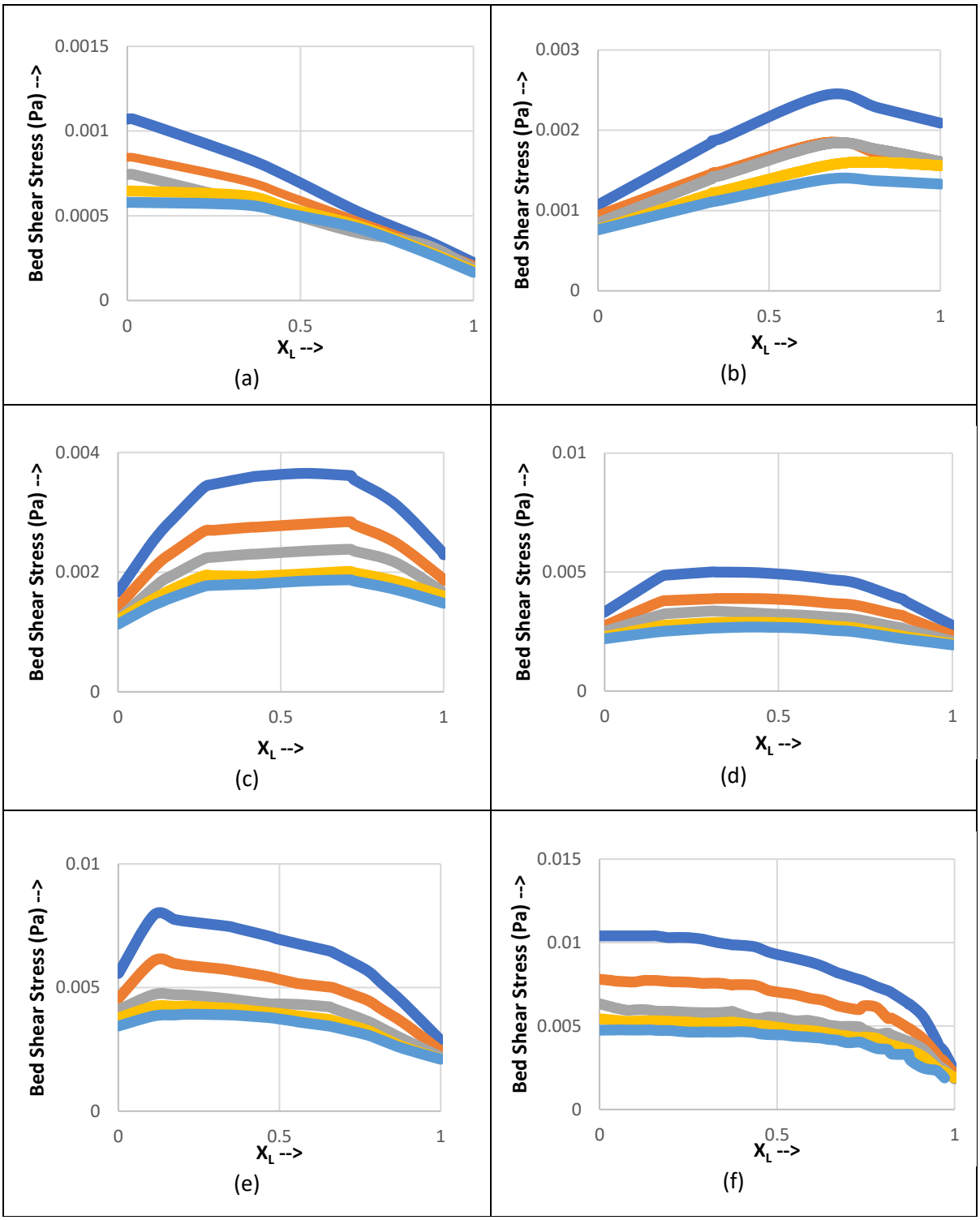

Figure A.20. Bed shear stress distributions for diameter ratio [κ = 0.50] (a) H_{bed} = 10%; (b) H_{bed} = 30%; (c) H_{bed} = 50%; (d) H_{bed} = 70%; (e) H_{bed} = 90%; and (f) H_{bed} = 100%

Bed Shear Stress Distributions for Diameter Ratio 0.75

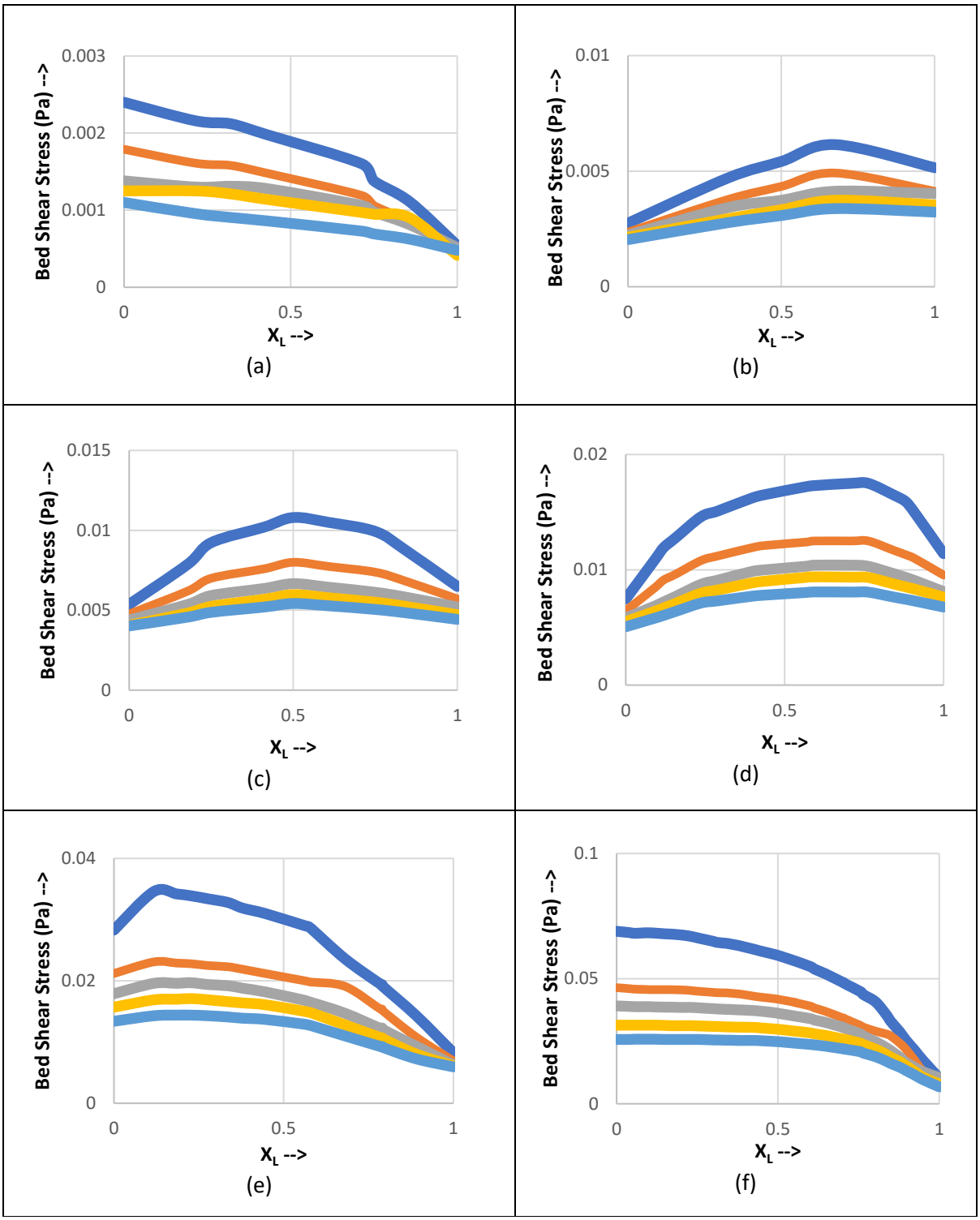

Figure A.21. Bed shear stress distributions for diameter ratio [κ = 0.75] (a) H_{bed} = 10%; (b) H_{bed} = 30%; (c) H_{bed} = 50%; (d) H_{bed} = 70%; (e) H_{bed} = 90%; and (f) H_{bed} = 100%

Velocity Distributions for Diameter Ratio 0.25

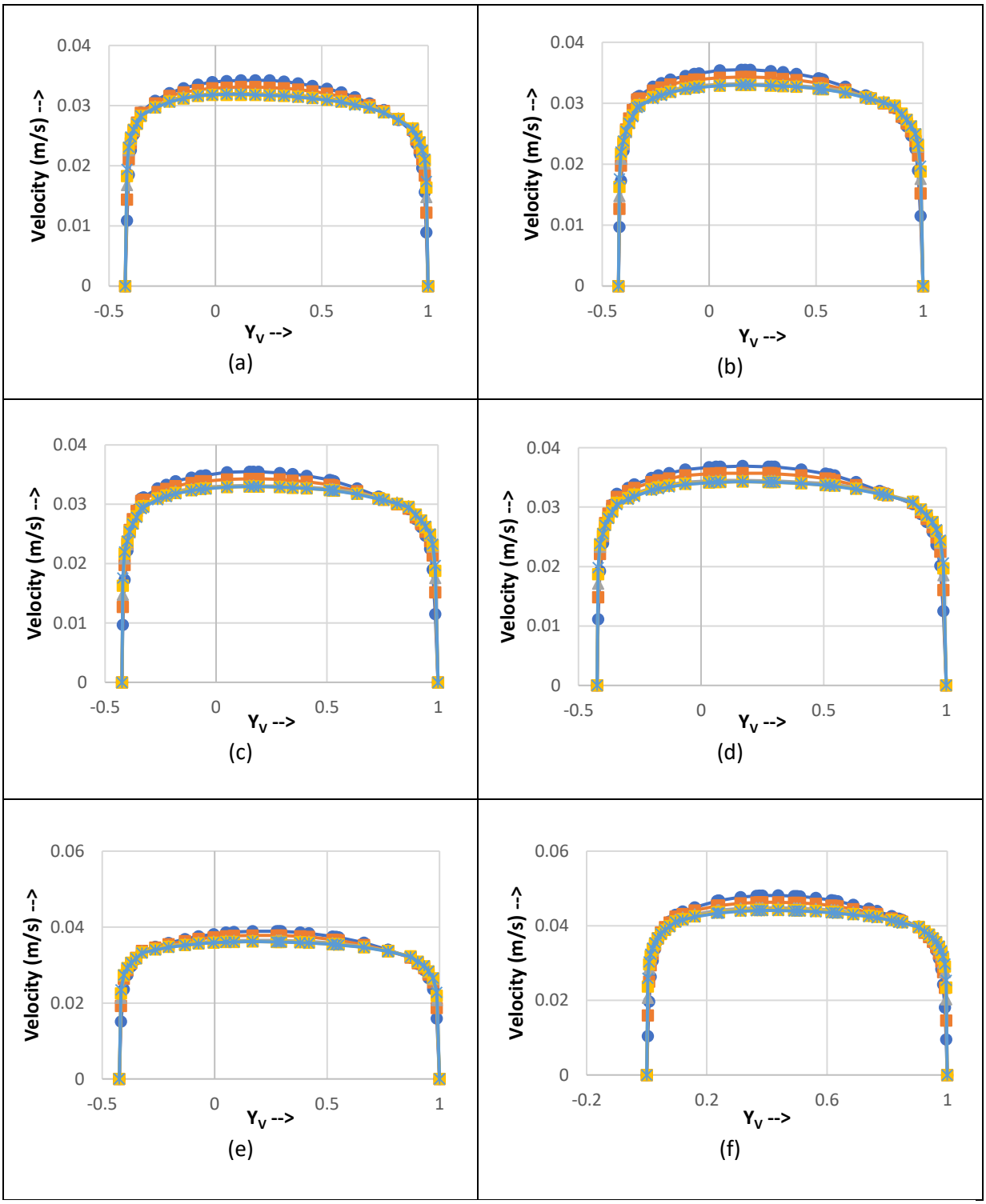

Figure A.22. Velocity profile [κ = 0.25 and Q = 5x10^{-5} m^3/s] (a) H_{bed} = 10%; (b) H_{bed} = 30%; (c) H_{bed} = 50%; (d) H_{bed} = 70%; (e) H_{bed} = 90%; and (f) H_{bed} = 100%

Velocity Distributions for Diameter Ratio 0.50

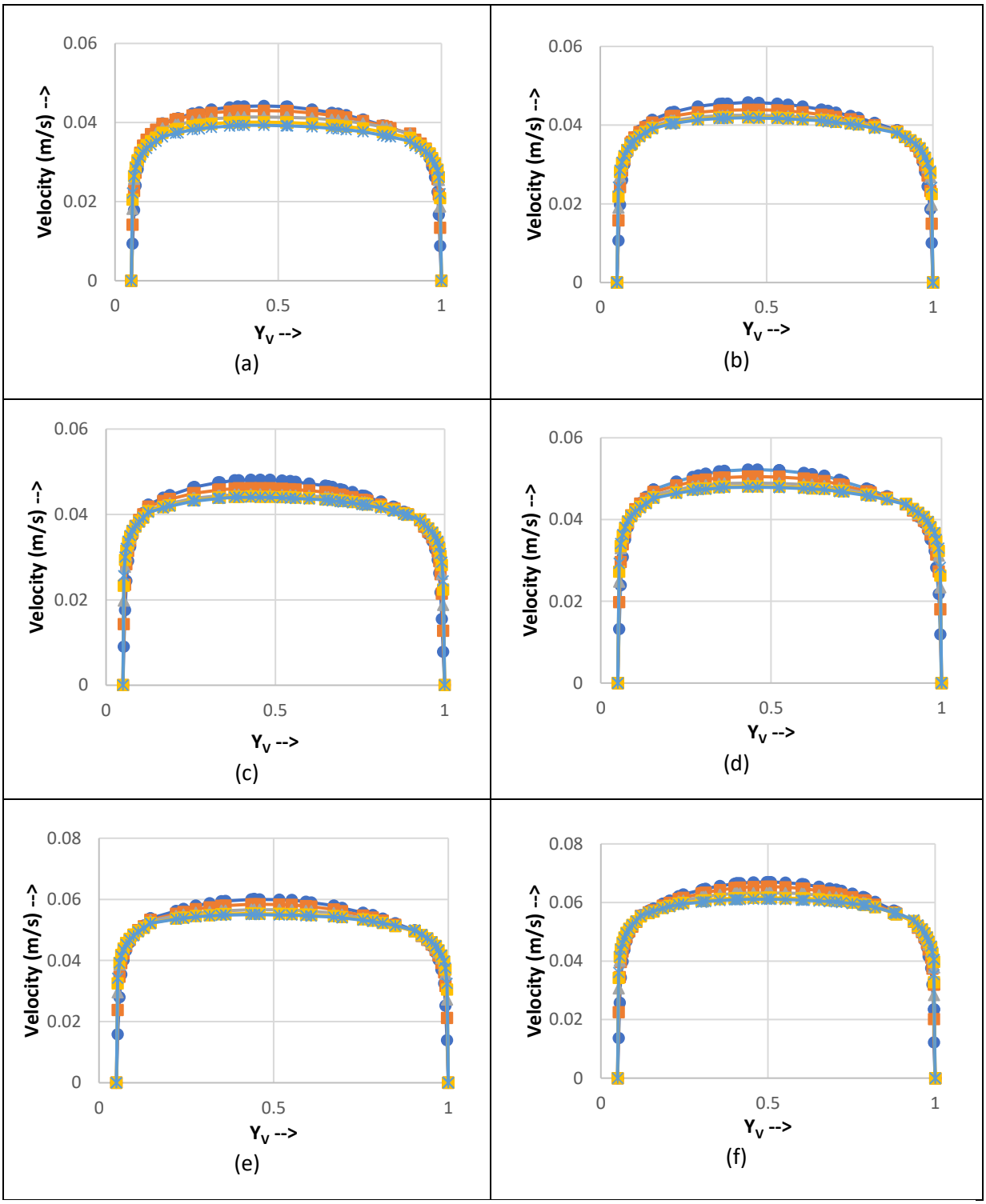

Figure A.23. Velocity profile [κ = 0.50 and Q = 5x10^{-5} m^3/s] (a) H_{bed} = 10%; (b) H_{bed} = 30%; (c) H_{bed} = 50%; (d) H_{bed} = 70%; (e) H_{bed} = 90%; and (f) H_{bed} = 100%

Velocity Distributions for Diameter Ratio 0.75

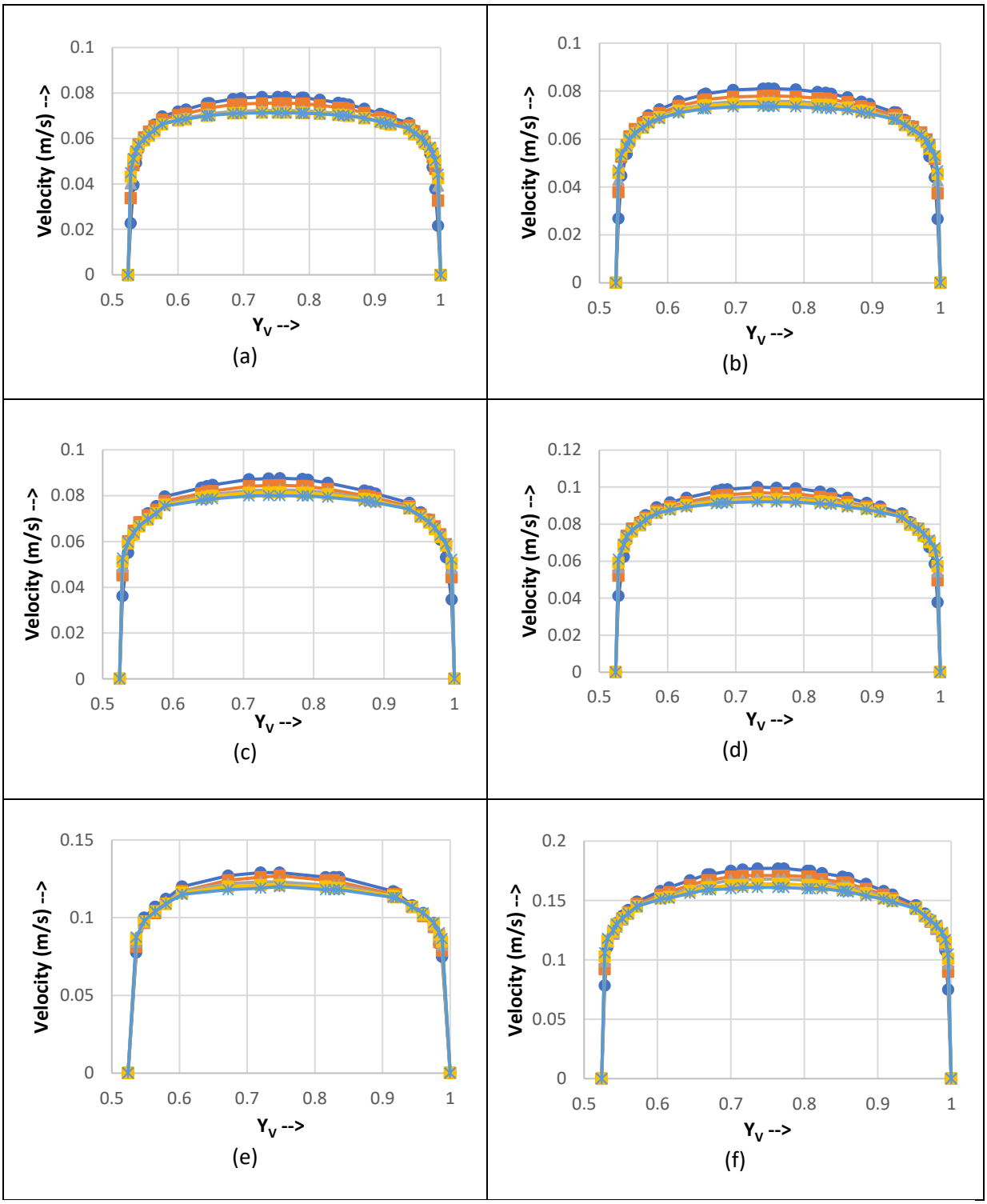

Figure A.24. Velocity profile [κ = 0.75 and Q = 5x10^{-5} m^3/s] (a) H_{bed} = 10%; (b) H_{bed} = 30%; (c) H_{bed} = 50%; (d) H_{bed} = 70%; (e) H_{bed} = 90%; and (f) H_{bed} = 100%

Velocity Distributions for H_{bed} = 0%

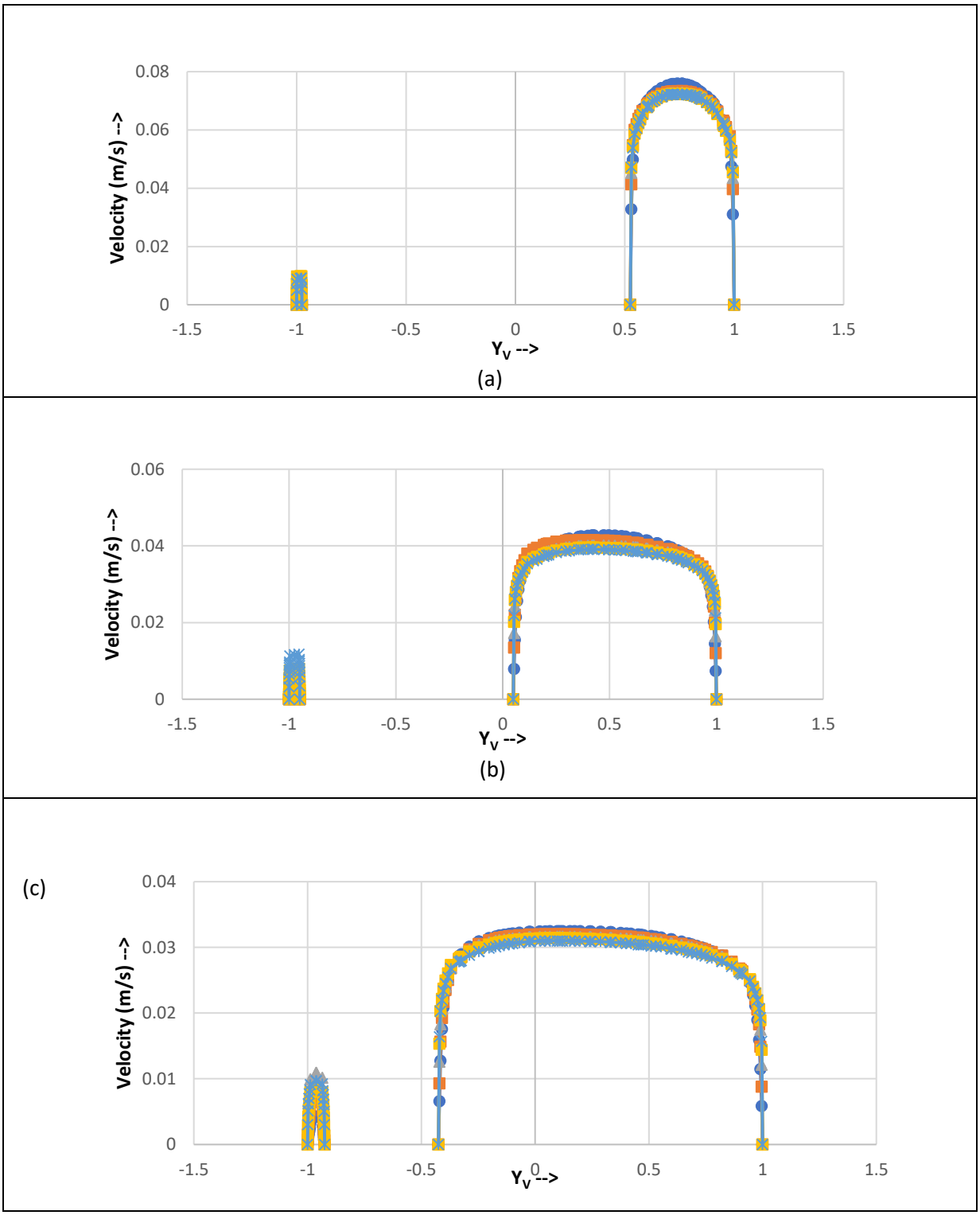

Figure A.25. Velocity profile [H_{bed} = 0% and Q = 5x10^{-5} m^3/s] (a) κ = 0.75; (b) κ = 0.50; (c) κ = 0.25

Bed Shear Stress Distribution for Diameter Ratio 0.50 with Varying K

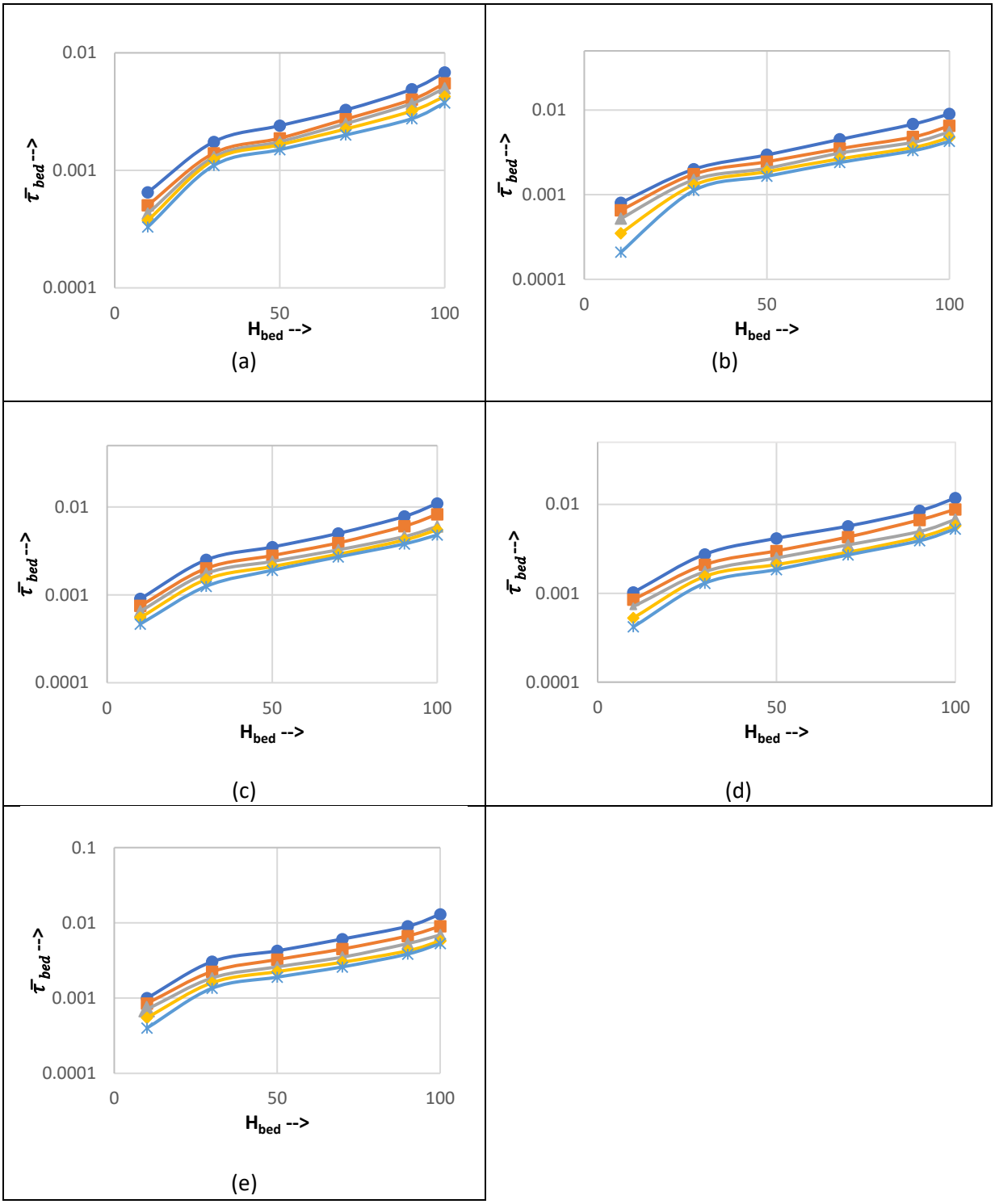

Figure A.26. Bed shear stress distribution [κ = 0.25 and Q = 5x10^{-5} m^3/s] (a) K = 1x10^{-5} kg/ms; (b) K = 2.5x10^{-5} kg/ms ; (c) K = 5x10^{-5} kg/ms ; (d) K = 7.5x10^{-5} kg/ms ; and (e) K = 1x10^{-4} kg/ms

Dimensionless Bed Shear Stress Distribution for Diameter Ratio 0.50 with Varying K

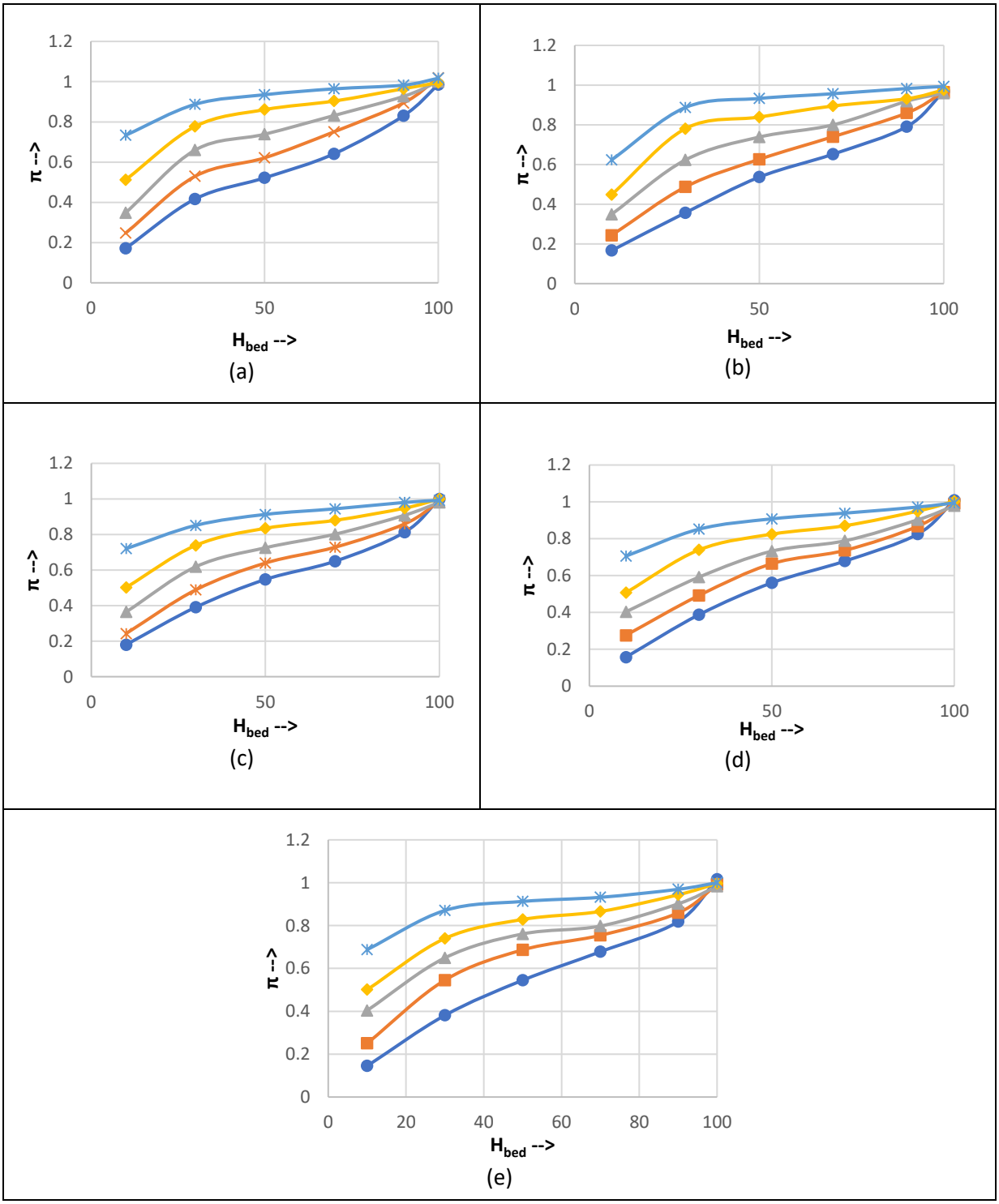

Figure A.27. Dimentional bed shear stress distribution [κ = 0.25 and Q = 5x10^{-5} m^3/s] (a) K = 1x10^{-5} kg/ms; (b) K = 2.5x10^{-5} kg/ms ; (c) K = 5x10^{-5} kg/ms ; (d) K = 7.5x10^{-5} kg/ms ; and (e) K = 1x10^{-4} kg/ms